TKK Dissertations 164
Espoo 2009

CAUSAL DIGRAPH REASONING FOR FAULT DIAGNOSIS IN PAPER MAKING APPLICATIONS

Doctoral Dissertation

Hui Cheng

Helsinki University of Technology
Faculty of Chemistry and Materials Sciences
Department of Biotechnology and Chemical Technology

TKK Dissertations 164
Espoo 2009

CAUSAL DIGRAPH REASONING FOR FAULT DIAGNOSIS IN PAPER MAKING APPLICATIONS

Doctoral Dissertation

Hui Cheng

Dissertation for the degree of Doctor of Science in Technology to be presented with due permission of the Faculty of Chemistry and Materials Sciences for public examination and debate in Auditorium KE2 (Komppa Auditorium) at Helsinki University of Technology (Espoo, Finland) on the 5th of June, 2009, at 12 noon.

Helsinki University of Technology
Faculty of Chemistry and Materials Sciences
Department of Biotechnology and Chemical Technology

Teknillinen korkeakoulu
Kemian ja materiaalitieteiden tiedekunta
Biotekniikan ja kemian tekniikan laitos

Distribution:
Helsinki University of Technology
Faculty of Chemistry and Materials Sciences
Department of Biotechnology and Chemical Technology
P.O. Box 6100 (Kemistintie 1)
FI - 02015 TKK
FINLAND
URL: http://chemtech.tkk.fi/en/
Tel. +358-9-4511
E-mail: sjtuchenghui@hotmail.com

ISBN 978-951-22-9878-5
ISBN 978-951-22-9879-2 (PDF)
ISSN 1795-2239
ISSN 1795-4584 (PDF)
URL: http://lib.tkk.fi/Diss/2009/isbn9789512298792/

TKK-DISS-2602

Picaset Oy
Helsinki 2009

ABSTRACT OF DOCTORAL DISSERTATION	HELSINKI UNIVERSITY OF TECHNLOGY P.O. BOX 1000, FI-02015 TKK http://www.tkk.fi

Author Hui Cheng

Name of the dissertation

Causal digraph reasoning for fault diagnosis in paper making applications

Manuscript submitted 02.02.2009	Manuscript revised
Date of the defence 05.06.2009	
☒ Monograph	☐ Article dissertation (summary + original articles)

Faculty	Faculty of Chemistry and Material Science
Department	Department of Biotechnology and Chemical Technology
Field of research	Causal digraph based fault diagnosis
Opponent(s)	Prof. Gentil Sylviane and Prof. Pentti Lautala
Supervisor	Prof. Sirkka-Liisa, Jämsä-Jounela
Instructor	Prof. Sirkka-Liisa, Jämsä-Jounela

Abstract

Fault detection and diagnosis systems are required by the process industries because of tightening global competition and the increasing complexity of the processes, which results in the difficulty for operators to perform the diagnosis tasks. Academic research in the field of fault diagnosis has expanded rapidly to meet this demand and successful applications with economic benefits have been reported extensively. As a fault diagnosis method, the causal directed graph method has proved to have considerable advantages in applications with complex processes. The causal digraph method has been subjected to three development phases: signed digraph, fuzzy digraph and dynamic digraph. Being versatile with cause-effect models, the causal digraph method is able to utilize the benefits of both qualitative and quantitative diagnosis methods. However, the latest development, the dynamic causal digraph method, still has certain drawbacks in the case of a process fault. In specific situations, the detection and diagnosis results are not always reliable or sufficient to satisfy the industrial requirements.

The aim of this thesis has been to enhance the traditional dynamic causal digraph method by developing a new fault detection approach and a new inference mechanism. The new detection approach produces better detection results and a more complete fault propagation path by taking into account the cancellation phenomenon of the different fault effects. The new inference mechanism is designed to identify possible faulty process components for the type of process fault. The proposed enhanced method has been tested on a generic paper machine simulator and the three-layered board machine simulator of Stora Enso Oyj. In the tests, a number of fault scenarios, sensor faults and process faults were using the proposed method. Finally, a comparison between the proposed method and the traditional method verified the improvements.

Keywords Fault diagnosis, Causal digraph, Paper making

ISBN (printed)	978-951-22-9878-5	ISSN (printed)	1795-2239
ISBN (pdf)	978-951-22-9879-2	ISSN (pdf)	1795-4584
Language	English	Number of pages	179

Publisher Helsinki University of Technology, Department of Biotechnology and Chemical Technology

Print distribution Helsinki University of Technology, Department of Biotechnology and Chemical Technology

☒ The dissertation can be read at http://lib.tkk.fi/Diss/ 2009/isbn9789512298792/

Preface

The research work presented in this thesis has been carried out in the Laboratory of Process Control and Automation, Helsinki University of Technology, between September 2004 and January 2009. I am very grateful to my supervisor, Sirkka-Liisa Jämsä-Jounela, for providing directions for this thesis. I would especially like to highlight her encouragement at the beginning of my PhD studies, and her continuous support. I also want to thank Professor Raimo Ylinen and Dr. Mats Nikus for their valuable advice and discussions.

I am very grateful to the pre-examiners, Professor Gentil Sylviane (Grenoble National Polytechnic Institute, France) and Professor Tommi Karhela (VTT, Finland), for their thoughtful review of the thesis and stimulating comments.

The thesis work was carried out in collaboration with VTT and Stora Enso Oy. I would especially like to thank Tommi Myller for providing his expertise about the board machine. The thesis work was mainly funded by the Finnish Graduate School in Chemical Engineering (GSCE), and this contribution is gratefully acknowledged.

I want to thank my colleagues in the Lab 'Kepo', who not only provided academic advice but also help in private life during my unforgettable four years in Finland. Especially, Mikko Vermasvuori, Nikolai Vatanski, Jerri Kämpe, Vesa-Matti Tikkala, Michela Mulas and Alexey are thanked for creating an inspiring atmosphere in the Lab.

Finally, I want to thank all my family. In spite of the distance, I have always felt them near me. I would especially like to emphasize my gratitude to my parents for being so supportive all these study years. I would also like to mention the love and support that I received everyday from my girlfriend Wei Song, which was food for my spirit during the last phase of my thesis.

Contents

List of Abbreviations

SDG	Signed Directed Graph
FCDG	Fuzzy Causal Digraph
QTF	Qualitative Transfer Function
DCDG	Dynamic Causal Digraph
EDCDG	Enhanced Dynamic Causal Digraph
MISO	Multiple Inputs Multiple Outputs
APROS	Advanced Process Simulation Environment
FD	Fault Diagnosis
UIO	Unknown Inputs Observer
MLP	Multi-Layer Perceptron
PCA	Principal Component Analysis
PLS	Partial Least Square
SOM	Self-Organizing Map
IR	Inverse Response
CR	Compensatory Response
CSTR	Continuous Stirred Tank Reactor
SCC	Strongly Connected Component
MSCC	Maximal Strongly Connected Component
FSS	Fault Separation Set
TMP	ThermoMechanical Pulp
CTMP	Chemi-ThermoMechanical pulp

List of Symbols

$\mu_Z(x)$	Membership value for the fuzzy set Z with crisp value x
$r_i(k)$	Simulation residual for node X_i
$r_i^p(k)$	Prediction residual for node X_i with the p-th input as measurement
P_Y^l	Set of indices of the parent nodes of the node Y
$r_i^{P_Y^l}(k)$	Prediction residual for node X_i with inputs in the set P_Y^l as measurement
P_Y	Set of indices of all the parent nodes of the node Y
<<	'negligible'
≅	'nearly identical to'
≈	'of the same order of magnitude'
$f_Y(\ )$	Discrete-time model for the node Y
Y	Node Y or the measurement of the node Y
$\hat{Y}$	Global simulation value of the node Y
$\overline{Y}$	Local simulation value of the node Y
GR_Y	Global residual for the node Y
LR_Y	Local residual for the node Y
ILR_Y^m	Individual local residual for the node Y with m-th input as measurement
$MLR_Y^{P_Y^l}$	Multiple local residual for the node Y with inputs in set P_Y^l as measurement

TLR_Y	Total local residuals for the node Y with all the inputs as measurement
U_n	Cumulative sum in the CUSUM method
m_n	The minimal value of the cumulative sum in the CUSUM method
β_0	The minimal detectable fault in the CUSUM method
μ_0	The mean value of the noisy signal in the CUSUM method
λ	The threshold for the cumulative sum in the CUSUM method
$CU(r)$	CUSUM calculation for the signal r
$IndexU_Y$	Set of detected parent nodes for the node Y
$contp_Y^i$	Fault effect contributions for the node Y from the i-th parent node
$contl_Y$	Local fault effect contribution for the node Y
PFE_Y	Set of the positive fault effect contributions for the node Y
NFE_Y	Set of the negative fault effect contributions for the node Y
$\mathbf{M}_Y$	Inter-arc knowledge matrix for the node Y or a sub process
$\mathbf{M}$	Inter-arc knowledge matrix for the whole digraph model
sv	Row vector representing a set of the suspected arcs
$ARC(\mathbf{M}, i)$	Function gives the arc of the i-th row in the matrix $\mathbf{M}$
$NUM(\mathbf{sv})$	Function gives the nonzero entries in a vector
$<A, B>$	Arc in the digraph model from the node A to the node B
M_b	Mass of the pulp in the blend chest of the short circulation in the layer 2 of the board machine [kg]
M_m	Mass of the pulp in the machine chest of the short circulation in the layer 2 of the board machine [kg]
Δt	Sampling time for the discrete-time model [s]

ρ_s	Density of the pulp [kg/m^3]
V_b	Volume of the pulp in the blend chest of the short circulation in the layer 2 of the board machine [m^3]
α	Percentage of the solid contents, which go through the wire in the short circulation of the layer 2 [%]
β	Percentage of the water, which goes through the wire in the short circulation of the layer 2 [%]
η	Retention rate of the former in the short circulation of the layer 2 [%]
δ	Retention rate during the web combination [%]

List of Figures

List of Tables

1 Introduction

1.1 Background

Owing to the increasing competition and complexity in the process industries, fault diagnosis systems that detect and locate the faults are needed to meet the requirements set on product quality, efficiency, environment and safety. On the one hand, the fierce competition in the global market means that the processes have either to run more efficiently or to produce the same quality of products with less stringent raw materials using more complex processes. On the other hand, the increasing complexity of the new processes means that the operator's tasks are moving from manual work to knowledge work. At the same time, fault diagnosis tasks can no longer be carried out by operators or plant engineers due to their complexity. According to the studies of Venkatasubramanian et al. (2003a), the improper management of abnormal situations results in the loss of 20 billion US dollars annually in the American petrochemical industry alone. The situation is probably even more serious in other industries or countries. For economic reasons, fault diagnosis systems are therefore needed to handle abnormal situations instead of human operators. By providing supportive information to the operators and/or recovering the process automatically, the fault diagnosis system keeps the complex processes running efficiently and safely. This will bring enormous economical benefits to the industries.

Academic research in the field of fault diagnosis has been very active since the 1970s. Our understanding of the nature of faults, as well as the goals and tasks of fault diagnosis, has changed considerably along with the development of fault diagnosis methods. The term 'fault' is generally defined as 'an unpermitted deviation of at least one characteristic property of the system from the acceptable, usual, standard condition.' (Isermann, 2006, p.20). Owing to the development of different types of method, the fault diagnosis problem has usually been defined in different ways. For

instance, it has been considered as a problem of pattern recognition from the pattern recognition perspective (Mourot et al., 1993). In the quantitative model based methods, fault diagnosis has been considered as 'Determination of the kind, size, location and time of detection of a fault. Follows fault detection. Includes fault isolation and identification.' (Isermann & Balle, 1997). After the 1980s, following the introduction of Artificial Intelligence (AI) methods such as fuzzy logic and artificial neural networks in the fault diagnosis research field, the definition of 'Abductive Diagnosis' was proposed. The task of fault diagnosis was presented as being 'to find the best hypothesis that best explains a set of observations' (Lapizco-Encinas & Reqqia, 2005).

Researchers' understanding of the structure of fault detection and diagnosis systems are also relatively variable, even though they are almost the same in nature. From the perspective of functionality, Isermann (1997) defines a system with three blocks: feature generation, symptom generation and fault diagnosis, which can be simply explained as residual generation, residual evaluation and fault diagnosis, respectively. From the point view of the information type, Venkatasubramanian et al. (2003a) defines a system with four blocks: measurement space, feature space, decision space and class space. However, these two structures are not totally different, because they both state that the essence of a fault detection and diagnosis system is to make a decision or to extract the fault information from the measurement data. Furthermore, the mapping functions between the four spaces in the second structure can be explained on the basis of the three functionality blocks in the first structure. For example, the function block of the feature generation in first structure can be placed between the measurement space and the feature space in the second structure. Similarly the symptom generation and fault diagnosis blocks are mapping functions between the feature space and decision space, decision space and class space respectively. Therefore, a more comprehensive understanding of the fault detection and diagnosis system is obtained.

Numerous fault diagnosis methods have been developed to carry out the mapping functions from the measurement space to the class space or to implement the

functionality blocks of feature generation, symptom generation and fault diagnosis. These methods differ from each other in terms of a priori knowledge and searching strategy. A comprehensive review and classification of these methods have been provided in Venkatasubramanian et al. (2003a). The three major categories are grouped (Figure 1) on the basis of the a priori knowledge type, because the search strategy is usually also dependent to a certain extent on the type of a priori knowledge.

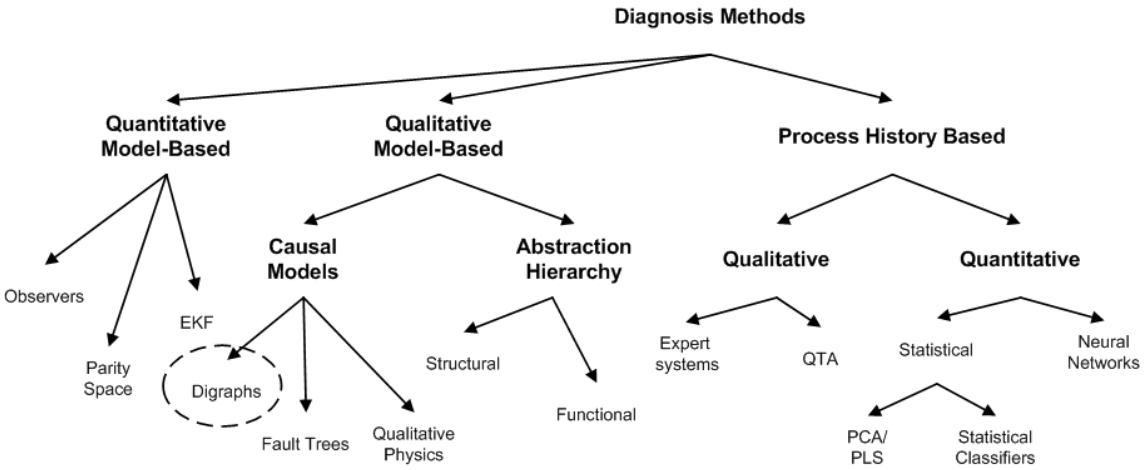

Figure 1. Classification of the fault diagnosis methods (Venkatasubramanian et al., 2003a).

The first group of fault diagnosis methods consists of quantitative model-based methods. Quantitative models are generally defined as input-output or state-space models. The fault diagnosis methods that include observers, parity space, Kalman filter, and parameter estimation, which utilize the quantitative models, belong to this category. The analytical redundancy described by the quantitative model is usually used for fault detection and diagnosis. For fault detection, the quantitative model is run parallel with the process in order to obtain the residuals, which are the discrepancy between the process and the model. The generated residuals are then evaluated for fault diagnosis by using their structural or direction information. The methods employed to design the structured residuals include different schemes for a bank of observers and fault filters. The dedicated observer scheme and generalized observer scheme are typical methods

for a bank of observers (Isermann, 2006, p.236), while unknown input observers (UIO) (Frank & Wönnenberg, 1989; Viswanadham & Scrichander, 1987 cited in Venkatasubramanian et al., 2003a) and the parity space method (Isermann, 2006, pp.210-220) are typical examples of fault filters.

The second group of methods is the qualitative model-based method. Unlike the quantitative models, qualitative models cannot describe the process using precise numeric models if a deep understanding of the process is not available (Lo et al., 2004). In the qualitative model, qualitative functions are constructed to describe the functions or behaviours of several units in the process. Qualitative functions for different units are then connected to form the qualitative model for the whole process according to the structural or functional hierarchy of the process. The fault diagnosis methods such as causal digraph methods, fault trees, qualitative physics, structural or functional abstraction hierarchy methods (Venkatasubramanian, et al., 2003b), which utilize the qualitative models for fault diagnosis, belong to this category. In this class of methods, fault detection is usually carried out directly by checking the measurements with the threshold values, because the qualitative model usually cannot be simulated parallel with the process. The fault-symptom causalities, i.e. structural or functional hierarchy knowledge of the process, are used for the fault diagnosis. Causal digraph methods, such as Signed digraph (SDG), fuzzy causal digraph (FCDG) and dynamic causal digraph methods (DCDG), perform the fault diagnosis using structural knowledge of the process (Iri et al., 1979; Shih & Lee, 1995a, b; Montmain & Gentil, 2000), while the multiple flow method performs the fault diagnosis using the functional hierarchy of the process (Larsson, 1996). Compared with the model-based quantitative methods, qualitative methods are able to handle more complex processes with a smaller modelling effort. However, the qualitative methods have their own drawback, which is the generation of spurious results.

The third group of methods is the process history based method, which utilizes the knowledge extracted from the history data in a qualitative or quantitative way. Rule-

based expert systems and qualitative trend analysis (QTA) are two of the most important qualitative historical data based methods (Venkatasubramanian, et al., 2003c). In the expert system, the system knowledge is represented in the form of IF-THEN rules extracted from the historical data of the process. Both inference mechanisms - forward chaining inference and backward chaining inference - can be used for fault diagnosis. The QTA method is able to extract a trend from the measurements, and this is used for fault detection and diagnosis. The quantitative model methods include artificial neural networks (ANN) and statistical methods. Depending on the type of problem, these methods are applied using a classification or a regression scheme. Moreover, the benefit of easy implantation is reflected by the large number of industrial applications reported (e.g. Komulainen et al., 2004; Jämsä-Jounela et al., 2003; Kämpjärvi et al., 2008 and Cheng et al, 2008b).

In this thesis, the causal digraph methods within the group of qualitative model-based methods are focused as illustrated in Figure 1. Accordingly, the term 'Fault diagnosis' is defined as fault detection and abductive diagnosis, because most of the causal digraph methods have been developed to search, by reasoning methods, for possible fault origins that can explain the observed faulty effects in a process. In particular, the dynamic causal digraph method is emphasized in this thesis, since it represents the latest development of the causal digraph methods and introduces the features of quantitative methods into the qualitative diagnosis methods.

1.2 Research problem and hypothesis

The major research problem of this thesis is to develop an enhanced dynamic causal digraph method (EDCDG) that integrates a new fault detection approach and a new diagnostic inference mechanism. The main aim of the enhanced method is to achieve better detection and fault diagnosis results. In processes where a fault is propagated through different pathways, the effects of a fault with different directions (positive or negative) may cancel each other out. In this case, the faulty variables appear

undetectable. Separating the different fault effects on the variables using the new detection approach enables these variables to be detected. For fault diagnosis, the traditional dynamic causal digraph method can only locate a fault in the variables. In the case of a process fault, however, it is also desirable to know which process components are responsible. A new inference mechanism is developed for finding the faulty process components.

The hypotheses of this thesis are:

1. The developed fault effects separation approach is able to enhance the traditional dynamic causal digraph method by giving better fault detection results for a process fault than the traditional method.
2. The dynamic causal digraph method enhanced by the developed inference mechanism is able to provide better diagnosis results for the process fault compared with the traditional method.

In order to prove the hypotheses, the following tasks had to be performed:

1. To develop a fault effects separation approach that detects the variables in the case of a process fault by taking into account cancellation of the fault effects.
2. To develop a diagnostic inference mechanism that allows identification of the faulty process components in the case of a process fault.
3. To develop an enhanced dynamic causal digraph method that combines the traditional dynamic causal digraph, the fault effects separation approach and the new diagnostic inference mechanism.
4. To develop a procedure for applying the enhanced dynamic causal digraph based fault diagnosis method.
5. To test the proposed method in the short circulation process of a generic paper machine simulator in the APROS environment.

6. To test the method in the stock preparation processes and the short circulation processes of a three-layered board machine APROS simulator of Stora Enso in Imatra

The first four tasks to develop the method and the procedure required for applying the method form the theoretical basis of this thesis. The last two tasks involve testing the method in the simulation environment.

1.3 Scope and content of the thesis work

The scope of the thesis work is the development of an enhanced dynamic causal digraph fault diagnosis method and its testing in a paper making process.

A literature review of the state of the art in causal digraph based fault diagnosis is presented in Chapter 2.

The enhanced dynamic causal digraph based fault diagnosis method and the corresponding application procedures are described in Chapter 3. In the EDCDG method, different fault effects are separated according to their directions, while a new diagnostic inference mechanism is used to identify the possible faulty process components. The application procedure describes the general steps used in applying the enhanced causal digraph method in papermaking processes.

In Chapter 4, the EDCDG method is tested in the short circulation process of a generic paper machine simulator in the APROS simulation environment. Three faults - a basis weight valve blockage, deculator consistency sensor drift and a retention drop in the former section, are studied. The process study, digraph modelling, fault scenario simulations and the fault diagnosis results are presented.

In Chapter 5, the EDCDG method is tested in stock preparation processes and short circulation processes of the Stora Enso board machine simulator in the APROS environment. Four different faults - consistency sensor bias, a retention drop in the former section, a headbox feed pump head drop and hydrocyclone plugging - are studied. The process study, digraph modelling, fault scenario simulations and the fault diagnosis results are presented. The hypotheses are asserted in Chapter 4 and 5.

In Chapter 6, the results from Chapters 4 and 5 are summarized and discussed. Finally, the conclusions and suggestions for future research work are presented in Chapter 7.

2 Causal digraph fault diagnosis methods: state of the art

Of the large number of fault diagnosis methods, causal digraph fault diagnosis methods are mainly studied in this thesis. As shown in the classification tree in Figure 1, digraph methods belong to the qualitative model-based method category and use a causal digraph model to perform the fault diagnosis. The causal graph is an excellent modelling method for representing those physical cause-effect relationships between different variables that are meaningful for the human operators in understanding the process or crucial for the fault diagnosis. In the causal directed graph models, the nodes denote the variables while the directed arcs between the nodes represent the causal relationships between these variables, through which faults could propagate. However, different models can be used to explain the cause-effect relationships on the arcs depending on the nature and abstraction level of the model. This has subsequently led to the development of a range of different methods for fault diagnosis.

Since Iri et al. (1979) introduced the SDG (the simplest causal-directed graph method) in the field of process fault diagnosis in 1979, there has been considerable progress in research on fault diagnosis methods with causal digraph models. In the past 20 years, dozens of modified causal digraph methods have been created and applied in the industry. Especially during the last decade, fuzzy logic (Shih & Lee, 1995a, b) and dynamic models, such as qualitative transfer functions (QTF) (Leyval, 1994) and difference equations (Montmain & Gentil, 2000), have been integrated into causal graph in order to increase the quantitative knowledge about the arcs and nodes for modelling a process. This, in turn, has provided space for developing new inference mechanisms for diagnosing the faults. The goals of reducing the uncertainty of the models and eliminating spurious and erroneous diagnosis results have been pursued along with the increase in qualitative knowledge. In fact, the history of the development of causal-directed graph fault diagnosis methods indicates a focus on increasing the quantitative

knowledge in qualitative models and on the development of new inference mechanisms that to improve the performance of fault diagnosis.

The basic SGD method proposed by Iri et al. (1979) models the process in a purely qualitative way, and this gave rise to the problem of spurious diagnosis results. Furthermore, for the sake of simplicity the SDG failed to analyze the faults whenever the inverse response (IR) and the compensatory response (CR) existed in a complex process (Oyeleye & Kramer, 1988). This limited the quality of the fault diagnosis result and impairs its practical usability. In order to decrease the number of spurious diagnosis results, a five-range pattern was applied to categorize the value of the variables by Shiozaki (1989) that replaced the original 3-suited threshold. Apparently the five-range pattern provided more quantitative information concerning the variables in the SDG, and this also leads to progress in the inference mechanism.

Applications of the SDG have been reported in different processes such as the nuclear power plant (Chung et al., 1994), the multi-stage separation process (Lai & Yu, 1995), the flash vaporizer process (Maurya et al., 2003a, b, 2004, 2006), and the furnace process in the petrochemical industry (Zhang et al, 2005). Furthermore, the variations of the SDG method tried to gain new features by combining it with other methods. An application of PCA-SDG has been reported in a fluidized catalytic cracking unit (Vedam & Venkatasubramanian, 1999), while the PLS-SDG and the dynamic PLS-SDG have been developed and applied in a pulp mill process (Lee et al, 2006) and a multi-stage flash desalination process (Ahn et al., 2008).

A major step in improving the fault diagnosis resolution of causal digraph models was the introduction of fuzzy logic. As for the five-range pattern, the fuzzy set theory was used to represent more quantitative knowledge about a small enough set of possible fault origins. Han et al. (1994) and Wang et al. (1995) utilized fuzzy membership functions to represent the variables, while the fault propagation manner was still kept as

consistency tables on arcs. Because the membership functions are related to the possibility distribution function, the results of the diagnosis have been evaluated on the basis of the degree of fuzzy set and the possibility of faults (Han et al., 1994). In the following year, Shih & Lee (1995a, b) extended their idea to signal propagation on the arcs, as well. In their paper, a fuzzy relation matrix was used to represent the causal-effect relationship between the nodes. Even though the fault diagnosis results were still obtained from the graph search inference mechanism, the results were sorted by the fuzzy membership function value, the credible fault membership and the frequency number. The number of spurious diagnosis results decreased considerably.

Several applications of the fuzzy causal digraph method have been reported. The application fields include the CSTR (continuous stirred-tank reactor) and the vaporizer (Han et al. 1994; Shih & Lee, 1995b), the waste water treatment process (Huang and Wang, 1999), the propane evaporator (Tarifa & Scenna, 1997) and the multi-stage flash desalination process (Tarifa & Scenna, 2004).

When using the methods mentioned above, however, the graph search inference mechanism still had to be used to find the paths of the fault propagation. This inference mechanism has high computational demands and can produce spurious diagnosis results because of uncertainty. Due to their poor ability to deal with dynamic situations, these methods are called steady-state analysis methods. Even with the integration of fuzzy logic, the representation of the variables and the relationship between them is still static. In order to incorporate more quantitative information about the process and to improve the fault diagnosis results, a qualitative transfer function (QTF) was introduced by Leyval et al. (1994). In the QTF-causal digraph model, the trajectories of the variables were used for the nodes, and the qualitative transfer function parameterized by a static gain, a delay and a settling time were used to represent the relationship between the variables. In the QTF the evolution of the variables was piecewise linear, and the event (the disturbance in a variable) was propagated through the arcs. However, the QTF-causal digraph has mainly been used for simulation purposes (Leyval et al., 1994). The

inverse inference mechanism was developed later by Montmain and Gentil (2000), with the difference and algebraic equations representing the cause-effect relationships. In this method, the behaviour of the process could be simulated dynamically and the graph search inference mechanism was no longer needed. With the inverse inference mechanism, the results of the global and local simulations were compared with the measured values in order to locate the fault. Application of the dynamic causal digraph method was reported in a nuclear fuel reprocessing process (Montmain & Gentil, 2000). The development history of the causal digraph based fault diagnosis methods is shown in Figure 2.

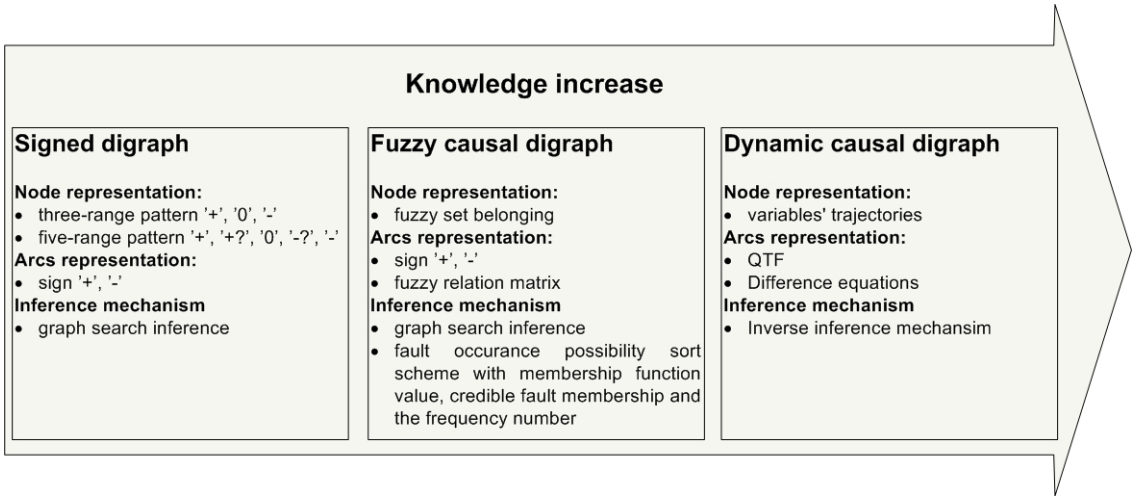

Figure 2. The development of causal digraph based fault diagnosis methods.

The SDG, FCDG and DCDG methods are reviewed in the rest of this chapter. A digraph model and a diagnosis mechanism are described for each method, respectively.

2.1 Fault diagnosis method based on the signed digraph

2.1.1 Signed digraph model

The original signed digraph model was introduced by Iri et al. (1979) for fault diagnosis in the chemical process industries. The definition of the SDG model was given by the following equation (Shih & Lee, 1995a).

$$MG = (V, E, \Lambda, \Delta) \tag{2.1}$$

V is the set of all nodes in the graph used to represent the variables of the process, which can be classified into two categories: measured variables and unmeasured variables, E is the set of the directed arcs of the graph, used to express the cause-effect relationships between the variable nodes. Λ is called a link influence function, giving a sign from the set {+, −} to the arc. Sign "+" is assigned to an arc if it is considered to have a positive gain influence, while sign "−" is assigned for the opposite case. The sign of the arcs can be acquired from the history data and process knowledge. Another way to determine the sign of the arcs is to derive it from the mathematical process model. For example we have a differential or an algebraic equation describing the process

$$\frac{dx_i}{dt} = f_i(x_1, x_2, \ldots, x_n) \quad or \quad x_j = f_j(x_1, x_2, \ldots, x_n) \tag{2.2}$$

If the partial derivative $\frac{\partial x_i}{\partial x_j}$ is positive, the sign of the arc between these two variable nodes is positive, and if it is negative the arc is negative. If the partial derivative is zero it means that there is no arc between them (Shih & Lee, 1995a).

Δ in Equation 2.1 represents the fault pattern of the nodes, which gives a sign from the set {+, 0, −} to the variable nodes according to the three-range thresholds shown in Figure 3. When the deviation of a measured value of the variable from its previous steady value is bigger than the thresholds *a1*, between *a1* and *a2*, or smaller than *a2*, the sign "+", "0" and "−" will be assigned to the corresponding nodes respectively.

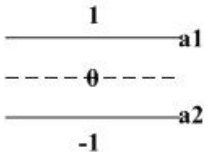

Figure 3. Three-range threshold.

Furthermore, the combination of the signs of all nodes is called the pattern of the system and represents its state. However, it rarely happens that all nodes in the SDG could be measured and assigned a sign. The sign of an unmeasured variable node could be decided arbitrarily. In this case the set of signs given on the measured variable nodes is called a partial pattern and the set of all the variables' signs is called the expanded pattern.

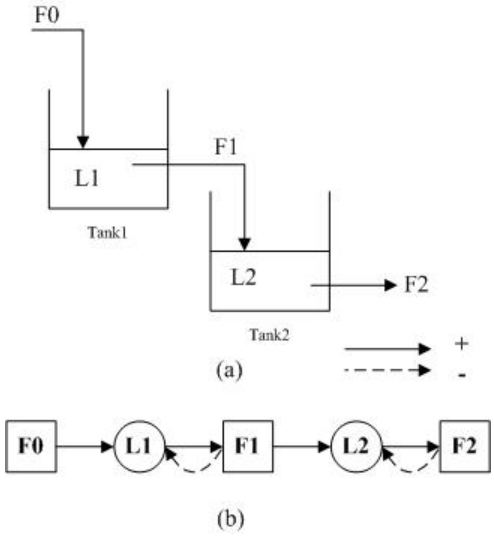

Figure 4. (a) Tank system (b) SDG model for the tank system (Shiozaki et al., 1989).

Figure 5. One pattern for the tank system (Shiozaki et al., 1989).

An example of the SDG is given in Figure 4 and a fault pattern of this SDG is given in Figure 5. In this example it is assumed that the flow rate variables are measurable and are denoted with a square in the graph, while the level of the tanks are not measured and are denoted with a circle in the SDG. The edges with sign "+" are represented with a solid line and edges with sign "–" are represented with a dashed line. It is assumed that the valve between the tank 1 and the tank 2 is faulty, which leads to the increase of the flow rate 1. The pattern of the two tank system is shown in Figure 5. Because the sign of the variables *L1* and *L2* are guessed, this is only one possible pattern out of the expanded pattern set.

2.1.2 Fault diagnosis with the signed digraph

After building the SDG model, it is assumed that the process is in a steady state, and thus the states of all the variable nodes in the digraph are "0". As an event (fault) occurs, its effect propagates through the whole graph. Thereby according to the measured variables and the guesses for the unmeasured variables, the patterns (expanded pattern) are obtained. For the purpose of fault diagnosis the graph can be simplified into a partial graph.

First, only the nodes whose signs are not "0" are considered as valid nodes for fault diagnosis. Then the consistency of the arcs is checked. If the sign of an arc, the sign of its predecessor node (*A*) and the sign of its descendent node (*B*) satisfy Equation 2.3, we call this arc to be consistent (Lai & Yu, 1995).

$$\operatorname{sgn}(A \to B) = \operatorname{sgn}(B) \cdot \operatorname{sgn}(A) \tag{2.3}$$

To make this consistency test easier, the consistency tables composed of all the possible combinations are made to distinguish the consistent arcs from the given expanded pattern. Figure 6 shows the truth tables used for the SDG with only two types of arcs: $A \xrightarrow{+} B$ and $A \xrightarrow{-} B$.

$A \xrightarrow{+} B$

	B	
A	+	-
+	T	F
-	F	T

$A \xrightarrow{-} B$

	B	
A	+	-
+	F	T
-	T	F

Figure 6. Consistency tables for the SDG fault diagnosis method (Lai & Yu, 1995).

Therefore, with all the valid nodes and consistent arcs, a partial graph called the CE-graph (Cause Effect) can be formed. Iri et al. (1979) stated, "If signs of all nodes are given, the origin of the failure exists in the maximal strongly connected component of the CE-graph." The CE-graph for the pattern in Figure 5 is given in Figure 7. First, the *F0* vertex is not a valid node because of its zero value. Then the arcs from *L1* to *F1* and from *F2* to *L2* are all removed because of inconsistency.

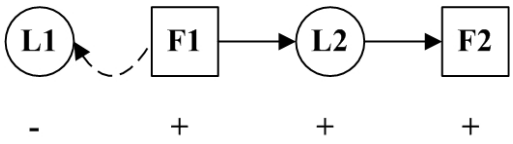

Figure 7. The CE-graph for the pattern in Figure 5.

Subsequently the graph search theory is applied to the CE-graph to search for the fault origin. Such subsets of the CE-graph that every node in it can be reached from every

other node are called the Strongly Connected Components (SCC). The roots of the SCC, which has no input arcs, are known as the Maximal Strongly Connected Components (MSCC). The SCCs and MSCCs can be found by the graph search algorithm (Tarjan, 1972, cited in Iri et al., 1979; Iri et al., 1979), while the nodes in the MSCCs are considered as the fault origins. An example of the graph decomposition is shown in Figure 8 for the CE-graph in Figure 7. The SCCs in the graph are enclosed by dashed circles.

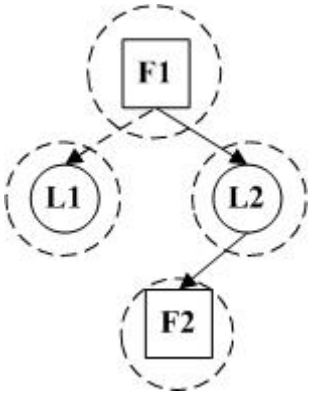

Figure 8. Decomposition of the CE graph into the SCCs.

In this special case the CE-graph in Figure 7 has no cycle in it, which means that every node can not be reached from every other node. Thus every node in the graph is a SCC, but only the *F1* node is an MSCC (the source of the whole CE-graph). It is obvious from Figure 8 that the *F1* node is the root of the whole CE-graph and also the root of the fault propagation path. Of course in most cases, there will be more than one MSCC, which implies more than one fault diagnosis solution for the basic SDG method. Moreover, this solution is only valid for the guessed values for *L1* and *L2*. If we make a new guess, a new fault solution will be obtained. In the real applications the SDG method produces lots of spurious fault solutions along with the correct one, and the SDG method cannot provide information to explain which fault solution is the most probable. The reason for these spurious solutions is the uncertainty resulted from the model. For the reason that the values of the unmeasured variables are not known and the

relations between the nodes are too simple, the false fault propagation path cannot be deleted from the alternatives.

So, in order to improve the fault diagnosis performance and to decrease the spurious fault diagnosis solutions, more quantitative knowledge was incorporated. The first way to do so was fuzzy logic, which is going to be studied in the following sections.

2.2 Fault diagnosis method based on the fuzzy causal digraph

In 1991 Yu and Lee (1991) used a fuzzy membership function to handle the uncertainty of the gain on the arc of the SDG, while the nodes were kept crisp. Another effort was made by Wang et al. (1995) to represent the nodes with a fuzzy membership function and the arcs with the crisp value of the 'causal strength'. Han et al. (1994) did the similar work except using the qualitative knowledge on the arcs. In the following year the further progress was made by using the fuzzy relations to estimate the unmeasured variables and to reduce the uncertainty of the model (Shih & Lee, 1995a, b). Thereby this fuzzy causal digraph method could decrease the spurious diagnosis results greatly. The FCDG has been applied to a real process and a comparison to the other diagnosis methods was studied. The conclusion drawn was that the FCDG can handle complex processes and get rid of erroneous diagnosis results in complex cases. Moreover, due to the relation between the fuzzy membership functions and the possibility functions, the diagnosis results could be ranked according to the fuzzy truth, making the isolation of fault candidates possible.

2.2.1 Fuzzy causal digraph model

The process transferring the real measured value into a fuzzy membership value is called fuzzification and the opposite process is called defuzzification. In the FCDG the signs "0", "+" and "–" assigned to the nodes in the original SDG are replaced by the fuzzy truth. Figure 9 shows the membership functions of the three fuzzy sets "N

(negative)", "Z (zero)", and "P (positive)", which are used by Shih and Lee (1995a) to represent the sign "−", "0", "+".. If one variable in the FCDG deviates from the steady value by −70, the fuzzy presentation for this deviation is [0.7, 0.3, 0] for the fuzzy sets "N", "Z" and "P" respectively, instead of just the sign "0" in the original SDG.

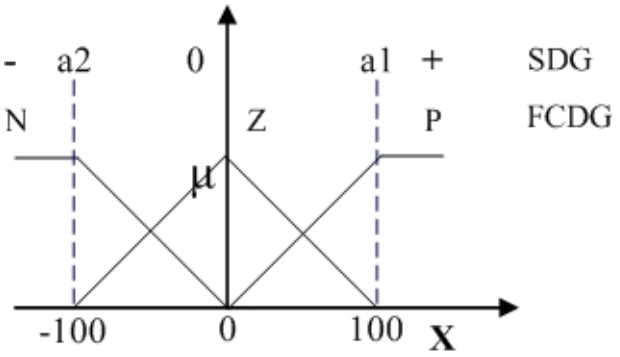

Figure 9. Membership function for the variable deviation (Shih & Lee, 1995a).

In the opposite case when the fuzzy representation of a node is available and the quantitative value of the variable deviation is demanded, defuzzification is applied. The discrete center-of-area (COA) method was used by Shih and Lee (1995a).

In the FCDG model, a fuzzy relation matrix is used to represent the cause-effect relationships between the variable nodes. According to the fuzzy logic theory, the relation matrix **R** is defined by the fuzzy composition, e.g. $\mathbf{B} = \mathbf{A} \circ \mathbf{R}$, where **B** and **A** are the family of fuzzy sets of the variable *B* (child node) and *A* (parent node) respectively, and ∘ denotes the composition operation (e.g., maximum-minimum). The relation matrix **R** is then calculated from the normal operation data of the variable *A* and *B* as

$$\mathbf{R} = \mathbf{A} \times \mathbf{B} = \int_{a \times b} \mu_a(A) \wedge \mu_b(B) \tag{2.4}$$

where a, b are the reference fuzzy sets of the variable A and B respectively, $\wedge$ is the conjunction operator (e.g., minimum), $\times$ is the Cartesian product. In the case that operation data from a different steady state is used, the fuzzy relation matrix $\mathbf{R}$ is calculated by $\mathbf{R} = \cup \mathbf{R}_k$, where $\mathbf{R}_k$ is the relation matrix for an operation state k, and $\cup$ is the disjunction operator (e.g., maximum) (Shih & Lee, 1995a).

The relation matrix $\mathbf{R}$ can be used to estimate the unmeasured variables in the fuzzy causal digraph model, while those variables are only guessed in the SDG method. For the digraph with m number of the input variables A_1 , A_2 ,…, A_m , the fuzzy representation of the output variable B is estimated as

$$\mathbf{B} = \mathbf{A}_1 \circ \mathbf{A}_2 \circ \cdots \circ \mathbf{A}_m \circ \mathbf{R} \tag{2.5}$$

After the defuzzification, the quantitative value of the variable B can be obtained.

2.2.2 Fault diagnosis with the fuzzy causal digraph

The diagnosis inference mechanism used by FCDG method is similar with the SDG method except that unmeasured variables are estimated by the fuzzy relations and that the possible fault origin candidates can be ranked by the fuzzy belonging (Shih & Lee, 1995b). By this way, the most possible fault origin can be identified.

Comparing to the original SDG method, the FCDG method has the following strong points (Shih & Lee, 1995b):

1. Increased diagnosis resolution compared to the original SDG.
2. Decreased amount of spurious fault interpretations.
3. Evaluation of the fault origin possibility.

4. Complex processes such as inverse responses and compensation responses, can be described by the FCDG model, thereby the FCDG has the ability to handle the complex process situations.
5. In cases with unmeasured variables and lack of the appropriate quantitative data of some variables, the FCDG can give the estimates of them using the fuzzy composition.

Compared to the other fault diagnosis methods, the FCDG model has following advantages (Shih & Lee, 1995b):

1. Short computation time due to the simple fuzzy calculations.
2. Can reduce spurious diagnosis solutions in complex process.
3. It can diagnose the fault origin in a process with single or multiple loops at early stages of the process faults.
4. New faults can be handled.
5. It can decide the key unmeasured variables and suggest where to install sensors to avoid degrading of the fault resolution.

However, the FCDG method is still a static and steady state method, which only utilizes the static relationship between variables and only concerns steady states of the process. In order to utilize the temporal and dynamic knowledge of the process, the dynamic causal digraph based fault diagnosis method was developed by introducing the dynamic model into the digraph.

2.3 Fault diagnosis method based on the dynamic causal digraph

The dynamic causal digraph fault diagnosis method further increases the amount of quantitative knowledge compared with the FCDG. In the dynamic causal digraph the nodes are no longer the deviations from a specific steady state. Instead, the trajectories of the process variables represent the nodes. The cause-effect relationships between variables are no longer static. Temporal knowledge and dynamic models have been introduced (Leyval et al., 1994; Montmain & Gentil, 2000). The inference mechanism for fault diagnosis is no longer the graph search algorithm. Instead, the inverse inference mechanism was developed to locate the fault.

2.3.1 Dynamic causal digraph model

In the dynamic causal digraph model, the nodes are represented by the trajectories of the process variables, while the cause-effect relationships between the variables are represented by the dynamic model or the temporal knowledge. The first type of dynamic digraph model used the qualitative transfer function to describe the cause-effect relationships (Leyval et al., 1994). The QTF is characterized by the gain, time delay and time lag of the parameters. In contrast to the traditional transfer function responses, the QTF response is piecewise linear. Several examples of the dynamic causal digraph model have been presented by Montmain and Gentil (2000), and by Fagrasan et al. (2004), which utilize difference equations, transfer functions etc. to describe the cause-effect relationships.

2.3.2 Fault diagnosis with the dynamic causal digraph

Due to the quantitative nodes and the dynamic model arcs, the dynamic causal digraph can be used to estimate the values of the variables in the digraph. The basic idea of fault

diagnosis with the DCDG is to compare the measurements of the nodes and the simulated values of the nodes.

For fault isolation purposes, the simulation with the DCDG is categorized into two groups: global simulation and local simulation. In the global simulation, the inputs of the dynamic model for one node are formed from the simulated values of its predecessor variables. However, the local simulation is performed by replacing the simulated values of the predecessor variables with the measured values. The diagnosis algorithm is called the inverse inference mechanism and is shown in Figure 10.

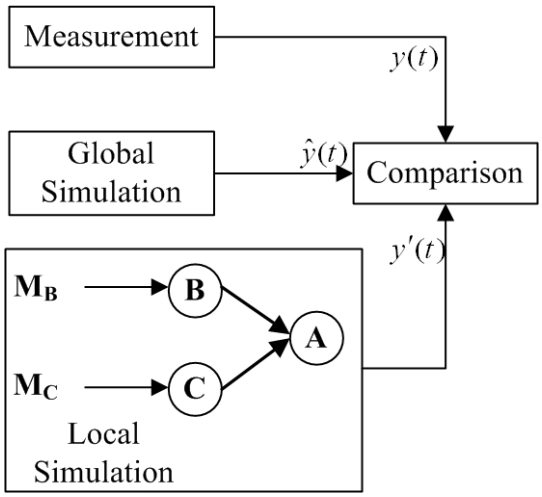

Figure 10. Basic idea of the inverse inference mechanism with the DCDG (Riera et al., 1999).

The fault diagnosis method based on the dynamic causal digraph developed by Montmain and Gentil (2000) performs the fault diagnosis in three steps.

1. Residual generation
2. Fault detection
3. Fault isolation

In the first step, the residual generation procedure is demonstrated by a system represented by the dynamic causal digraph with linear difference equations. Suppose one variable node X_i in the digraph has multiple input nodes X_j, as shown in Figure 11.

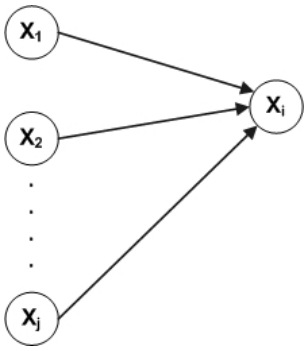

Figure 11. Example for residual generation with the DCDG.

The actual behaviour of the node X_i is described as

$$x_i(k) = (1 - A_i(q^{-1}))x_i(k) + \sum_{j \in P_i} q^{-d_{ji}} A_{ji}(q^{-1}) x_j(k) + E_i(q^{-1}) f_i(k) \tag{2.6}$$

where A_i and A_{ji} are polynomials in the shift operator q^{-1}, d_{ji} is the delay between the variable nodes X_i and X_j, P_i is the set of all the subscripts of j of the ancestor X_j, $f_i(k)$ is the local disturbance or fault at the node X_i, and $E_i(q^{-1})$ represents the fault effect transfer function at the node X_i (Montmain & Gentil, 2000). However, in the global simulation, the behaviour of the node X_i is computed as:

$$\hat{x}_i(k) = (1 - A_i(q^{-1}))\hat{x}_i(k) + \sum_{j \in P_i} q^{-d_{ji}} A_{ji}(q^{-1}) \hat{x}_j(k) \tag{2.7}$$

Thus the simulation residual of the node X_i is obtained by taking the difference between the measurement $x_i(k)$ and the global simulation value $\hat{x}_i(k)$ as:

$$\begin{aligned} r_i(k) &= x_i(k) - \hat{x}_i(k) = (1 - A_i(q^{-1}))r_i(k) + \sum_{j \in P_i} q^{-d_{ji}} A_{ji}(q^{-1}) r_j(k) + E_i(q^{-1}) f_i(k) \\ &= \sum_{j \in P_i} \frac{q^{-d_{ji}} A_{ji}(q^{-1}) r_j(k)}{A_i(q^{-1})} + \frac{E_i(q^{-1}) f_i(k)}{A_i(q^{-1})} \end{aligned} \tag{2.8}$$

Equation 2.8 (Montmain & Gentil, 2000) implies that the simulation residual is affected by both the simulation residuals of the predecessor nodes and the local faults. Thus the simulation residual is used for fault detection.

In order to isolate the fault, the prediction residuals are generated. In the local simulation, the behaviour of the node X_i can be computed by

$$\bar{x}_i^p(k) = (1 - A_i(q^{-1}))\bar{x}_i^p(k) + \sum_{\substack{j \in P_i \\ j \neq p}} q^{-d_{ji}} A_{ji}(q^{-1}) \hat{x}_j(k) + q^{-d_{pi}} A_{pi}(q^{-1}) x_p(k) \tag{2.9}$$

In Equation 2.9, the input from the predecessor X_p is replaced by its measurement $x_p(k)$. Thus the prediction residual is calculated as

$$r_i^p(k) = x_i(k) - \bar{x}_i^p(k) = (1 - A_i(q^{-1}))r_i^p(k) + \sum_{\substack{j \in P_i \\ j \neq p}} q^{-d_{ji}} A_{ji}(q^{-1}) r_j(k) + E_i(q^{-1}) f_i(k) \tag{2.10}$$

Comparing the simulation residual in Equation 2.8 and prediction residual in Equation 2.10 shows that the effect of the predecessor X_p is removed from the prediction residual. Therefore, the contribution from the node X_p (Montmain & Gentil, 2000) can be calculated by

$$\begin{aligned} r_i(k) - r_i^p(k) &= (1 - A_i(q^{-1}))\left(r_i(k) - r_i^p(k)\right) + q^{-d_{pi}} A_{pi}(q^{-1}) r_p(k) \\ &= \frac{q^{-d_{pi}} A_{pi}(q^{-1})}{A_i(q^{-1})} r_p(k) \end{aligned} \tag{2.11}$$

Equation 2.11 indicates that the difference between the two residuals is decoupled from the other predecessor nodes and the local fault. Similarly, if more than one measurement is used in the local simulation for the node X_i, the behaviour is computed as

$$\bar{x}_i^{P_i^l}(k) = (1 - A_i(q^{-1}))\bar{x}_i^{P_i^l}(k) + \sum_{\substack{j \in P_i \\ j \notin P_i^l}} q^{-d_{ji}} A_{ji}(q^{-1}) \hat{x}_j(k) + \sum_{m \in P_i^l} q^{-d_{mi}} A_{mi}(q^{-1}) x_m(k) \tag{2.12}$$

where P_i^l is the set of subscripts of the predecessor nodes, the measurements of which are used in the local simulation. The corresponding prediction residuals are therefore

$$\begin{aligned} r_i^{P_i^l}(k) &= x_i(k) - \bar{x}_i^{P_i^l}(k) \\ &= (1 - A_i(q^{-1}))r_i^{P_i^l}(k) + \sum_{\substack{j \in P_i \\ j \notin P_i^l}} q^{-d_{ji}} A_{ji}(q^{-1}) r_j(k) + E_i(q^{-1}) f_i(k) \end{aligned} \tag{2.13}$$

Thus the contribution from the nodes in the set P_i^l can be calculated as

$$r_i(k) - r_i^{P_i^l}(k) = \sum_{p \in P_i^l} \frac{q^{-d_{pi}} A_{pi}(q^{-1})}{A_i(q^{-1})} r_p(k) \tag{2.14}$$

In the second step, fault detection is performed with the simulation residuals of the nodes in the digraph. In the third step, each detected variable is tested with the rules to determine whether it is a primary fault (fault origin) or a secondary fault (fault propagated from predecessor nodes). The generic rules (Montmain & Gentil, 2000) are:

1. $\forall p \in P_i, r_i^p \cong r_i$: node X_i is the fault origin.
2. $r_i^p << r_i$, and $\forall j \in P_i, j \neq p, r_i^j \cong r_i$: fault propagates from the node X_p.
3. $\exists P_i^l \subset P_i$, and $r_i^{P_i^l} << r_i, \forall p \in P_i^l, r_i^p \approx r_i$: fault propagates from the nodes X_p, $p \in P_i^l$.

where $<<$, $\cong$ and $\approx$ represent 'negligible', 'nearly identical to' and 'of the same order of magnitude', respectively. After the introduction of the fuzzy representation of the order of magnitude, the test of the relationships of $r_i^p \cong r_i$, $r_i^p << r_i$ and $r_i^p \approx r_i$ are transferred to the calculation of the fuzzy belonging to $\left|r_i^p\right|/|r_i| \cong 1$, $\left|r_i^p\right|/|r_i| << 1$ and $\left|r_i^p\right|/|r_i| \approx 1$. The above rules are simplified into the calculation of the suspicion degree of the predecessor nodes of the detected variables (Montmain & Gentil, 2000) as:

$$\begin{aligned} \mu_{suspicion}(X_p) = & \left[\underset{\substack{j \in P_i \\ j \neq p}}{\wedge} \left\{ \mu_{\left|r_i^j\right|/|r_i| \cong 1}(r_i^j, r_i) \right\} \wedge \mu_{\left|r_i^p\right|/|r_i| << 1}(r_i^p, r_i) \right] \\ & \vee \left[\underset{\substack{j \in P_i^l \\ j \neq p}}{\wedge} \left\{ \mu_{\left|r_i^j\right|/|r_i| \approx 1}(r_i^j, r_i) \right\} \wedge \mu_{\left|r_i^p\right|/|r_i| \approx 1}(r_i^p, r_i) \wedge \mu_{\left|r_i^{P_i^l}\right|/|r_i| << 1}(r_i^{P_i^l}, r_i) \right] \end{aligned} \tag{2.15}$$

where '$\wedge$' and '$\vee$' are a conjunction and a disjunction operator, for which minimum and maximum operations are used, respectively.

With Equation 2.15, the detected variables and their predecessor nodes are evaluated by the fault suspicion degree. A simple threshold is set for the suspicion degree in order to decide whether a node is a fault origin. The predecessor node can be identified as a fault origin even if it is not detected with the simulation residuals due to the improper setup of the threshold. This provides the robustness of the fault diagnosis results.

The dynamic causal digraph based fault diagnosis method has the following advantages compared to the SDG and the FCDG:

1. The number of spurious fault diagnosis results are decreased significantly.
2. DCDG can cover not only one steady state of the process, but also a relatively broad and continuous state range of the process.
3. The inverse inference mechanism of the DCDG improves the efficiency of the inference compared with the graph search algorithm.

However, there are also some disadvantages to this method, which impair the applicability of the DCDG and give an incentive to further improve the fault performance. Firstly, fault detection based on the simulation residual r_i, given in Equation 2.8, is not valid in some special cases. Equation 2.8 clearly shows that the simulation residual r_i for the node i is the sum of the propagated fault effects r_j from the predecessor nodes X_j and the local fault $f_i(k)$. Therefore, in the case where different fault effects are acting in different directions, the simulation residual may disappear or be too small to be detected. For the same reason, cancelling out of the different fault effects can also occur in the calculation of the prediction residuals.

It is also implied by Equations 2.8 and 2.15 that fault isolation based on the suspicion degree calculation is no longer valid, even though the simulation residual is detectable.

The suspicion degree is calculated by comparing the simulation and the prediction residuals, with the implicit assumption that the different fault effects have the same sign and direction. When the assumption is not satisfied, the simulation residual can be smaller than the prediction residual which, in turn, results in an incorrect suspicion degree. Furthermore, because the ratio of the prediction residual to the simulation error is used to calculate the suspicion degree, which is sensitive to the noise, singularity problems may occur when the signals are noisy. Finally, a threshold for the suspicion degree has to be set in order to map the suspicion degree signal to the set {0, 1}, even though the residual has already been mapped into a real number between [0, 1] by the fuzzy sets at the beginning of the fault isolation.

The last problem considered is that the faults are usually located by the DCDG on the process variables (nodes), rather than on the level of process components (arcs). Two types of the fault are usually considered in the DCDG method. The first type is the sensor fault, which is defined as a measurement bias or drift. The second type is the process fault, which means the unwanted changes of the cause-effect relationships between the process variables. The DCDG method locates the fault on the variables for both of these two types of faults. In the case of a sensor fault, the diagnosis results are able to provide sufficient information to locate the fault in the component, because the variables correspond to the sensor in a straightforward manner. However, in the case of a process type of fault, the faulty nodes cannot tell the responsible components due to the MISO (multiple input and single output) structure of the digraph. In industrial applications, on the other hand, it is usually necessary to know the corresponding faulty process component. One important task is therefore to locate the responsible arc.

3 An enhanced dynamic causal digraph method for fault diagnosis and its application procedure

An enhanced dynamic causal digraph method is proposed in this chapter. Specifically, the fault separation approach and the inference mechanism between the arcs have been developed in order to overcome the drawbacks of the dynamic causal digraph method as discussed in Section 2.3.2. In order to make the application of the proposed method easier, it is also described in general terms at the end of this chapter.

3.1 Fault diagnosis method based on the enhanced dynamic causal digraph

The enhanced dynamic causal digraph method performs the fault detection and isolation in five steps:

1. Generate the global residuals (*GR*).
2. Detect a possible abnormality in the *GR* signals using the CUSUM method in order to form the detection set.
3. For the variables in the detection set, generate the local residuals (*LR*), apply the CUSUM method to the *LRs*, locate the primary fault and identify its nature by means of the fault isolation and nature rules. The preliminary fault propagation path is formed in this step.
4. In the case of a process fault, the fault effects separation approach is applied. If more variables are detected, the preliminary fault propagation path is modified.
5. In the case of a process fault, an additional inference step between the arcs is performed in order to locate the fault on the responsible arc(s).

These steps are described in detail as follows.

3.1.1 Residual generation with the dynamic causal model

The dynamic causal digraph produces two kinds of residuals to be used in fault detection and isolation: global and local residuals (referred as a simulation residual and a prediction residual in Chapter 2). The global residual is produced for the purpose of fault detection by a difference between the measurement and the global propagation value:

$$GR_Y = Y - \hat{Y} \tag{3.1}$$

where Y is the measurement and $\hat{Y}$ is the global propagation value obtained by

$$\hat{Y}(k) = f_Y(\hat{U}(k-1), \hat{U}(k-2), \ldots) \tag{3.2}$$

where $\hat{U}(k-\tau) = \{\hat{u}_1(k-\tau), \ldots, \hat{u}_n(k-\tau)\}$ are the lagged global propagation values from the predecessors in the digraph model, τ is the time lag 1, 2, … depending on the system order, $f_Y()$ is the discrete-time model with n input variables and the output variable Y.

The local residuals are subcategorized into three types: individual local residuals (*ILR*), multiple local residuals (*MLR*) and total local residuals (*TLR*).

The individual local residual is produced by taking the difference between the measurement and the local propagation value with only one measured input, while all the others are propagation values from the parent nodes.

$$\begin{aligned} ILR_Y^m &= Y - \overline{Y} \\ \overline{Y}(k) &= f_Y(\overline{U}(m, k-1), \overline{U}(m, k-2), \ldots) \end{aligned} \tag{3.3}$$

where $\overline{U}(m, k-\tau) = \left\{ \overline{u}_i(k-\tau) \middle| \overline{u}_i(k-\tau) = \begin{cases} \hat{u}_i(k-\tau), i \neq m \\ u_i(k-\tau), i = m \end{cases}, 1 \leq i \leq n \right\}$, $\hat{u}_i(k-\tau)$ is the lagged global propagated value from the predecessors, and $u_i(k-\tau)$ is the measurement for the *i*-th parent node.

Similarly, the $MLR_Y^{P_Y^l}$ is produced as

$$\begin{aligned} MLR_Y^{P_Y^l} &= Y - \overline{Y} \\ \overline{Y}(k) &= f_Y(\overline{U}(P_Y^l, k-1), \overline{U}(P_Y^l, k-2), \ldots) \end{aligned} \tag{3.4}$$

where $\overline{U}(P_Y^l, k-\tau) = \left\{ \overline{u}_i(k-\tau) \middle| \overline{u}_i(k-\tau) = \begin{cases} \hat{u}_i(k-\tau), i \notin P_Y^l \\ u_i(k-\tau), i \in P_Y^l \end{cases}, 1 \leq i \leq n \right\}$, P_Y^l is the set of indices of the predecessors which use the measurement as an input. The TLR_Y is produced with $P_Y^l = P_Y$, where P_Y is the set of indices of all the predecessors of *Y*.

3.1.2 Fault detection with the CUSUM method

The CUSUM method is used to evaluate the generated residual signals with respect to its insensitivity to the noise and outliers in the measurements. Moreover, the CUSUM method is able to detect both positive and negative changes in the mean of the residual signal. The direction of the change provides useful information for fault diagnosis.

The residual signals produced are mapped to the set {0, 1, −1} by the CUSUM method. In the faultless case, the residuals are assumed to be zero mean random signals, and in the case of a fault the mean value of the residual signal is changing in either a positive or a negative direction.

The CUSUM algorithm (Hinckley, 1971) for a positive mean change is given by the following equations:

$$\begin{aligned} U_0 &= 0 \\ U_n &= \sum_{k=1}^{n} \left(r(k) - \mu_0 - \beta_0 / 2 \right) \\ m_n &= \min_{0 \le k \le n} U_k \end{aligned} \tag{3.5}$$

where β_0 is a user-specified minimum detectable change, $r(k)$ is the residual signals, and μ_0 is the mean value of the nominal signal. Whenever $U_n - m_n > \lambda$, a change is detected. λ is the design parameter, usually tuned according to the requirements for the false alarm and missed alarm rates. It provides robustness to the fault detection but it also delays the detection. A similar algorithm for the detection of the negative mean changes can easily be obtained by modifying Equations 3.5. In the rest of the thesis, the result of the CUSUM calculation will be denoted as a function: *CU* (*r*).

3.1.3 Fault isolation using a set of rules

Fault isolation is performed recursively for the nodes in the detection set by using a set of rules. These isolation rules, developed by Montmain and Gentil (2000), see Section 2.3.2, are converted into a table for the convenience of implementation, as shown in Table 1.

From Table 1, the first row can be interpreted that no fault is detected. In the second row, node Y is detected first, because GR_Y is detected. The ILR_Y^m and $MLR_Y^{P_1}$ are not detected, which implies that the fault effect from other nodes than m-th node are negligible. Furthermore, the ILR_Y^i and $MLR_Y^{P_2}$ are detected, which implies that the fault effects from the m-th node is significant. Similarly, for the third row, the rule for deciding the fault propagation path through multiple parent nodes is presented. In the last row, where all the residual signals are detected, the local fault is identified.

Table 1. Fault isolation rules of the dynamic causal digraph.

$CU(GR_Y)$	$CU(TLR_Y)$	$CU(ILR_Y^m)$	$CU(ILR_Y^i)$	$CU(MLR_Y^{P_1})$	$CU(MLR_Y^{P_2})$	Decision
0	0	0	0	0	0	No fault
1/−1	0	0[1)]	1/−1[1)]	0[1)]	1/−1[1)]	Fault propagates from the parent node m
1/−1	0	1/−1[2)]	1/−1[2)]	1/−1[2)]	0[2)]	Fault propagates from the nodes with an index in P_2
1/−1	1/−1	1/−1	1/−1	1/−1	1/−1	Local fault on the variable Y

[1)] $\forall i \neq m, i \in P_Y$, $m \in P_1$, $m \notin P_2$, $P_1, P_2 \subseteq P_Y$, P_Y is the set of indices of parents nodes of the node Y.

[2)] $\forall i, m, i \in P_Y, m \in P_Y$, $\forall P_1, P_2 \subseteq P_Y$

After the fault isolation, the nature of the fault is identified by testing how the fault propagates from the fault origin to their children nodes. If the global residuals of the children nodes are detected and the local residuals of the children nodes are normal, it can be inferred that in the process the fault propagates to the other parts, while the measurement of the fault origin variable has no fault. Thus the fault is identified as a process fault. On the contrast, if the global residuals of the children nodes are normal and the total local residuals are detected, it can be inferred that in the process the fault does not propagate further and the measurement of the fault origin variable is faulty.

Therefore, it is defined as a local measurement fault. The rules for identifying the nature of the fault are given in Table 2.

Table 2. Fault nature rules of the dynamic causal digraph.

$CU(GR_X)$[1)]	$CU(TLR_X)$	Fault nature
1/−1	1/−1	Local fault for that child node
1/−1	0	Process fault for the faulty node
0	1/−1	Measurement fault for the faulty node

[1)] X is the index of any child nodes of the node Y.

3.1.4 Separation of the fault effects

In order to manage the specific cases where *GR* becomes too small to detect due to the cancellation of different fault effects, the fault effects with different directions are taken into account and separated. It can be seen from Equation 2.8 that the global residuals are generated by the sum of the different fault effects from both the local fault and the parent nodes. If the fault effects have different directions, i.e. positive or negative, there is the possibility that cancellation of the fault effects will make the global residual disappear. Furthermore, the different fault effects can be calculated using Equation 2.11 with the assumption that there is no measurement fault. Thus, the proposed approach to perform the separation of the fault effects in the case of a process fault is as follows:

1. Form the fault separation set consisting of the variables, for which different fault effects in the *GRs* need to be separated.
2. For each variable in the set formed in Step 1, calculate the fault effect contributions from its detected parent nodes and its local fault effect
3. Rank the generated fault effect contributions from the parent nodes according to the magnitude in a decreasing order for both directions, positive and negative
4. Apply the CUSUM method to the local fault effect contribution and the fault effect contributions from the parent nodes. Make a decision on fault detection and fault isolation

Firstly, the fault separation set (*FSS*) is formed as

$$FSS = \left\{ Y \left| IndexU_Y \neq \phi, \text{ and } \left| CU(GR_Y) \right| = 0 \right. \right\} \tag{3.6}$$

where $IndexU_Y = \{ i \left\| CU(GR_{U_i}) \right| = 1,\ U_i \in P_Y \}$ is the set of the indices of the node Y's predecessors, the global residuals of which have been identified in the fault detection. The symbol ϕ denotes the empty set.

In the second step, the different fault effect contributions are calculated for each node in the set *FSS*, if the *FSS* is not empty,

$$\begin{aligned} contp_Y^i &= GR_Y - ILR_Y^i, Y \in FSS, i \in IndexU_Y \\ contl_Y &= TLR_Y \end{aligned} \tag{3.7}$$

where $contp_Y^i$ is the fault effect contribution from the *i*-th predecessor, while the $contl_Y$ is the local fault effect contribution.

In the third step, the set of the positive contributions (PFE_Y) and the set of the negative contributions (NFE_Y) are formed as

$$\begin{aligned} PFE_Y &= \{ contp_Y^i \left| contp_Y^i > 0, i \in IndexU_Y \right. \} \\ NFE_Y &= \{ contp_Y^i \left| contp_Y^i < 0, i \in IndexU_Y \right. \} \end{aligned} \tag{3.8}$$

where the contributions in PFE_Y and NFE_Y are ranked according to the magnitude in their decreasing order.

In the fourth step, the CUSUM method is applied to the local fault effect contribution $contl_Y$, and the elements in the set PFE_Y and NFE_Y. The detection results are used for the fault detection and isolation. The algorithm is described as

1. Apply the CUSUM method to the local fault effect contribution $contl_Y$, the sum of the positive fault effect contribution $\sum_{i=1}^{lp} PFE_Y(i)$ and the sum of the negative fault effect contribution $\sum_{i=1}^{ln} NFE_Y(i)$, where $PFE_Y(i)$ and $NFE_Y(i)$ denote the *i*-th element in the sets PFE_Y and NFE_Y respectively. *lp* and *ln* are the number of the elements in these two sets. If none of these three contributions have been detected, the node *Y* is fault free, otherwise go to Step 2
2. If the local fault effect contribution $cont_l$ is detected, then the node *Y* is the fault origin.
3. If the sum of the positive fault effect contribution $\sum_{i=1}^{lp} PFE_Y(i)$ is detected, then the CUSUM method is applied to each positive fault effect contribution $PFE_Y(i)$, otherwise go to Step 5. If a set of elements $PFE_Y(i)$ are detected, then the fault is considered as detected and propagated from the corresponding parent nodes, otherwise go to Step 4
4. The CUSUM method is applied to the combined fault effect contributions $PFE_Y(1) + PFE_Y(2)$, $PFE_Y(1) + PFE_Y(2) + PFE_Y(3)$ and so on, until the first combined fault effect contribution is detected. The fault is then considered as detected and propagated from the corresponding parent nodes
5. For the negative fault effect set NFE_Y, repeat Steps 3-4

The above algorithm is illustrated in Figure 12.

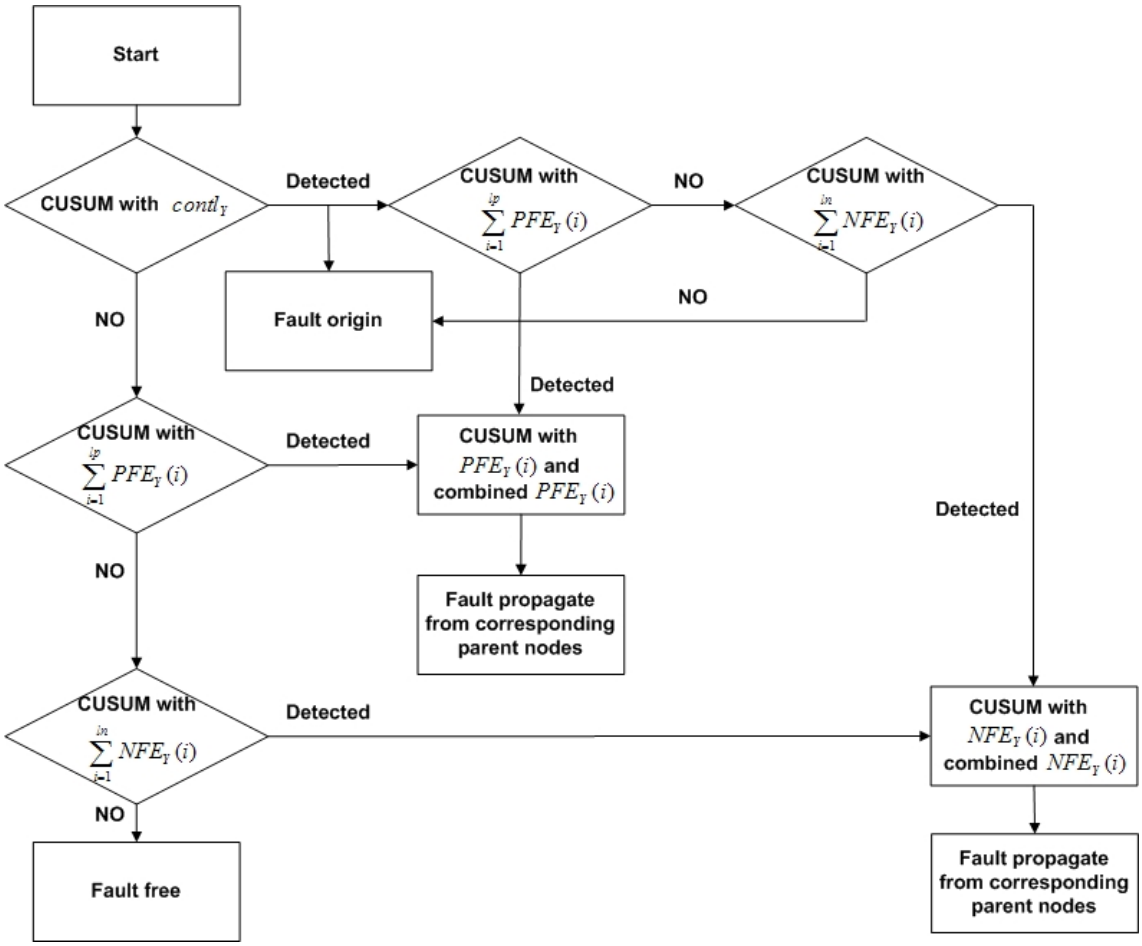

Figure 12. Separation algorithm of the fault effects.

3.1.5 Inference mechanism between the arcs

In the case of a process fault, which is assumed that only one process component is faulty simultaneously, in addition to locating the fault on the variables, locating it on the arcs is also desirable. However, the MISO structure of the digraph causes problems by generating spurious results. If one specific node Y with n input arcs in the digraph is identified as the fault origin for one process fault, then the number of sets of the suspected arcs, which can explain the fault on the node, is $2^n - 1$, $n \geq 1$. In the case

where a large number of input arcs exist, or there are more than one fault origins identified, then the number of sets of suspected arcs is very high. In order to decrease the number of spurious results, a new inference mechanism between the arcs is proposed for evaluating the sets of suspected arcs.

The idea behind the proposed inference mechanism is to test the consistency between the sets of the suspected arcs formed from the fault origins and the knowledge among the arcs. Due to the conservation constraints such as material or energy balances, an inconsistency between two variables will also usually result in inconsistencies between other variables when a process fault occurs. This knowledge is introduced into the digraph by an inter-arc knowledge matrix, and a consistency test is performed by matrix manipulations. Only the sets of the suspected arcs which are consistent with the knowledge matrix of the digraph are considered as possible results.

The inter-arc knowledge matrix of the whole digraph is formed in three steps:

1. Construct the inter-arc knowledge matrices for the output arcs of the same parent node.
2. Construct the inter-arc knowledge matrix for the whole digraph by merging the matrices generated in Step 1
3. Modify the inter-arc knowledge matrix of the whole digraph considering the knowledge between the arcs, which do not share the same parent node.

Due to the fact that the output arcs of the same parent node have closer locations and bigger effects on each other compared with other types of arcs, the inter-arc knowledge matrices for them are first derived from the process knowledge. For a node, U, in a digraph, the inter-arc knowledge matrix $\mathbf{M}_U$, describing the relationship between the output arcs, is specified as

$$\mathbf{M}_U(i,j) = \begin{cases} 1, \text{ if the inconsistent arc } < U, i > \\ \quad \text{results in the inconsistency of } < U, j > \\ 0, \text{ otherwise} \end{cases} \tag{3.9}$$

The dimension of the matrix $\mathbf{M}_U$ for a node U is $n \times n$, if n is the number of the output arcs which a node has. From the definition, the matrix $\mathbf{M}_U$ is not necessarily symmetric since the knowledge of the output arcs is directional.

Secondly, the knowledge matrix **M** for all the arcs in the digraph model is obtained by merging the knowledge matrices of every individual node in the digraph model, given as:

$$\mathbf{M} = \text{blockdiag}(\mathbf{M}_1, \mathbf{M}_2, \ldots, \mathbf{M}_q) \tag{3.10}$$

where q denotes the number of nodes that have output arcs in the digraph model. The knowledge matrix **M** has the dimension $N_a \times N_a$, where N_a is the number of arcs in the digraph, and each row or column represents one arc in the digraph.

The third step is to modify the matrix **M** obtained with Equation 3.10 considering the knowledge between the arcs which do not have the same parent nodes, given as

$$\mathbf{M}(i,j) = \begin{cases} 1, \text{ if the inconsistent arc } i \\ \quad \text{results in the inconsistency of } j \\ 0, \text{ otherwise} \end{cases} \tag{3.11}$$

where the arc i is the arc represented by the i-th row in the matrix **M**.

The consistency test between the sets of suspected arcs and the knowledge matrix **M** is performed by matrix manipulation. First, one row vector **sv** with length N_a is formed for one specific set of the suspected arcs:

$$\mathbf{sv}(i) = \begin{cases} 1, \text{if } \ ARC(\mathbf{M}, i) \in S, 1 \le i \le N_a \\ 0, \text{otherwise} \end{cases} \tag{3.12}$$

where $ARC(\mathbf{M}, i)$ gives the arc corresponding to the i-th row in the matrix **M**. The set S of the suspected arcs is evaluated by multiplying the row vector **sv** and the matrix **M** of the digraph. The set S is considered as a possible result only when the number of nonzero entries in the obtained row vector does not change when compared to the row vector **sv**:

$$NUM(\mathbf{sv}) = NUM(\mathbf{sv} \cdot \mathbf{M}) \tag{3.13}$$

where $NUM(\ )$ gives the number of nonzero entries in the vector.

Two important properties can be derived from Equation 3.13. Firstly, if there is no knowledge available about the output arcs, then the knowledge matrix **M** for the digraph will be the identity matrix, resulting in $\mathbf{sv} = \mathbf{sv} \cdot \mathbf{M}$. Thus Equation 3.13 will be satisfied for every set of suspected arcs and no spurious results can be removed from the possible results. Secondly, the knowledge matrix **M** usually consists of bidirectional knowledge, which means that if one faulty arc results in another faulty arc then the opposite is true. However, this is not always the case and a non-bidirectional knowledge matrix does exist. Moreover, the non-bidirectional knowledge matrix **M** produces more spurious results in the case that the process knowledge is not so certain. An example is given in

Table 3 for the node U with two output arcs. For the non-bidirectional knowledge matrix $\overline{\mathbf{M}}_U$ two sets of suspected arcs are accepted, while for the bidirectional knowledge matrix $\mathbf{M}_U$ only one set is accepted. On the other hand, the non-bidirectional knowledge matrix $\overline{\mathbf{M}}_U$ guarantees the correct fault diagnosis result in the case that the available process knowledge has uncertainty. From Table 3 it can be seen clearly that the second element in the first row of the matrix $\overline{\mathbf{M}}_U$ is defined as 0, if the concerning knowledge is uncertain. Furthermore, all the suspected sets accepted by the matrix $\mathbf{M}_U$ are also accepted by the matrix $\overline{\mathbf{M}}_U$, which means a correct fault diagnosis result has not been rejected. However, more spurious fault diagnosis results is produced with the matrix $\overline{\mathbf{M}}_U$.

Table 3. Comparison between a bidirectional and a non-bidirectional knowledge matrix.

Suspected sets	$\mathbf{M}_U = \begin{bmatrix} 1 & 1 \\ 1 & 1 \end{bmatrix}$	$\overline{\mathbf{M}}_U = \begin{bmatrix} 1 & 0 \\ 1 & 1 \end{bmatrix}$
[1 1]	Accepted	Accepted
[0 1]	Rejected	Rejected
[1 0]	Rejected	Accepted

Figure 13 illustrates the operation of the proposed inference mechanism between the arcs. The assumption is made that the nodes Y_2 and Y_3 are identified as fault origins for the process fault. The knowledge between the output arcs from the same node is first introduced into the digraph, provided that the arcs from different parent nodes do not have effect with each other:

$$\mathbf{M}_{U_1} = \begin{bmatrix} 1 & 0 \\ 1 & 1 \end{bmatrix}, \mathbf{M}_{U_2} = \begin{bmatrix} 1 & 1 \\ 1 & 1 \end{bmatrix} \Rightarrow \mathbf{M} = \text{blockdiag}(\mathbf{M}_{U_1}, \mathbf{M}_{U_2}) = \begin{bmatrix} 1 & 0 & 0 & 0 \\ 1 & 1 & 0 & 0 \\ 0 & 0 & 1 & 1 \\ 0 & 0 & 1 & 1 \end{bmatrix} \tag{3.14}$$

The corresponding arcs of each row of the matrix **M** are shown in Table 4.

Table 4. The list of arcs of the matrix **M** in Equation 3.14.

No.	Arcs	No.	Arcs
1	$<U_1, Y_1>$	3	$<U_2, Y_2>$
2	$<U_1, Y_2>$	4	$<U_2, Y_3>$.

Due to the fact that the node Y_2 has two input arcs, and the node Y_3 has one input arc, there are three sets of suspected arcs, $\{<U_1, Y_2>, <U_2, Y_2>, <U_2, Y_3>\}$, $\{<U_1, Y_2>, <U_2, Y_3>\}$ and $\{<U_2, Y_2>, <U_2, Y_3>\}$, which are possible results. For the first set, the **sv** vector is formed as [0 1 1 1] according to Equation 3.13 and Table 4. The result of the multiplication of **sv** and **M** is

$$NUM(\mathbf{sv}) = 3 \neq NUM(\mathbf{sv} \cdot \mathbf{M}) = NUM(\begin{bmatrix}1 & 1 & 2 & 2\end{bmatrix}) = 4 \tag{3.15}$$

The result vector has four nonzero entries while the **sv** vector only has three, which implies that the first set of suspected arcs cannot both explain the identified fault origins and be consistent with the knowledge between output arcs. For the same reason, the second set of arcs is excluded from the possible results. For the last set, **sv** vector is [0 0 1 1] and the result of the multiplication of **sv** and **M** is:

$$NUM(\mathbf{sv}) = 2 = NUM(\mathbf{sv} \cdot \mathbf{M}) = NUM(\begin{bmatrix}0 & 0 & 2 & 2\end{bmatrix}) \tag{3.16}$$

The result vector has two nonzero entries, and so has the vector **sv**, which indicates that the third set is the possible result. It can be seen that the proposed inference mechanism between the arcs is able to decrease the number of spurious sets of the suspected arcs.

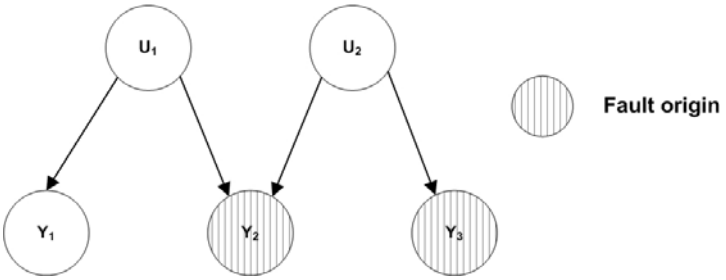

Figure 13. Example of inference between the arcs.

3.2 General procedure for applying the enhanced dynamic causal digraph method

In order to test and apply the proposed EDCDG method, the general procedure is presented in this section. The basic idea is illustrated in Figure 14. As can be seen from the figure, the application of the EDCDG method consists of four steps. The tasks of each step are introduced in detail in the following:

1. Process study. The main aim of this step is to obtain the process knowledge and fault-free data for subsequent causal digraph modelling. The related tasks are determination of the sub-process of interest for the study, the process dynamic phenomenon study, the variable selection of interest, the experiment design and fault-free data collection.

2. Causal digraph modelling. The main aim of this step is to establish the causal digraph model. The related tasks are causal structure identification, dynamic model selection for the description of the cause-effect relationships, identification of the selected model with fault-free data, and construction of the inter-arc knowledge matrix. The causal structure is preliminarily identified from the flowsheet of the process or the priori knowledge. Next, the model type selection and the model identification are performed with the obtained causal structure. These two tasks are generally dependent on the nature of the process dynamic. In the case that desired accuracy cannot be achieved, more arcs should

be introduced into the preliminary structure according to the fault-free data. However, the complexity of the causal structure is increasing with more arcs. Thus the trade off must be made between the causal digraph complexity and the accuracy. Furthermore, the first principle model type is preferred, if the model is available, due to the wide validity region. On the other hand, the data-driven model can be used to decrease the modelling time and effort, but its validity region should be kept in the mind always. Therefore, the general requirement for the causal digraph modelling, which can be used as criteria to guide the causal digraph modelling, are accuracy, complexity, and validity region.

3. Fault study. In this step, the main aim is to obtain the faulty data for the test and application purposes. The related tasks are determination of the faults of interest for the study, study of the effects of the individual faults, and collection of the faulty data from the process or simulator. In order to perform the EDCDG method, the variables in the causal digraph model need to be logged either from the process or from the dynamic simulator. However, first the probability to have the data from the processes during the period of the interesting fault is usually quite low. Moreover, the operators are definitely not favourable to make a fault in the processes on purpose. Thus, the dynamic simulator plays a critical role in the fault simulation. The requirement is that the simulator should be able to simulate the fault effects similar to the real processes.

4. Fault scenario diagnosis using the EDCDG method. The main aim of this step is to initiate the enhanced DCDG method with the causal digraph model, faulty data and the inter-arc knowledge matrix obtained from the above three steps. First, the residuals are generated by means of the digraph model and the faulty data. The residuals are modified for the better detection results using the fault effects separation approach. Next the residuals are evaluated by the CUSUM method for the detection. The detection results are then utilized by the inverse inference mechanism to locate the fault in the variables and to identify the nature of the fault. In the case of a process fault, the inter-arc knowledge matrix is used

by the inference mechanism between the arcs in order to locate the fault on the arcs and to identify the possible faulty process component.

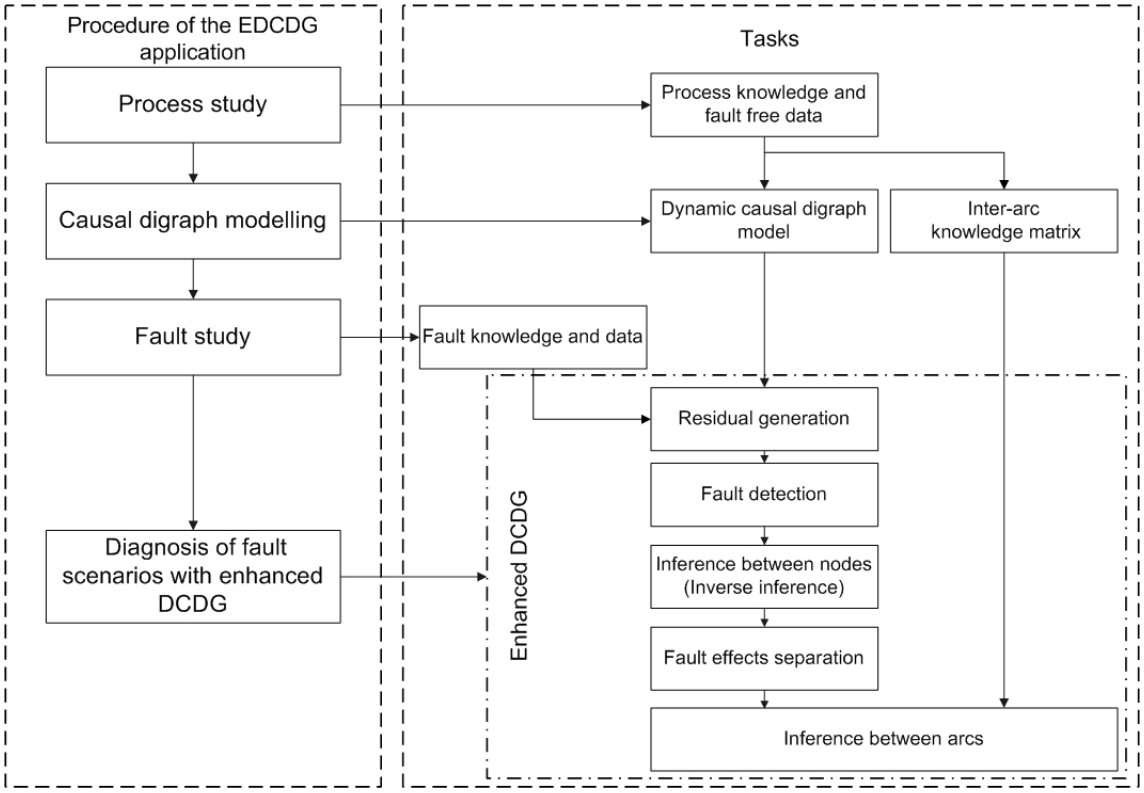

Figure 14. General procedure used in applying the EDCDG method.

4 Testing the EDCDG using a generic paper machine simulator

The proposed method was tested on the paper machine short circulation process, which was simulated using the Advanced Process Simulation Environment (APROS). The structure of this section follows the presented procedure: process study, causal digraph modelling, fault scenarios study, fault diagnosis and results.

4.1 Process study

In this section, the studied process is specified as short circulation, starting from the machine chest to the former section. The description of the process and the simulation environment are given as follows.

4.1.1 Description of the short circulation process

The short circulation is a crucial part of the papermaking process, with several important functions. The dilution of the fiber suspension entering the process to a suitable consistency for the headbox takes place in the short circulation, in a mixing process where low-consistency water from the wire pit is mixed with high-consistency stock. The second important task of the short circulation is the removal of impurities and air. This task is performed in the hydrocyclones, machine screens and the so-called deculator. The short circulation also improves the economy of the process because the valuable fibers and filler materials that pass through the wire are recycled. Being the intermediate process between the stock preparation and a former, the short circulation process is also very important for paper quality control, because the most important paper qualities such as basis weight, ash rate and fiber orientation are controlled in the short circulation process.

The short circulation process starts after the machine chest. The machine chest is usually followed by a thick stock pump and a basic weight valve, which is used for basis weight control. The thick stock from the machine chest is pumped to the wire pit and mixed with white water and filler under the control of the filler valve. The diluted stock is pumped by a fan pump via the hydrocyclones to the deculator where the air in the diluted stock is removed. The deculator has a continuous overflow to keep the inlet pressure constant for the head box feed pump. The diluted stock is then pumped into the hydraulic headbox and sprayed onto the wire at a constant speed, which is controlled by the hydraulic pressure produced by the headbox feed pump. On the wire the stock is dehydrated to form a wet web. About 93% of the water and 46% (paper machine specific) of the filler and fiber pass through the wire and flow to the wire pit as white water (Weise et al., 2000, pp. 134-135). The flowsheet of the process is presented in Figure 15.

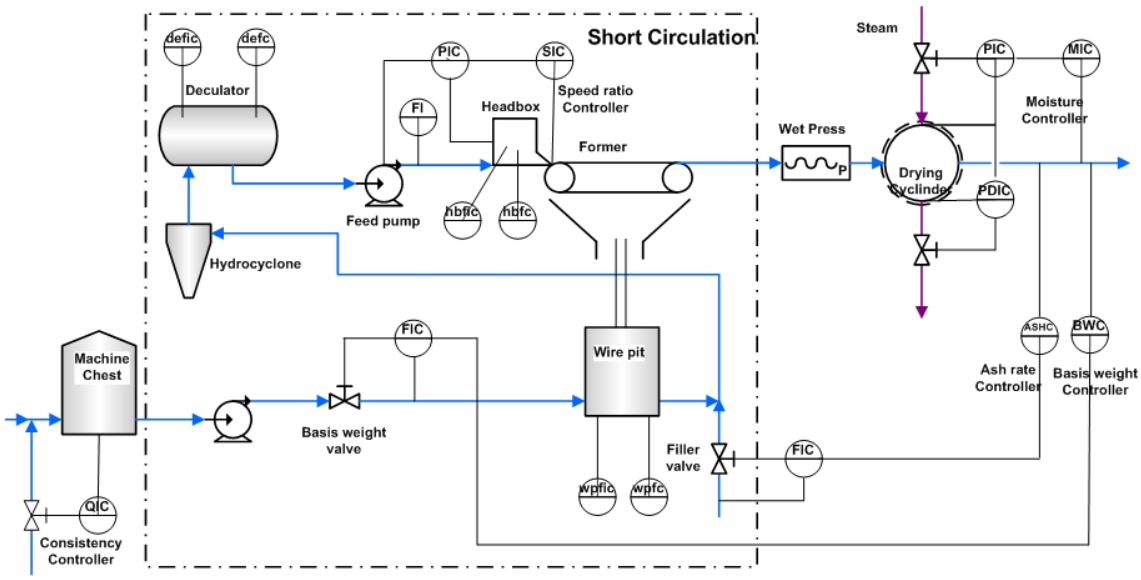

Figure 15. Flowsheet of the short circulation of the generic paper machine simulator.

The interesting measurements in the short circulation process and the paper quality measurements are listed in Table 5. All of these measurement signals were assumed to be available for fault diagnosis purposes.

Table 5. Description of the variables in the short circulation.

Variables	Description	Type	Unit
baval	Basis weight valve opening	Actuator	0−1
wpfc	Filler consistency in the wire pit	Measurement	%
wpfic	Fiber consistency in the wire pit	Measurement	%
fval	Filler adding valve opening	Actuator	0−1
defc	Filler consistency in the deculator	Measurement	%
defic	Fiber consistency in the deculator	Measurement	%
hbfc	Filler consistency in the headbox	Measurement	%
hbfic	Fiber consistency in the headbox	Measurement	%
feedpump	Headbox feed pump rotation	Actuator	%
totalflow	Mass flow into the headbox	Calculated value	kg/s
bw	Basis weight of paper	Measurement	g/m^2
ash	Ash consistency of paper	Measurement	%

4.1.2 Simulation environment

The method was tested in the APROS simulation environment developed by VTT (Technical Research Centre of Finland) in cooperation with former Imatran Voima (IVO), nowadays Fortum Oyj. It was developed within the Numerical Simulation of Processes research project carried out in VTT in 1986-1988, and reported by Silvennoinen et al.(1989). APROS was originally designed for and has been widely used in the power industry. The APMS (Advanced Paper Machine Simulator), or nowadays APROS Paper, was introduced by Tuuri, et al. (1995). APROS simulation software has extensive model libraries for modular model development and solution algorithms for different kinds of flow, heat and mass transfer processes (Silvennoinen et al. 1989; Laukkanen, 2001).

APROS Paper is a part of the APROS simulation software family. It provides validated model algorithms for the process components, such as equipment and automation, of the paper machine. These component models are mainly based on first principles. The simulation model is constructed by drawing the process flowsheet and setting up the parameters of the components (Lappalainen et al., 2003). The development of model

libraries of APROS Paper has been reported in many publications. For example, simulation of recovery boiler operations by Juslin and Tuuri (1992, cited in Juslin, 2005), simulation of displacement pulping process by Juslin and Pollari (1994, cited in Juslin, 2005), simulation of black liquor evaporation plant by Juslin and Niemenmaa (1994, cited in Juslin, 2005), modelling of a rotary lime kiln by Karhela et. al. (1998, cited in Juslin, 2005).

The structure of APROS Paper is presented in Figure 16. The major components are a graphical user interface, model libraries, calculation engine and communication interfaces.

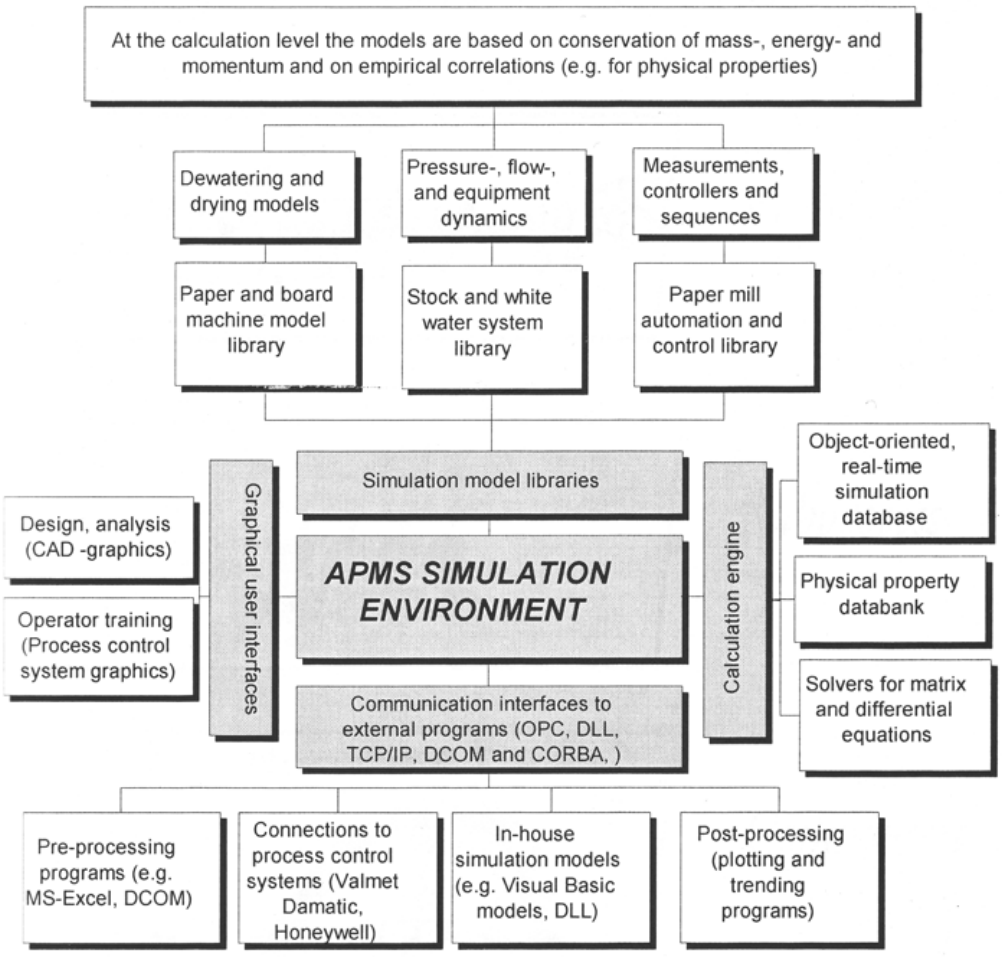

Figure 16. Structure of the APROS simulation environment (Laukkanen, 2001).

APROS uses Grades (developed by Process Vision) as a graphical user interface in the Windows operating system. In Grades, a user can construct models of processes in a CAD-like environment and also run and monitor simulations. Model libraries include model components for different unit operations of the pulp and paper industry, flow networks and automation systems. The calculation engine includes a real-time simulation database, a physical property database for different substances, and solvers for sparse matrices and differential equations. The communication interfaces are used for data transfer between the APROS simulator and external programs.

One built-in generic paper machine model was provided by VTT for the basic simulation. The control loops were added and the process components were parameterized according to a typical setup of the papermaking process (Weise et al., 2000, pp.131-136; Paulapuro, 2000, p.297), shown as Table 6.

Table 6. Setup of the paper machine simulator.

Name	Value	Unit/Description
Pulp recipe (Broke:CP:TMP)	30:21:49	
Fiber retention of the former	58	%
Filler retention of the former	50	%
Number of nips in wet press	3	Type: shoe
Linear pressure on the nips	70,90,120	kN/m
Steam supply pressure for dryer	500	kPa
Web speed	16	m/s
Web width	8	m
Paper basis weight	50	g/m^2
Paper ash rate	18	%
Paper moisture rate	7	%
Basis weight valve nominal pressure drop	30	kPa
Filler weight valve nominal pressure drop	100	kPa

Five control loops were added to the basic model in order to enable testing of the proposed method on the closed loop process. The control loop structure is shown in Figure 17 within the APROS paper machine environment. The consistency controller before the machine chest makes sure that the short circulation process receives a constant stock fed as material input. The paper quality variables, basis weight, ash rate and the moisture rate are controlled by the basis weight valve, the filler valve, and a set of steam valves respectively, all of which are in cascade control structures. Finally, the jet wire ratio is controlled by the centrifugal feed pump.

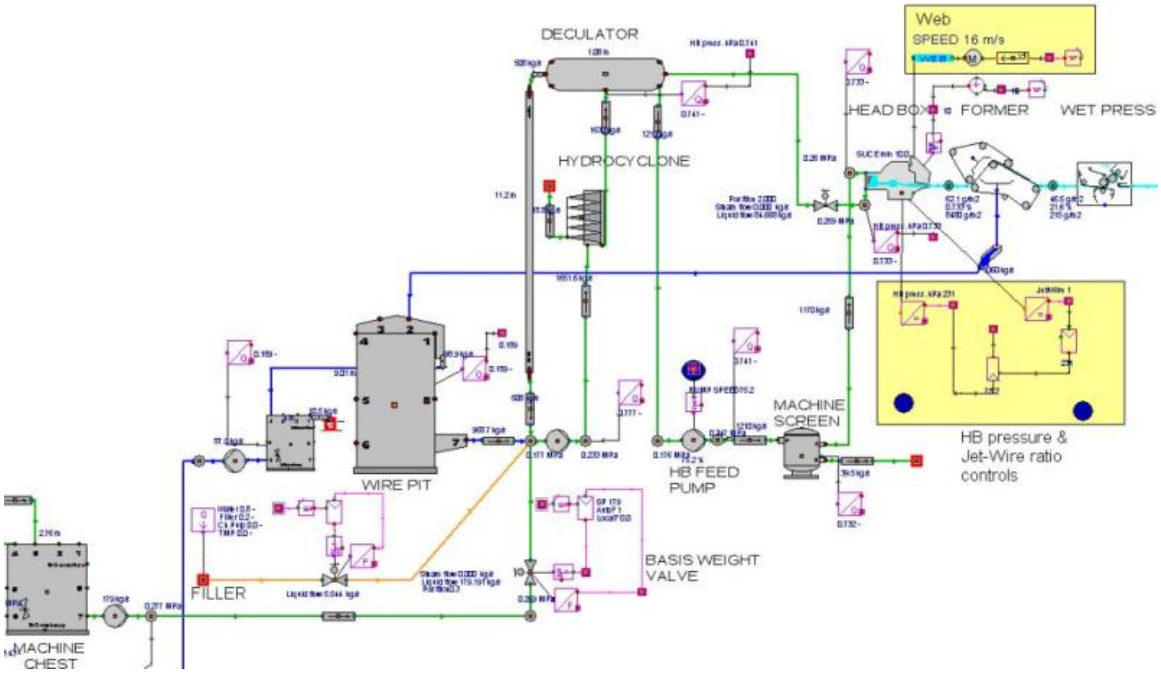

Figure 17. APROS paper machine model (VTT, 2005).

4.2 Dynamic causal digraph modelling

The process knowledge and fault-free data are used in this section to identify the causal structure and the cause-effect relationship models. In the case of the causal structure, the process knowledge concerning the relationship between the arcs is used to construct the inter-arc knowledge matrix.

4.2.1 Causal digraph construction

First, the causal structure of the short circulation process is determined according to the flowsheet. Due to the possible danger to introduce more arcs than necessary, special care is required to analyze the causal structure for variables evolving jointly. The process knowledge used for the causal digraph construction is shown as follows.

1. In the short circulation, the mass flow through the headbox *totalflow* is only determined by the rotation speed *feedpump*, with the assumption that the slice opening of the headbox is constant. The causal structure for the variable *totalflow* is therefore formed.
2. In the short circulation, the fibre consistency in the deculator *defic* is first determined by the basis weight valve opening *baval*, because *baval* affects the thick stock flow from the machine chest. Secondly, the fibre consistency in the wire pit *wpfic* has a direct effect on the variable *defic*. Thirdly, the filler valve opening *fval* has an effect on *defic*, because of the dilution effect of the filler flow. Finally, the mass flow through the headbox *totalflow* affects the overflow of the deculator which, in turn, influences the variable *defic* by changing the ration between the thick stock and white water.
3. The effect of the variable *defic* on the variable *hbfic* and the effect of the variable *hbfic* on the variable *wpfic* are clearly evident from the process flowsheet.
4. The basis weight *bw* of the paper is affected by the mass flow through the headbox, the fibre consistency and the filler consistency in the headbox, if it is assumed that the moisture of the paper is kept constant. The reason why the variable totalflow is not included in the input variables for the ash of the paper will be explained in connection with the fault-free simulation data.
5. Due to the similarity between the fibre and filler consistency in the deculator, headbox and wire pit, the causal structures for the variables *defc*, *hbfc* and *wpfc* are formed accordingly.

The idea used in constructing the causal digraph structure from the flowsheet is illustrated in Figure 18.

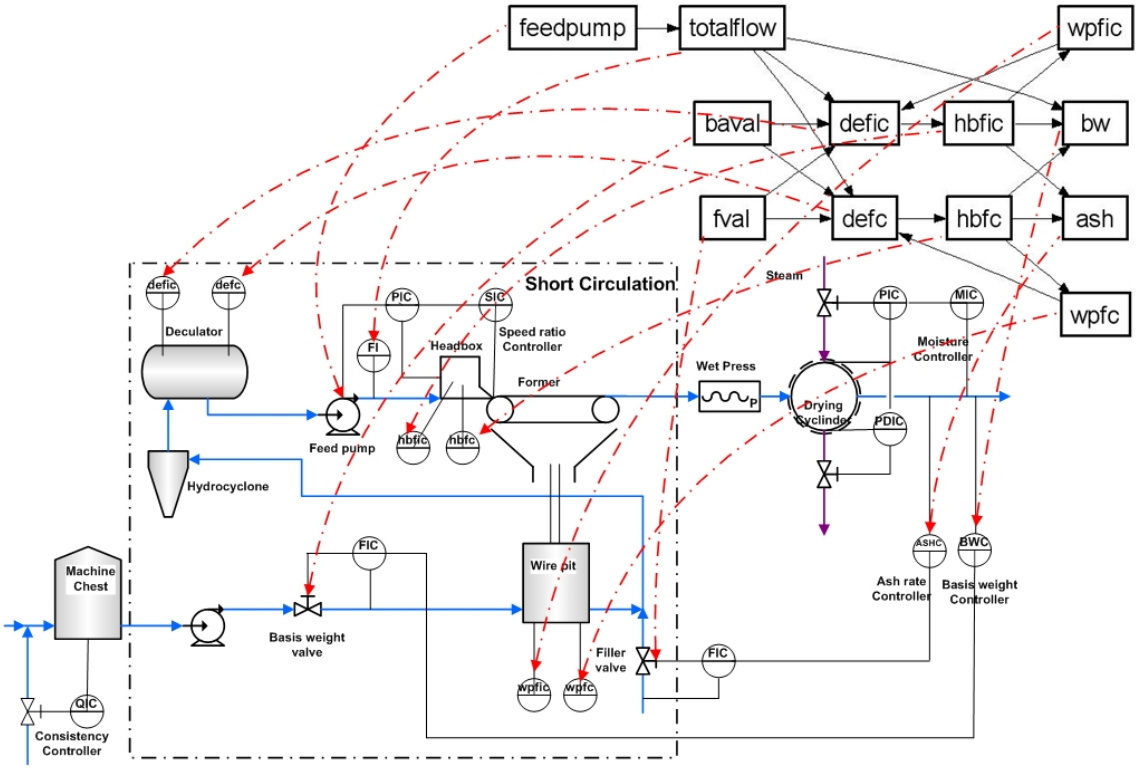

Figure 18. Causal digraph structure of the short circulation derived from the flowsheet.

After the structure of the causal digraph has been preliminarily chosen, the generic paper machine simulator is run in an open loop in order to collect fault-free data of the process, during which the basis weight valve, filler valve and feed pump for the headbox are adjusted manually as shown in Figure 19. The sampling time for the data log is 10 second.

The structure of the digraph is refined using the fault-free data. As can be seen in Figure 20, during the period 4 000-5 500 s the effect of the variable *totalflow* on *bw* is obvious, while that on the variable ash is negligible. Therefore, only the arc from the variable *totalflow* to the variable *bw* is needed. The final version of the causal structure is shown in Figure 18. The arcs in the digraph are numbered and shown in Table 7.

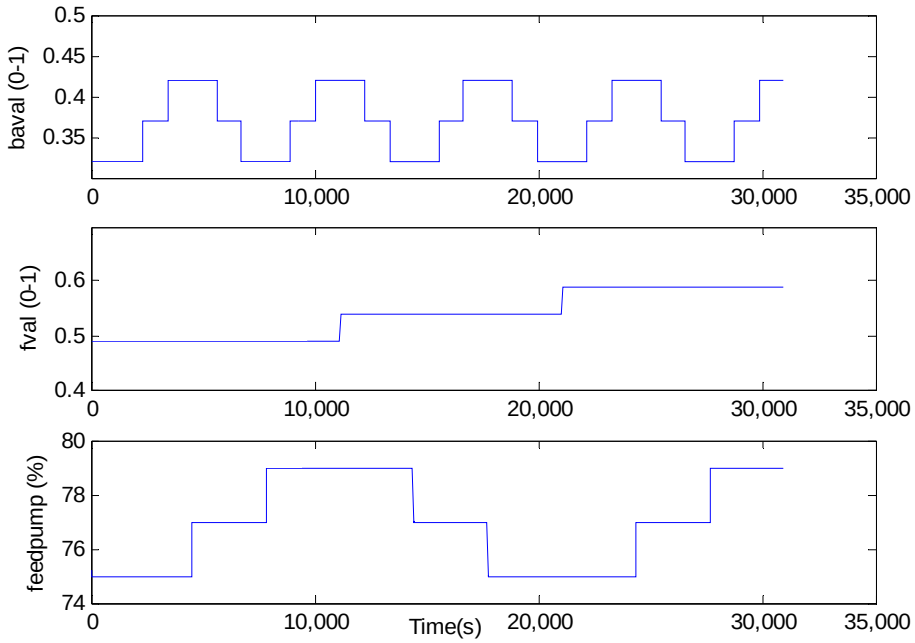

Figure 19. Actuator manipulation in fault-free simulation.

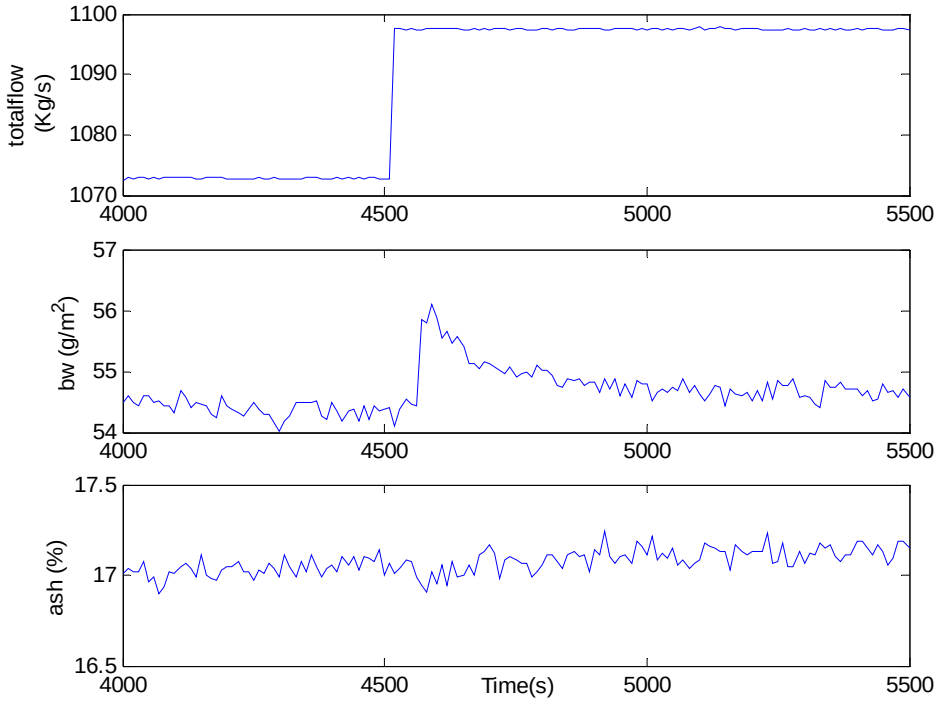

Figure 20. Variables *totalflow*, *bw*, and *ash* during the period 4 000-5 500 s.

Table 7 The list of the digraph arcs in Figure 18.

No.	Arcs	No.	Arcs	No.	Arcs
1	<*feedpump*, *totalflow* >	7	<*fval*, *defic*>	13	<*hbfic*, *ash*>
2	< *totalflow*, *bw*>	8	<*fval*, *defc*>	14	<*hbfc*, *bw*>
3	<*totalflow*, *defic*>	9	<*defic*, *hbfic*>	15	<*hbfc*, *ash*>
4	<*totalflow*, *defc*>	10	<*defc*, *hbfc*>	16	<*hbfc*, *wpfc*>
5	<*baval*, *defic*>	11	<*hbfic*, *wpfic*>	17	<*wpfic*, *defic*>
6	<*baval*, *defc*>	12	<*hbfic*, *bw*>	18	<*wpfc*, *defc*>

In order to evaluate whether linear state-space models can accurately describe the process behaviour, the linearity between related variables was tested in two ways with the fault-free data. For those variables that have only one input in the digraph in Figure 18, the steady points (input vs. output) were plotted and fitted to a straight line. For those variables that have more than one input, the linear regression model was constructed with the least square method for the steady-state data. The model outputs were then compared with the measurements. The result of the test according to the digraph structure indicated that the paper machine model used by APROS is relatively linear (Cheng et al., 2006) when the paper grade defined in Table 6 is produced.

The collected data were then used to obtain the cause-effect models. The linear discrete-time state space model was used for all the variables, except that the static linear regression model was used for the variable *totalflow*. Due to the fact that the transportation delay caused by the pipes is usually smaller than the sampling time of 10 second, the delays between the variables are not considered except for the delays from the input variables to *bw* and *ash*. In the paper machine simulator, the web length from the headbox to the basis weight scanner and the ash rate scanner is 254 meters, while the web speed is 16 m/s. The transportation delay was calculated to be around 15 second. Therefore, in the models for the variable *bw* and *ash*, one sample delay was used for the input variables.

For the linear discrete-time state space model identification, the collected data were first pre-processed by removing the steady state values. The model identification was carried out using the recurrent neural network. During the training, the hidden nodes were set up as linear nodes, while the biases for all the neuron nodes were set to zero. The software NNDT (Neural Networks Development Tool) was used for the training task (Saxén & Saxén, 1994). The obtained models are given in Table 8.

Table 8. State space models for the causal digraph of the short circulation process.

Nodes	*A*	*B*	*C*
totalflow	0	1.84	1.00
defic	$\begin{bmatrix} 3.35*10^{-2} & -0.253 \\ 5.60*10^{-3} & 5.14*10^{-2} \end{bmatrix}$ [1)]	$\begin{bmatrix} -0.245 & 0.196 \\ -3.42*10^{-3} & 4.34*10^{-3} \\ 8.48*10^{2} & -8.81*10^{2} \\ 8.70*10^{-4} & -6.90*10^{-4} \end{bmatrix}^T$	$\begin{bmatrix} -5.293*10^{-2} & -6.52*10^{-2} \end{bmatrix}$
hbfic	0.761	5.16	$4.56*10^{-2}$
wpfic	0.915	0.469	$7.50*10^{-2}$
defc	$\begin{bmatrix} 1.80 & 0.171 \\ -4.95 & -4.19*10^{-2} \end{bmatrix}$	$\begin{bmatrix} -0.479*10^{-2} & 0.270 \\ -0.260 & 1.46 \\ -3.44*10^{2} & 1.97*10^{4} \\ 1.73*10^{-3} & -9.97*10^{-3} \end{bmatrix}^T$	$\begin{bmatrix} -1.14*10^{-3} & -1.90*10^{-3} \end{bmatrix}$
hbfc	0.715	4.18	0.0684
wpfc	0.932	−2.80	−0.0124
ash	$\begin{bmatrix} 0.666 & 0.475 \\ -8.15*10^{-2} & 1.09 \end{bmatrix}$	$\begin{bmatrix} 3.54*10^{4} & 8.47*10^{4} \\ 2.74*10^{5} & 3.65*10^{3} \end{bmatrix}^T$	$\begin{bmatrix} 6.66*10^{-2} & -0.105 \end{bmatrix}$
bw	$\begin{bmatrix} 0.870 & 1.07*10^{-2} \\ 0.119 & 0.897 \end{bmatrix}$	$\begin{bmatrix} -3.78*10^{3} & 2.30*10^{3} \\ -2.69*10^{3} & 1.76*10^{3} \\ -0.157 & 0.126 \end{bmatrix}^T$	$\begin{bmatrix} -0.307 & 0.255 \end{bmatrix}$

[1)] In Table 8, only 3 digs are reported

4.2.2 Construction of the Inter-arc knowledge matrix

In order to perform the inference between the arcs, the inter-arc knowledge matrix needs to be formed according to Equation 3.9, 3.10 and 3.11. The knowledge matrices of

nodes with output arcs were formed first based on the process knowledge of paper machines.

For the node *totalflow* the knowledge matrix

$$\mathbf{M}_{totalflow} = \begin{bmatrix} 1 & 0 & 0 \\ 0 & 1 & 1 \\ 0 & 1 & 1 \end{bmatrix} \tag{4.1}$$

was formed. It represents the relationship between the arc <*totalflow*, *bw*>, <*totalflow*, *defic*> and <*totalflow*, *defc*>. It can be seen from the matrix $\mathbf{M}_{totalflow}$ that the inconsistency of the arc <*totalflow*, *bw*> does not result in an inconsistency of the other output arcs, since the arc <*totalflow*, *bw*> represents the cause-effect relationship between the mass flow through the headbox and the basis weight variable of the paper, and the arcs <*totalflow*, *defic*> and <*totalflow*, *defc*> are located before the headbox in the process. It can also been seen from the matrix $\mathbf{M}_{totalflow}$ that whenever one of the arcs <*totalflow*, *defic*> and <*totalflow*, *defc*> is faulty, then the other one is also faulty. This is based on the fact that, in the process, the relationship between the mass flow through the headbox and the fiber consistency in the deculator is correlated with the relationship between the mass flow and the filler consistency in the deculator, since they physically share the same pipe from the deculator.

For the node *baval* the knowledge matrix

$$\mathbf{M}_{baval} = \begin{bmatrix} 1 & 0 \\ 1 & 1 \end{bmatrix} \tag{4.2}$$

was formed. It represents the relationship between the arc <*baval*, *defic*> and <*baval*, *defc*>. Theoretically, if the actuator fault in the basis weight valve causes the inconsistency of <*baval*, *defic*> or <*baval*, *defc*>, then another arc should be faulty at the same time, since the relationship between the control signal and the mass flow through the basis weight valve changed due to the fault, thus subsequently changing the relationship on the arc <*baval*, *defic*> and <*baval*, *defc*>. However, the dilution effect represented by the arc <*baval*, *defc*> is relatively small compared to the effect of the arc <*baval*, *defic*>, such that the fault cannot always produce residuals on the node *defc* that are large enough for detection when the fault on the arc <*baval*, *defic*> produces large enough residuals for detection. On the other hand, if the fault on arc <*baval*, *defc*> is significant enough to detect, then the fault on <*baval*, *defic*> must be significant enough for detection. Based on the above, the noncommutative matrix in Equation 4.2 is used to represent the knowledge between the arc <*baval*, *defic*> and <*baval*, *defc*>. For the same reason, the matrix

$$\mathbf{M}_{fval} = \begin{bmatrix} 1 & 1 \\ 0 & 1 \end{bmatrix} \tag{4.3}$$

is used to represent the knowledge between arc <*fval*, *defic*> and <*fval*, *defc*>.

For the node *hbfc* the knowledge matrix

$$\mathbf{M}_{hbfc} = \begin{bmatrix} 1 & 1 & 1 \\ 1 & 1 & 1 \\ 1 & 1 & 1 \end{bmatrix} \tag{4.4}$$

was formed. It represents the relationship between the arc <*hbfc*, *bw*>, <*hbfc*, *ash*> and <*hbfc*, *wpfc*>. This sub matrix is obtained from the knowledge of the filler material

balance. Whenever the flow of the filler to the wire pit decreases or increases, the flow of the filler to the final production (*ash* and *bw*) increases or decreases. The same matrix is obtained for the arcs <*hbfic*, *bw*>, <*hbfic*, *ash*> and <*hbfic*, *wpfc*>.

For the nodes *feedpump*, *defic*, *defc*, *wpfic* and *wpfc*, which have only one output, the scalar 1 was assigned as their knowledge matrices.

The knowledge matrix **M** for the whole digraph is formed by merging these knowledge matrices for nodes as shown below:

$$\mathbf{M}_{feedpump} = 1;\ \mathbf{M}_{totalflow} = \begin{bmatrix} 1 & 0 & 0 \\ 0 & 1 & 1 \\ 0 & 1 & 1 \end{bmatrix};\ \mathbf{M}_{baval} = \begin{bmatrix} 1 & 0 \\ 1 & 1 \end{bmatrix};$$

$$\mathbf{M}_{fival} = \begin{bmatrix} 1 & 1 \\ 0 & 1 \end{bmatrix};\ \mathbf{M}_{defic} = 1;\ \mathbf{M}_{defc} = 1$$

$$\mathbf{M}_{hbfic} = \begin{bmatrix} 1 & 1 & 1 \\ 1 & 1 & 1 \\ 1 & 1 & 1 \end{bmatrix};\ \mathbf{M}_{hbfc} = \begin{bmatrix} 1 & 1 & 1 \\ 1 & 1 & 1 \\ 1 & 1 & 1 \end{bmatrix};\ \mathbf{M}_{wpfic} = 1;\ \mathbf{M}_{wpfc} = 1 \tag{4.5}$$

$$\mathbf{M} = \text{blockdiag}(\mathbf{M}_{feedpump}, \mathbf{M}_{totalflow}, \mathbf{M}_{baval}, \mathbf{M}_{fival}, \mathbf{M}_{defic}, \mathbf{M}_{defc}, \mathbf{M}_{hbfic}, \mathbf{M}_{hbfc}, \mathbf{M}_{wpfic}, \mathbf{M}_{wpfc})$$

The corresponding arcs of each row of the matrix **M** are shown in Table 7.

4.3 Study on the fault scenarios

Three different types of fault were introduced into the APROS paper machine model in sequence in order to test the proposed method. The first fault was an actuator basis weight valve fault. In the APROS model, the fault was introduced by increasing the parameter ‘nominal pressure drop’ of the basis weight valve from 30kPa to 36kPa. In

reality, the corresponding fault is a blockage of the basis weight valve due to a fiber flocculation phenomenon, which makes the opening of the valve's flow area smaller than normal.

The second fault introduced was a measurement fault on the fiber consistency in the deculator. A drift fault with a slope of $3.5*10^{-6}$%/s was added to the fault-free measurement *defic*.

The third fault introduced was a process fault, in which the filler retention of the former dropped. In the APROS model the fault was simulated by changing the retention setup for filler from 50% to 45%. Because of the smaller size of the filler compared to the fibers in the stock, the retention rate for the filler is relatively low. The decrease in the filler retention will directly affect the ash rate of the final paper. Although the quality control for the ash rate maintained the paper quality following the setpoint, the paper machine was running inefficiently. Furthermore the filler transportation ability was affected considerably. Moreover, since it is difficult to transfer filler to the final product, it will accumulate in the short circulation, which increases the wear of process devices like pumps, pipes and valves. As a result of the above, a filler retention drop fault can cause serious problems that require as early as possible detection and identification.

The total simulation time for three fault scenarios was 33 800 seconds (about 9.4 hours), and the sampling time was 10 seconds. The three faults were introduced into the simulator in sequence at the time intervals 1 800−5 800 s, 9 800−15 800 s and 17 800−25 800 s, respectively.

4.4 Fault diagnosis results obtained with the enhanced dynamic causal digraph method

With the causal digraph model obtained (See Figure 18 and Table 8 in Section 4.2.1), the inter-arc knowledge matrix (See Equation 4.5 in Section 4.2.2) and the faulty data obtained from the fault scenarios simulation in APROS, the proposed EDCDG method is applied. The procedures: residual generation, fault detection, fault isolation, fault effects separation and locating the fault on the arcs, have been gone through. The results for the three fault scenarios are presented as follows.

4.4.1 Fault diagnosis results for the actuator fault on the basis weight valve

A fault occurring in the basis weight valve will affect the whole paper machine through the short circulation process. Since the quality controller keeps the basis weight variable following the setpoint, the fault may be difficult to notice. With the causal digraph, however, the global residuals which test the consistency between the measurements and the globally simulated values were generated as shown in Figure 21. The global residuals are evaluated by the CUSUM method for detection purpose.

From Section 3.1.2, it can be seen that two parameters need to be set up for carrying out the CUSUM method. The minimal detectable fault β_0 is usually set from the point view of the user, while the parameter λ is defined according to the measurement noise level to make compromise between the miss alarm rate and the false alarm rate. For example, in this case study, the residual deviation which is bigger than $2g/m^2$ is considered as fault for the variable *bw*. Similarly, the minimal detectable fault 5kg/s, 1% and 0.01% are set for the variable *totalflow*, *ash* and all the consistency variables. The parameter λ is usually set as 5-10 times of the β_0 value for good detection results. The detection results in Figure 21 indicate that five variables in the digraph are suspected fault

candidates. The detection set was formed then by these five variables: *bw*, *ash*, *defic*, *hbfic*, and *wpfic*.

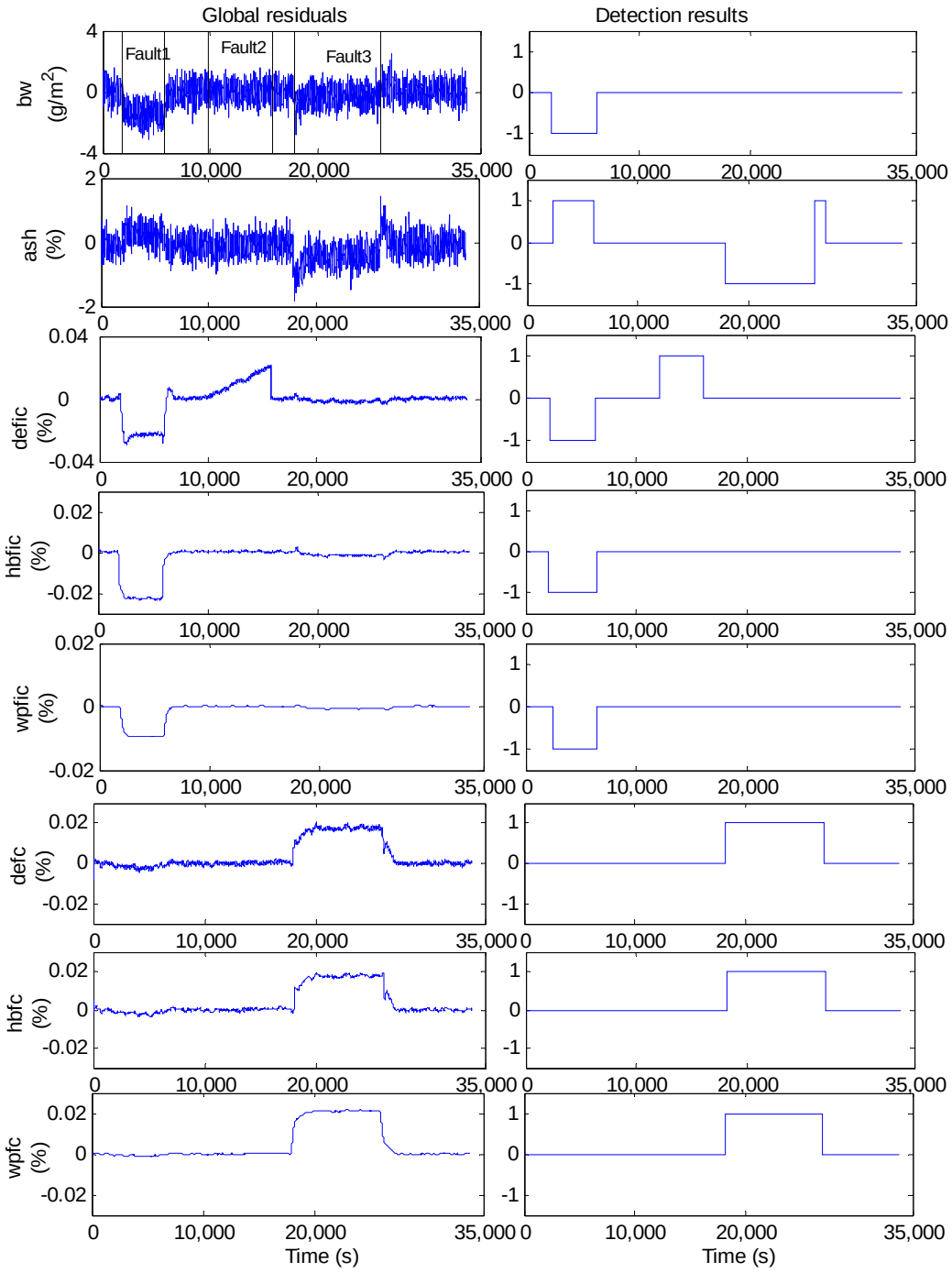

Figure 21. Global residuals for the variables *bw*, *ash*, *defic*, *hbfic*, *wpfic, defc, hbfic and wpfc.*

Next, the *LR*s are generated for the variables in the detection set and the fault isolation rules are applied. In the example shown in Figure 22, the TLR_{bw} indicates that during time 1 800−5 800 s the alarm on the variable *bw* is not local but originates from the parent nodes, while the TLR_{defic} indicates that *defic* is the fault origin. Moreover, the generated *ILR*s shown in Figure 23 imply that the alarm on *bw* is from the parent node *hbfic* during time 1 800−5 800 s. As the result of the fault isolation, the preliminary fault propagation path is formed as shown in Figure 24, where all the variables in the detection set have been processed.

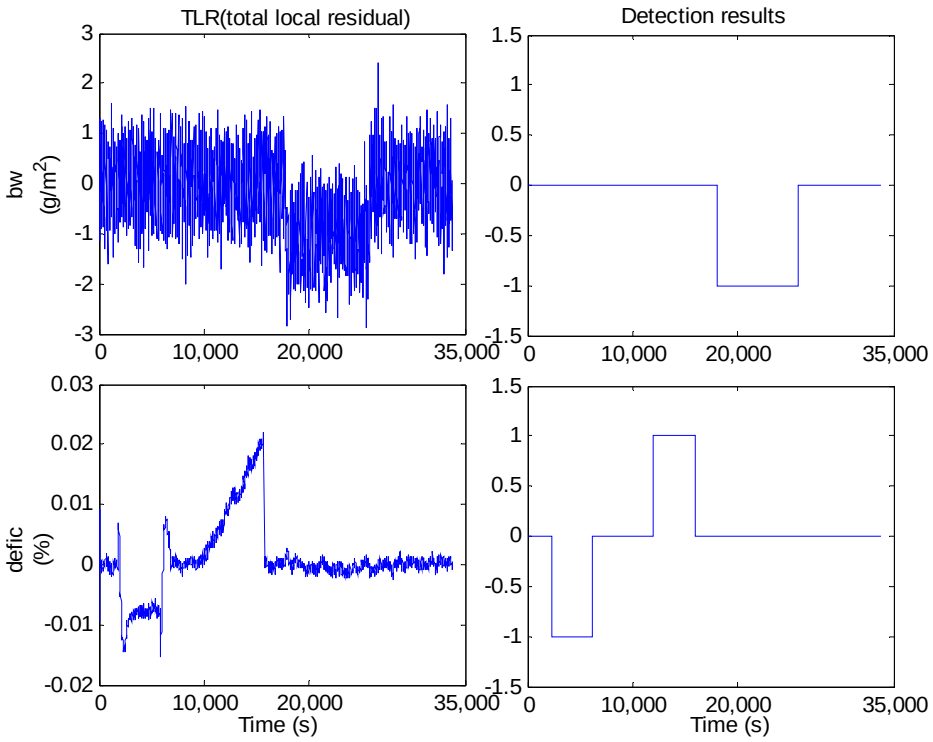

Figure 22. TLR_{bw} and TLR_{defic}.

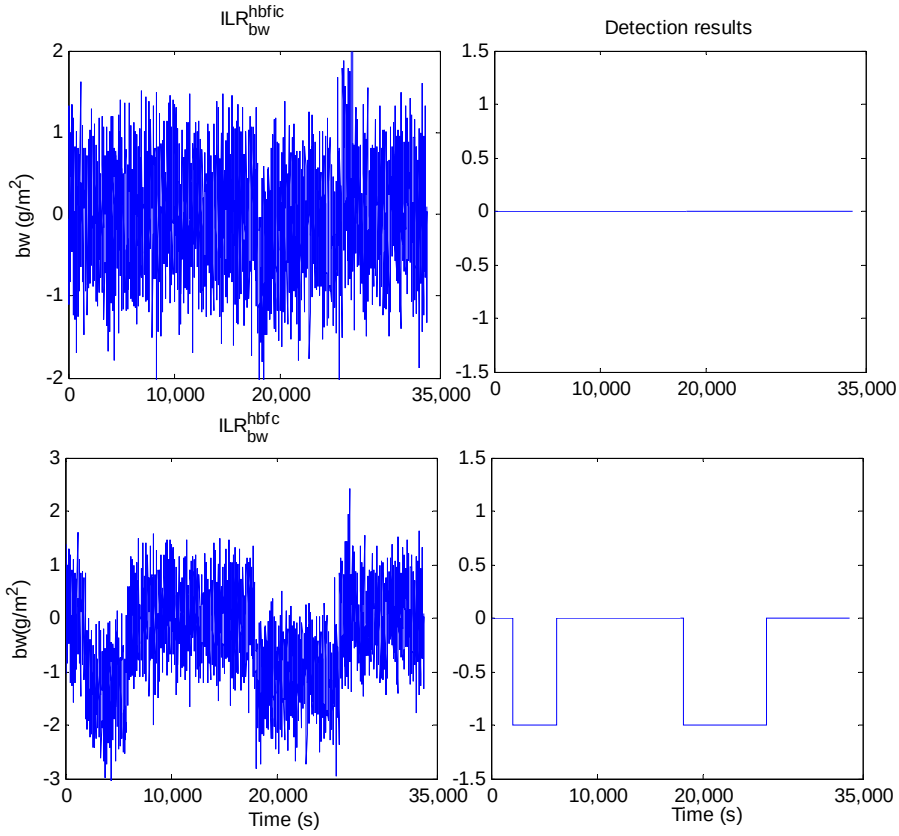

Figure 23. ILR_{bw}^{hbfic} and ILR_{bw}^{hbfc}.

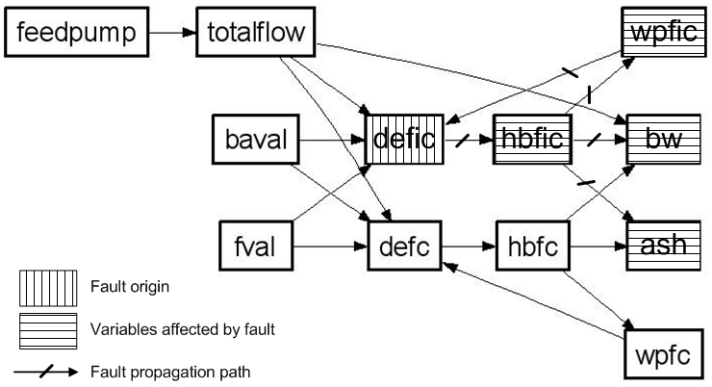

Figure 24. The preliminary fault propagation path for the time period 1 800−5 800 s.

The fault was identified as a process fault by the nature rules: it propagated globally through the digraph and this studied fault is the blockage of the basis weight valve which is considered as a component in the process. Thus, the approach for separating fault effects is applied to the variables whose parent nodes have global detections. The

fault separation set *FSS* was first formed as an empty set according to Equation 3.6. Therefore, the separation approach for different fault effects was not needed, while the preliminary fault propagation path in Figure 24 keeps unchanged.

Since the identified fault is a process fault, locating the process fault on the arc is performed in order to find the responsible process component. However, spurious results were produced due to the MISO structure of the digraph. In Figure 24, the input arcs for fault origin node *defic* are <*totalflow*, *defic*>, <*baval*, *defic*>, <*fval*, *defic*> and <*wpfic*, *defic*>. Thus the number of sets of suspected arcs is $\left(2^4-1\right)=15$, which are {<*totalflow*, *defic*>}, {<*totalflow*, *defic*>, <*baval*, *defic*>}…

With the inter-arc knowledge matrix **M** given in Equation 4.5, the 15 sets of suspected arcs were tested with Equation 3.13. The set of suspected arcs {<*totalflow*, *defic*>, <*baval*, *defic*>, <*fval*, *defic*>} is considered as an example. The **sv** for this set is

$$\mathbf{sv}=\begin{bmatrix}0 & 0 & 1 & 0 & 1 & 0 & 1 & 0 & 0 & 0 & 0 & 0 & 0 & 0 & 0 & 0 & 0 & 0\end{bmatrix} \tag{4.6}$$

and the test with Equation 3.13 is performed as follows:

$$\begin{aligned} &NUM(\mathbf{sv})=3\neq NUM(\mathbf{sv}\cdot\mathbf{M})= \\ &NUM\left(\begin{bmatrix}0 & 0 & 1 & 1 & 1 & 0 & 1 & 1 & 0 & 0 & 0 & 0 & 0 & 0 & 0 & 0 & 0 & 0\end{bmatrix}\right)=5 \end{aligned} \tag{4.7}$$

Thus the set {<*totalflow*, *defic*>, <*baval*, *defic*>, <*fval*, *defic*>} cannot be a possible result. The set {<*baval*, *defic*>, <*wpfic*, *defic*>} is considered as another example. The **sv** for the set is

$$\mathbf{sv} = \begin{bmatrix} 0 & 0 & 0 & 0 & 1 & 0 & 0 & 0 & 0 & 0 & 0 & 0 & 0 & 0 & 0 & 0 & 1 & 0 \end{bmatrix} \tag{4.8}$$

and the test with Equation 3.13 is performed as follows:

$$\begin{aligned} &NUM(\mathbf{sv}) = 2 \neq NUM(\mathbf{sv} \cdot \mathbf{M}) = \\ &NUM(\begin{bmatrix} 0 & 0 & 0 & 0 & 1 & 0 & 0 & 0 & 0 & 0 & 0 & 0 & 0 & 0 & 0 & 0 & 1 & 0 \end{bmatrix}) = 2 \end{aligned} \tag{4.9}$$

Thus this set is accepted as a possible result. After the test of all the sets of suspected arcs, only three of them were left as possible results: {<*baval*, *defic*>} and {<*baval*, *defic*>, <*wpfic*, *defic*>} and {<*wpfic*, *defic*>}. The number of possible results is decreased from 15 to 3 by using the inference mechanism between the arcs.

The fault diagnosis results, i.e. the three sets of suspected arcs, provide valuable information for identifying the faulty process component in the case of an actuator fault, which is considered to be a special case of process fault. The arc in the first set is <*baval*, *defic*>, which corresponds to the process components: a basis weight valve and a hydrocyclone. Similarly, for the second set of suspected arcs, the hydrocyclone is suspected since it is located on both of the two arcs; for the third set of suspected arcs, only the hydrocyclone is suspected to be faulty. So the possible faulty process components are the basis weight valve and hydrocyclone. Moreover, the direction of the TLR_{defic}, as shown in Figure 22, indicates that the direction of the fault is negative, which implies that the fiber transport ability to the deculator has decreased. The reason for this could be either that the flow area of the basis weight valve has decreased or that the acceptance rate of fiber in the hydrocyclone has decreased.

4.4.2 Fault diagnosis results for the sensor fault on the fiber consistency of the deculator

The second faulty scenario is a measurement fault for the fiber consistency in the deculator. It was simulated during the time period 9 800−15 800 s. The *GR*s shown in Figure 21 indicate that, during this time period, only the variable *defic* produced an alarm. The generated TLR_{defic} in Figure 22 indicates that the variable *defic* is the fault origin according to the fault isolation rules. With the fault nature rules it can be inferred that it is a measurement fault. Finally, the fault propagation path for the time period (9 800−15 800 s) is shown as the fault diagnosis result in Figure 25.

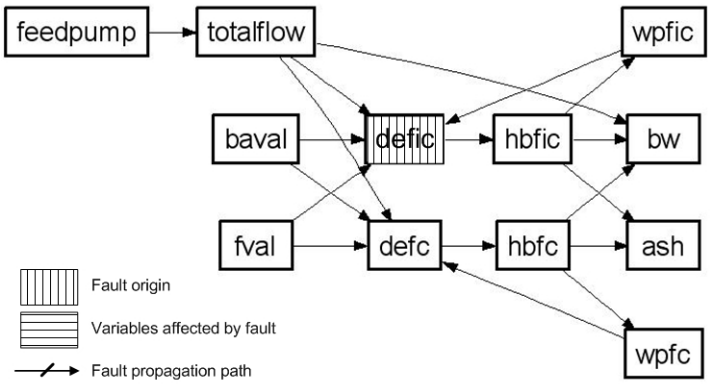

Figure 25. Fault diagnosis results for the time period (9 800−15 800 s).

In this sensor fault case, the fault detection and isolation results were the same for both the proposed method and the conventional method. Due to the nature of the fault, neither the fault separation nor the inference between the arcs was performed.

4.4.3 Fault diagnosis results for the process fault of the filler retention drop in the former section

The third fault scenario is a retention drop of filler on the former, which can be characterized as a process fault. The fault was simulated during the time period 17

800−25 800 s. The variables *ash*, *defc*, *wpfc*, *hbfc* were detected from the *GR*s shown in Figure 21 for the period 17 800−25 800 s, and the detection set was formed.

Next, *LR*s are generated for the variables in the detection set and fault isolation rules are applied. In Figure 26, the TLR_{ash} and TLR_{wpfc} indicate that during time 17 800−25 800 s the alarm on the variable *ash* and *wpfc* are local, while the ILR_{defc}^{wpfc} and ILR_{hbfc}^{defc} indicate that the variables *defc* and *hbfc* are not the fault origin. As the results of the fault isolation result, the preliminary fault propagation path is shown in Figure 24, where all the variables in the detection set have been processed.

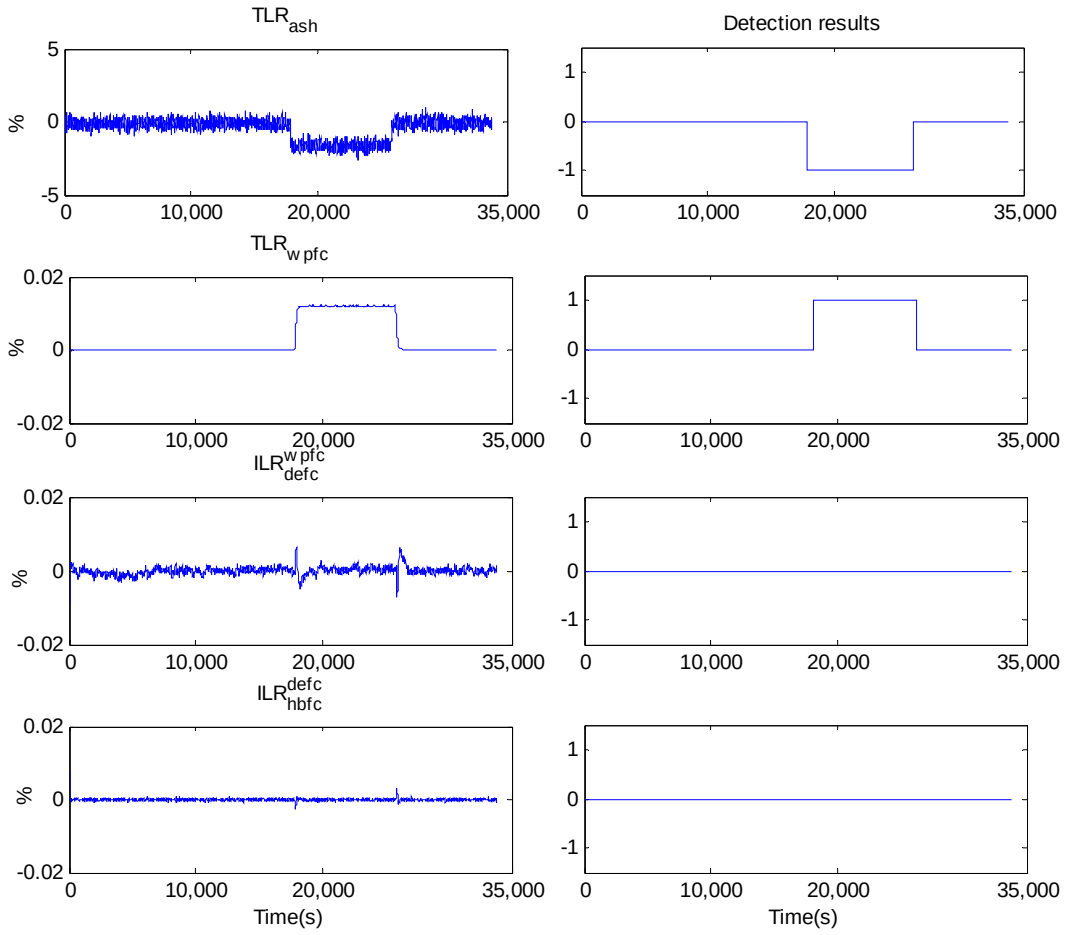

Figure 26. TLR_{ash}, TLR_{wpfc}, ILR_{defc}^{wpfc} and ILR_{hbfc}^{defc}.

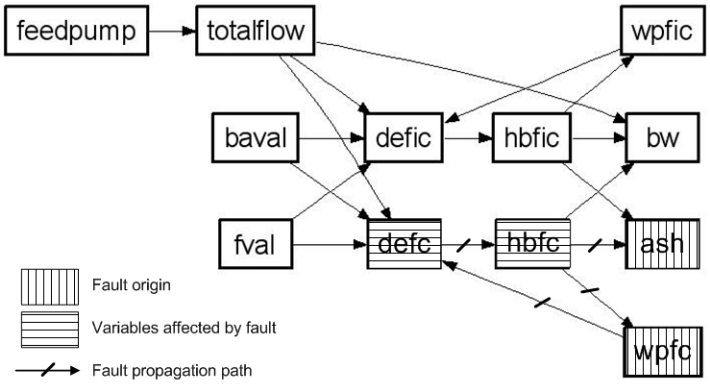

Figure 27. The preliminary fault propagation path for the time period (17 800−25 800 s).

The fault was identified as a process fault by the nature rules: it propagated globally through the digraph. Thus, the approach for separating fault effects was applied to the variables whose parent nodes have global detections. The fault separation set $FSS = \{bw\}$ was first formed according to Equation 3.6 with $IndexU_{bw} = \{hbfc\}$. Secondly, the different fault effects were calculated for the variable *bw* as

$$\begin{aligned} contp_{bw}^{hbfc} &= GR_{bw} - ILR_{bw}^{hbfc} \\ contl_{bw} &= TLR_{bw} \end{aligned} \tag{4.10}$$

The generated fault effect contributions for the variables *bw* are shown in Figure 28.

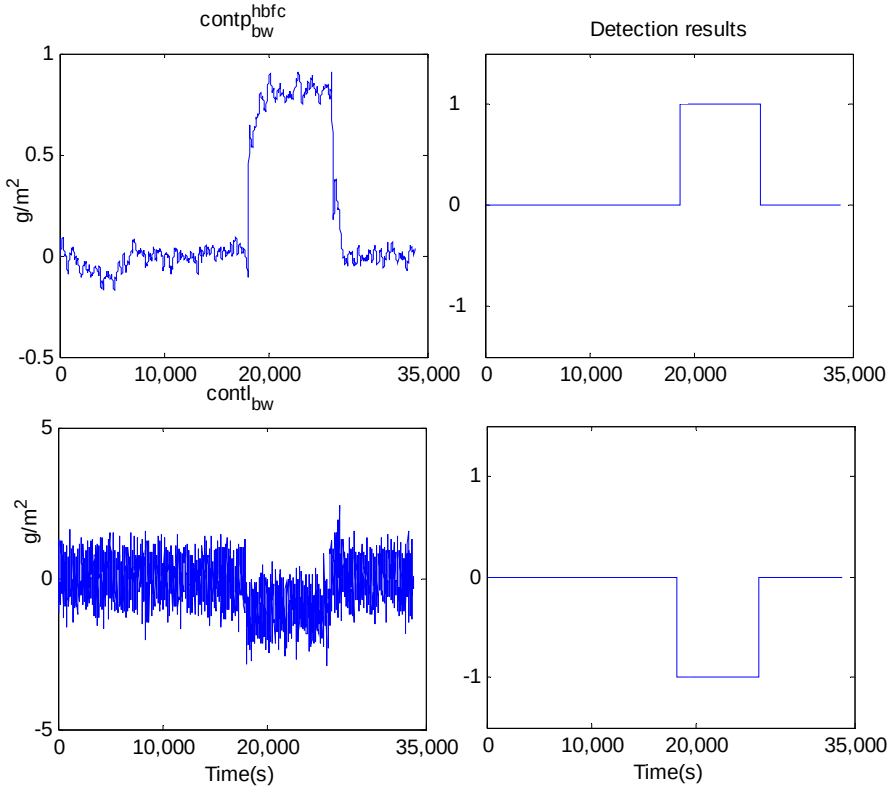

Figure 28. $contp_{bw}^{hbfc}$ and $contl_{bw}$.

Thus in the third step of the fault effect separation, the set PFE_{bw} is formed as $\left\{contp_{bw}^{hbfc}\right\}$, while the set NFE_{bw} is a empty set.

In the fourth step, the CUSUM method was applied to the local fault effect contribution $contl_{bw}$ and the element in the set PFE_{bw} according to the algorithm in Figure 12. The detection results shown in Figure 28 indicate that there are two fault effects on the variable *bw*. The first one is the fault effect propagated from the variable *hbfc* with the positive direction, while the second fault is the local fault on the variable *bw* itself with the negative direction. The cancellation of these two fault effects makes the global residual of the variable *bw* disappear, which is shown in Figure 21. Therefore, the preliminary fault propagation path in Figure 27 was then modified as presented in Figure 29.

Since the identified fault is a process fault, locating the process fault on the arcs is performed in order to find the responsible process component. However, spurious results were produced due to the multiple fault origins and multiple input arcs for each fault origin. In Figure 29 the input arcs for fault origin nodes *wpfc*, *bw*, *ash* are {<*hbfc*, *wpfc*>}, {<*totalflow*, *bw*>, <*hbfic*, *bw*>, <*hbfc*, *bw*>} and {<*hbfic*, *ash*>, <*hbfc*, *ash*>}, respectively. Thus the number of sets of suspected arcs is $1 \cdot (2^2 - 1) \cdot (2^3 - 1) = 21$, which are {<*hbfc*, *wpfc*>, <*totalflow*, *bw*>, < *hbfc*, *ash*>}, {<*hbfc*, *wpfc*>, <*hbfic*, *bw*>, <*hbfic*, *ash*>}…

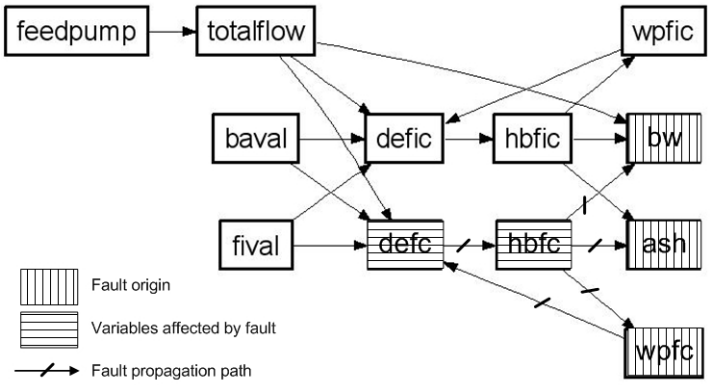

Figure 29. Fault propagation path for the time period (17 800−25 800 s).

With the knowledge matrix **M** given in Equation 4.5, the 21 sets of suspected arcs were tested with Equation 3.13. The set of suspected arcs {<*hbfc*, *wpfc*>, <*hbfic*, *ash*>, <*hbfic*, *bw*>} is considered as an example. The **sv** for this set is

$$\mathbf{sv} = \begin{bmatrix} 0 & 0 & 0 & 0 & 0 & 0 & 0 & 0 & 0 & 0 & 0 & 1 & 1 & 0 & 0 & 1 & 0 & 0 \end{bmatrix} \tag{4.11}$$

and the test with Equation 3.13 is performed as follows:

$$NUM(\mathbf{sv}) = 3 \neq NUM(\mathbf{sv} \cdot \mathbf{M}) = NUM([0 \quad 0 \quad 0 \quad 0 \quad 0 \quad 0 \quad 0 \quad 0 \quad 0 \quad 0 \quad 2 \quad 2 \quad 2 \quad 1 \quad 1 \quad 1 \quad 0 \quad 0]) = 6 \tag{4.12}$$

Thus the set {<*hbfc*, *wpfc*>, <*hbfic*, *ash*>, <*hbfic*, *bw*>} cannot be a possible result. The set {<*hbfc*, *wpfc*>, <*hbfc*, *ash*>, <*hbfc*, *bw*>} is considered as another example. The **sv** for the set is

$$\mathbf{sv} = [0 \quad 0 \quad 0 \quad 0 \quad 0 \quad 0 \quad 0 \quad 0 \quad 0 \quad 0 \quad 0 \quad 0 \quad 0 \quad 1 \quad 1 \quad 1 \quad 0 \quad 0] \tag{4.13}$$

and the test with Equation 3.13 is performed as follows:

$$NUM(\mathbf{sv}) = 3 = NUM(\mathbf{sv} \cdot \mathbf{M}) = NUM([0 \quad 0 \quad 0 \quad 0 \quad 0 \quad 0 \quad 0 \quad 0 \quad 0 \quad 0 \quad 0 \quad 0 \quad 0 \quad 3 \quad 3 \quad 3 \quad 0 \quad 0]) = 3 \tag{4.14}$$

Thus this set is accepted as a possible result. After the test of all the sets of suspected arcs, only two were left as possible results: {<*hbfc*, *wpfc*>, <*hbfc*, *ash*>, <*hbfc*, *bw*>} and {<*hbfc*, *wpfc*>, <*hbfc*, *ash*>, <*hbfc*, *bw*>, <*totalflow*, *bw*>}. The number of possible results decreased from 21 to 2 by using the inference mechanism between the arcs.

The fault diagnosis results, i.e. the two sets of suspected arcs, provide valuable information in identifying the faulty process component in the case of a process fault. The first arc in the first set {<*hbfc*, *wpfc*>, <*hbfc*, *ash*>, <*hbfc*, *bw*>} is <*hbfc*, *wpfc*>, which corresponds to the process components: a former section and the white water tray. Similarly, the arcs <*hbfc*, *ash*> and <*hbfc*, *bw*> correspond to the process components: a former section, a wet press and a drying group. Thus the suspected process component is the former section, since it is located on all three arcs. The same result is obtained from the second set. Moreover, the results also indicated that the fault occurred for the

filler material but not for the fiber material. Finally, the direction of the TLR_{wpfc}, as shown in Figure 26, implies that the direction of the fault is the drop in the filler retention, rather than an increase in the filler retention.

5 Testing of the EDCDG using the three-layered board machine simulator

In this chapter, the proposed enhanced dynamic causal digraph method is further tested on a more complex process, the three-layered board machine of the Stora Enso Kaukopää mills in Imatra, Finland. The simulator model of the board machine constructed in the APROS Environment is used for the test. The structure of this section follows the general application procedures of the method: process study, causal digraph modelling, fault scenario study, fault diagnosis and results.

5.1 Process study

This test focuses on the board machine at Stora Enso Kaukopää mills in Imatra, Finland. The board machine produces 210 000 tonnes of three-layered, uncoated and coated liquid packaging boards, graphical boards and folding box boards per year. The basis weight varies from 170 to 400 g/m^2. The board machine was originally built already in 1956, but it was upgraded in 1990 when a new top wire unit was installed in the former section, and in 2005 when parts of the automation system were updated. The width of the web is 5.6 m and the maximum production speed is 550 m/min. The board machine uses hardwood and softwood kraft pulp, chemi-thermomechanical pulp (CTMP) and broke as raw materials (Metso Automation, 2007).

The part of the board machine tested extends from the stock preparation to the end of the former section. The main emphasis is on stock preparation, short circulation and the wet end of the board machine, which are the most critical parts of the process, because most of the properties of the end product are determined by the phenomena that take place here.

The board making process and the unit operations of a board machine are described in this section. Some features of the board machine model in APROS are also introduced.

5.1.1 Process description of the three-layered board machine

Paper and board making processes start from stock preparation, the purpose of which is to provide the board machine the required amount of stock with uniform quality and minimum variations (Weise et al., 2000, p.125).

The first stage is refining, where the raw materials are processed to obtain the desired properties of the stock. Refining is a mechanical treatment to modify the fibres so that they can be formed into a paper or board grade with specific properties (Lumiainen, 2000, p.87).

Refining is followed by blending, where the different pulps are mixed and the final composition of fibres is achieved. The composition in this part of the process is not the final one of the product, because more components will be added later on in the process. Blending is carried out in a blend chest, into which the pulps are portioned according to a specific recipe. The mixture is then pumped to a machine chest while the consistency is controlled by dilution water. The machine chest has an overflow back to the blend chest so that its level can be kept constant.

The APROS Stora Enso board machine model used in this study starts from the pulp storage chests immediately before refining. They are used as boundary conditions for the simulations so that they supply stock of constant quality to the blending. The boundary conditions include the temperature, consistency of the stock and the level in the chests (Lappalainen, 2003). The flowsheet of the stock preparation of layer 2 of the board machine is presented in Figure 30.

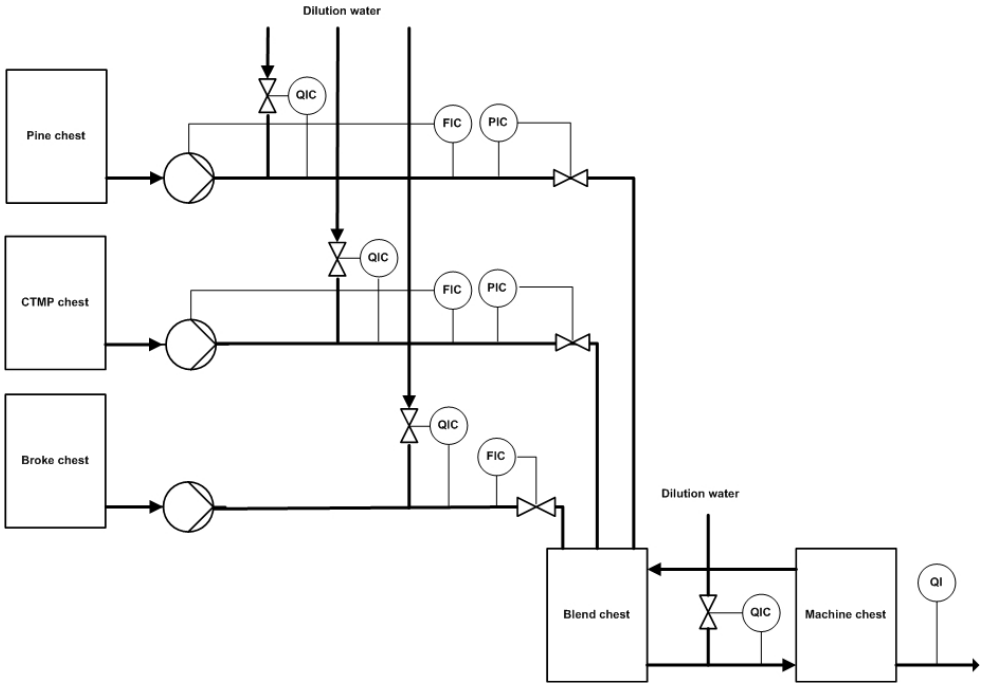

Figure 30. Flowsheet of stock preparation of layer 2 of the Stora Enso board machine (Stora Enso Oyj, 2002).

The blended stock is then delivered to the short circulation, which is described in Section 4.1.1. A flowsheet of the short circulation process is presented in Figure 17. However, the multi-layered board machine differs from conventional paper machines because they have multiple short circulations and headboxes – one for each layer. In the case of studied board machine, there are three layers. The short circulations of layers 1 and 3 are for the top and the bottom layers, respectively, and the second one is for the middle layer. In the board machine model the short circulations of layers 1 and 3 are almost identical. They both have a four-stage centrifugal cleaning plant, while the second has only a three-stage one. This is due to the lower quality requirement of the middle layer stock. As it is not visible in the end product there is no need for any stringent cleaning. Furthermore, in the board machine the deculator is removed from the short circulation. Finally, due to the similarity of the pulp used for layers 1 and 3, one stock preparation section is shared by the two layers, and layer 2 has its own stock preparation process. The structure of the short circulations of the board machine is shown in Figure 31.

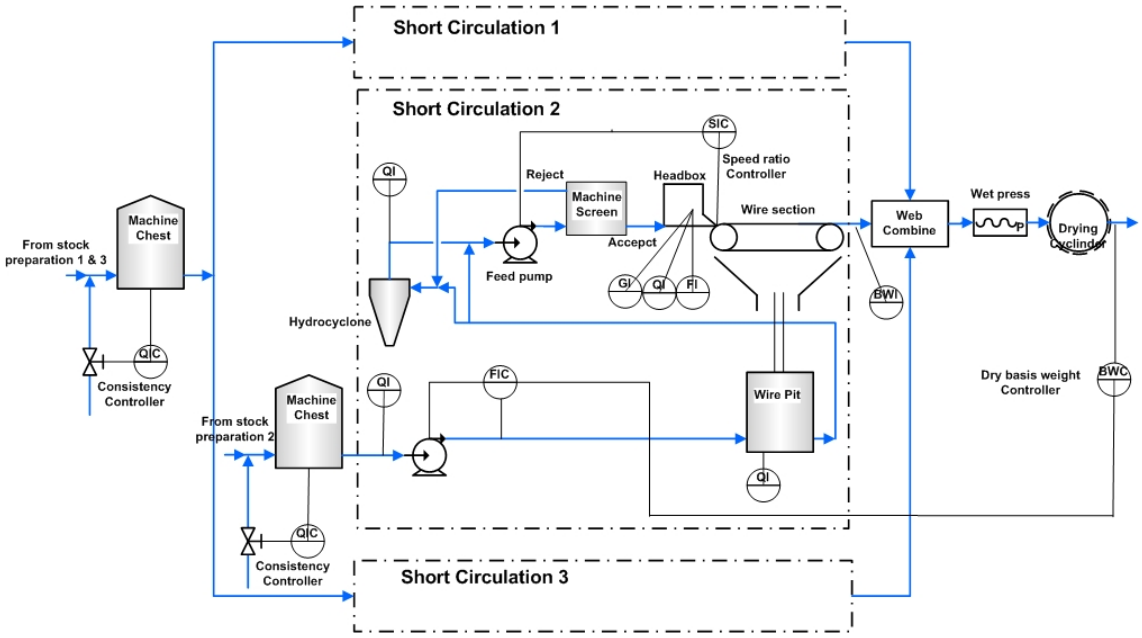

Figure 31. Short circulations of the three-layered board machine (Stora Enso Oyj, 2002).

Formation of the paper or board web begins when the headbox jet hits the wire. The water in the stock starts to drain through the wire and the fibre and other solid material are retained. Kaukopää mills' board machine uses fourdrinier forming for the top and bottom layers. In the fourdrinier process the water is removed only downwards through the horizontal wire. The middle layer also has a top wire unit that enables upward removal of the water. The water that is drained in the forming section, i.e. the white water, is recycled back to the wire pit and is used as dilution water for the thick stock. After the forming, the webs are combined to form the board, which is trimmed to its final width.

In this test, the studied process is limited to the two stock preparation parts, three short circulation parts, three headboxes and three formers. The measurements and actuator signals in these sections of the board machine and the paper quality measurements are listed in Table 9. All of these measurement signals were assumed to be available for fault diagnosis purposes.

Table 9. Description of the variables in the studied board machine.

Variables	Description	Type	Unit
Stock preparation of the layer 1 and 3			
birspeed13	birch pump rotation speed	A[1)]	%
birflow13	mass flow of birch	M[2)]	kg/s
birdval13	dilution water valve opening for the birch line	A	-
birdflow13	dilution water flow for the birch line	E[3)]	kg/s
bircon13	birch consistency	M	%
birpress13	pressure before the birch valve	M	kPa
pspeed13	pine pump rotation speed	A	%
pflow13	mass flow of pine	M	kg/s
pdval13	dilution water valve opening for the pine line	A	-
pdflow13	dilution water flow for the pine line	E	kg/s
pcon13	pine consistency	M	%
ppress13	pressure before the pine valve	M	kPa
mcval13	dilution water valve opening for the machine chest	A	-
dflow13	dilution water flow for the machine chest	E	kg/s
conm13	consistency before the machine chest	M	%
sccon1	consistency of the machine chest	M	%
Stock preparation of the layer 2			
broval2	valve opening for the broke line	A	-
broflow2	mass flow of the broke	M	kg/s
brodval2	dilution water valve opening for the broke line	A	-
brodflow2	dilution water flow for the broke line	E	kg/s
brocon2	broke consistency	M	%
pspeed2	pine pump rotation speed	A	%
pflow2	mass flow of the pine stock	M	kg/s
pdval2	dilution water valve opening for the pine line	A	-
pdflow2	dilution water flow for the pine line	E	kg/s
pcon2	pine consistency	M	%
cspeed2	CTMP pump rotation speed	A	%
cflow2	mass flow of the CTMP	M	kg/s
cdval2	dilution water valve opening for the CTMP line	A	-
cdflow2	dilution water flow for the CTMP line	E	kg/s
ccon2	CTMP consistency	M	%
mcval2	dilution water valve opening for the machine chest	A	-
dflow2	dilution water flow for the machine chest	E	kg/s
conm2	consistency before the machine chest	M	%
ppress2	pressure before the pine valve	M	kg/s
cpress2	pressure before the CTMP valve	M	kg/s
sccon2	consistency of the machine chest	M	%
Short circulation of the layer 1			
bwspeed1	basis weight pump rotation speed	A	%
scflow1	flow from the machine chest (thick stock flow)	M	kg/s
wpcon1	wire pit consistency	M	%

acceptcon1	consistency of accept flow from the hydrocyclone	M	%
headspeed1	headbox feed pump rotation speed	A	%
headflow1	mass flow through the headbox	M	kg/s
headcon1	headbox consistency	M	%
sliceopen1	slice opening of the headbox	A	mm
drybw1	dry basis weight of the layer 1	M	g/m^2
Short circulation of the layer 2			
bwspeed2	basis weight pump rotation speed	A	%
scflow2	flow from the machine chest (thick stock flow)	M	kg/s
wpcon2	wire pit consistency	M	%
acceptcon2	consistency of accept flow from the hydrocyclone	M	%
headspeed2	headbox feed pump rotation speed	A	%
headflow2	mass flow through the headbox	M	kg/s
headcon2	headbox consistency	M	%
sliceopen2	slice opening of the headbox	A	mm
drybw2	dry basis weight of the layer 2	M	g/m^2
Short circulation of the layer 3			
bwspeed3	basis weight pump rotation speed	A	%
scflow3	flow from the machine chest (thick stock flow)	M	kg/s
wpcon3	wire pit consistency	M	%
acceptcon3	consistency of accept flow from the hydrocyclone	M	%
headspeed3	headbox feed pump rotation speed	A	%
headflow3	mass flow through the headbox	M	kg/s
headcon3	headbox consistency	M	%
sliceopen3	slice opening of the headbox	A	mm
drybw3	dry basis weight of the layer 3	M	g/m^2
Process after web merge			
spcon	consistency in the pine pulp storage tank	B[4)]	%
sccon	consistency in the CTMP pulp storage tank	B	%
sbrocon	consistency in the broke pulp storage tank	B	%
scbircon	consistency in the birch pulp storage tank	B	%
conlong	consistency of the dilution water	E	%
drybw123	dry basis weight after the web merge	M	g/m^2
machspeed	machine speed	A	m/min

[1)] 'A' denotes the actuator variable, [2)] 'M' denotes the measurement variable

[3)] 'E' denotes the unmeasurable variables which are estimated from other variables

[4)] 'B' denotes the boundary variables, which is constant

5.1.2 Simulation environment

The Imatra board machine model was developed by Stora Enso and VTT in the APROS environment. It was originally constructed on the base of modelling and simulation studies carried out in 1998-2002 for Stora Enso's Kaukopää mills. It has been

previously used for grade change simulations and studies reported by Lappalainen et al. (2003).

The board machine was modelled from the storage chests of refining to the end of drying section 7. It included the models of the processes and the complete automation system with grade change automation. The modelling and the model itself are presented in Lappalainen (2004). For the sake of simplicity, during the testing the simulator was set up to produce only the two common grades manufactured in the Imatra mill.

The automation system was already included in the simulator. In the test, the variables dry basis weight, dry basis weight ratio between layers, jet wire speed ratio, consistencies in the machine chests, level in the blend chests, consistencies of each pulp line before the blend chests and the flow ratio of different pulps before blending, were controlled to follow the setpoints.

5.2 Dynamic causal digraph modeling

The process knowledge and the fault free data are used in this section to identify the causal structure and the cause-effect relationship models. With the causal structure, the process knowledge about the relationships between the arcs is used to construct the inter-arc knowledge matrix.

5.2.1 Causal digraph construction

Due to the fact that there are similarities between the stock preparations and the short circulations of the individual layers, the stock preparation and short circulation of layer 2 are used to illustrate the causal digraph construction used in this study. After construction of the digraph model for each individual sub-process, the digraph model for the whole process can be formed by connecting the individual sub-processes together.

5.2.1.1 Causal digraph construction for stock preparation of layer 2

The structure of the causal digraph is obtained from the flowsheet of stock preparation 2, together with the process knowledge. The principle is illustrated in Figure 32. It can be clearly seen from the flowsheet that, for the pine line, the total mass flow is mainly affected by three variables: the pump rotation speed *pspeed2*, the dilution water valve opening *pdval2*, and the pressure between the pump and valve *ppress2*. Moreover, the consistency after dilution is determined by the mass flow from the storage chest *pflow2-pdflow2*, the mass flow of the dilution water *pdflow2*, the consistency in the storage chest *spcon* and the consistency of the dilution water *conlong*. However, the consistency in the storage chest is considered to be constant, and the dilution water coming from long circulation can be estimated from the consistencies in the wire pits of the individual layers. Therefore, the consistency in the storage chest and the consistency of the dilution water are considered as parameters instead of the variables in the digraph. Furthermore, the mass flow of the dilution water *pdflow2* can be determined from the dilution water valve opening *pdval2* and the total mass flow in the pine pulp line *pflow2*. This will be explained later in the detailed modelling part. The corresponding causal digraph structure is formed on the basis of the above understanding of the pine pulp line. Since the CTMP line is similar to the pine line in the flowsheet, a digraph structure similar to that shown in Figure 32 is formed. However, the broke line is different from that of the two pulp lines above, because there is no pressure measurement between the pump and the valve, and the total mass flow is controlled by the valve opening. Therefore, a different causal digraph structure is formed for the broke line in Figure 32.

After determination of the digraph structure of each individual pulp lines, the consistency after mixing the dilution water and stock from the blend chest is then considered. It can be seen from the flowsheet that the consistency in the blend chest is affected by the variables mass flow of the pine line, CTMP line, broke line and overflow from the machine chest, consistency of the pine line, CTMP line, broke line and machine chest, and also the dilution water mass flow, which is determined by the

dilution water valve opening. Furthermore, the flow from the blend chest is also regulated by the dilution water valve. The overflow from the machine chest can be calculated by the flows of the individual pulp lines and the flow out of the blend chest according to the mass balance of the blend chest. Thus, the digraph structure for the variable *conm2* is formed as shown in Figure 32. The structure for the consistency in the machine chest is straightforward, because the consistency *conm2* is the only variable that affects the consistency in the machine chest. The arcs in the digraph are numbered and listed in Table 10 in accordance with the causal structure shown in Figure 32.

The board machine model was run in APROS with the control loops closed for the stock preparation of layer 2 in order to collect fault-free data for identification of the models between the variables in the causal digraph shown in Figure 32. During the simulation, the setpoints of the variables *brocon2*, *pcon2*, *ccon2*, *sccon2* were manipulated using different grades, as shown in Figure 33. The sampling time for the data log was 10 seconds.

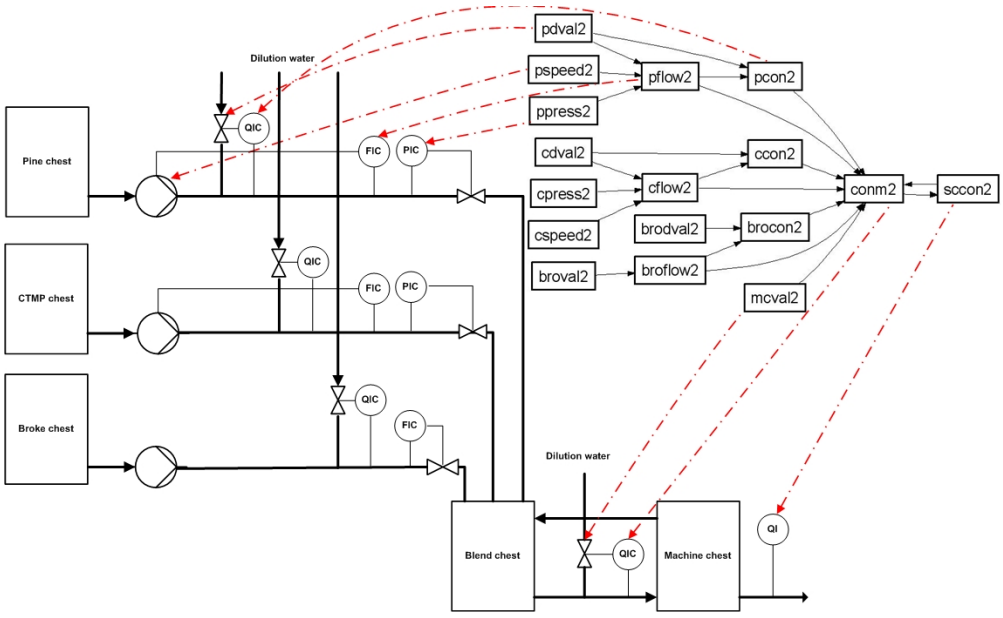

Figure 32. Causal digraph structure of stock preparation 2 derived from the flowsheet.

Table 10. The list of the digraph arcs in Figure 32.

No.	Arcs	No.	Arcs	No.	Arcs
1	*<pdval2, pflow2>*	8	*<cflow2, conm2>*	15	*<broval2, broflow2>*
2	*<pdval2, pcon2>*	9	*<broflow2, brocon2>*	16	*<brodval2, brocon2>*
3	*<cdval2, cflow2>*	10	*<broflow2, conm2>*	17	*<pcon2, conm2>*
4	*<cdval2, ccon2>*	11	*<ppress2, pflow2>*	18	*<ccon2, conm2>*
5	*<pflow2, pcon2>*	12	*<pspeed2, pflow2>*	19	*<brocon2, conm2>*
6	*<pflow2, conm2>*	13	*<cpress2, cflow2>*		
7	*<cflow2, ccon2>*	14	*<cspeed2, cflow2>*		

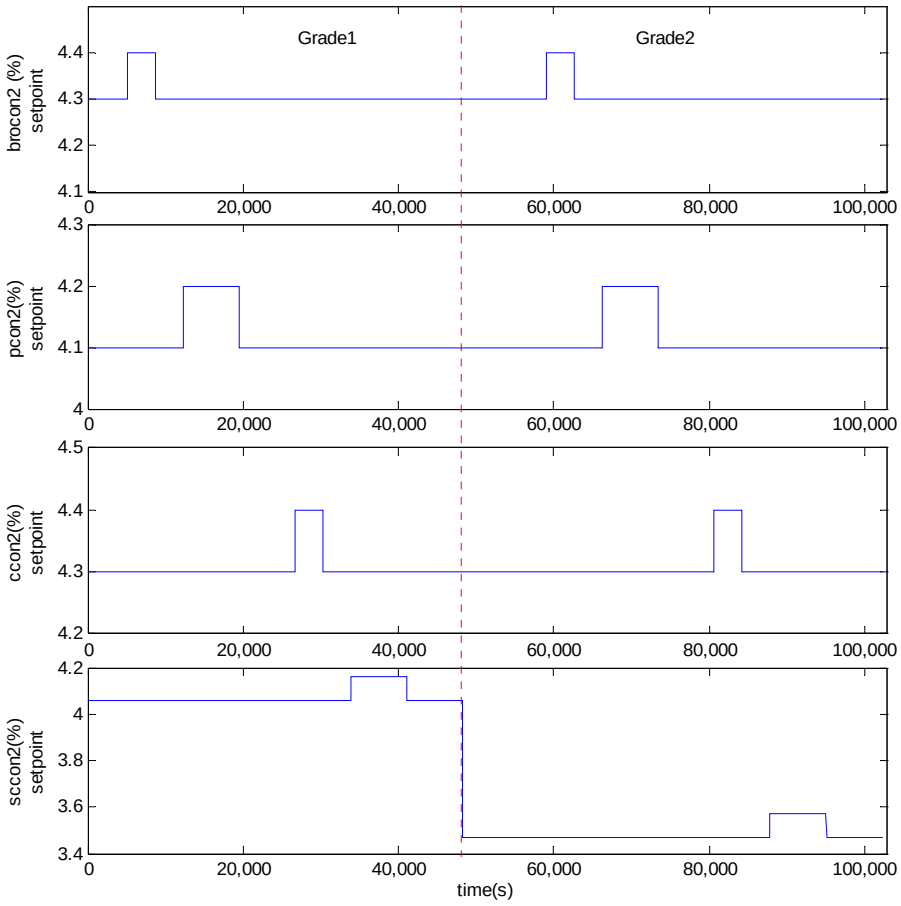

Figure 33. Setpoint manipulations for the stock preparation of layer 2 in fault free simulation.

The cause-effect models between the variables in the digraph were identified on the basis of the fault-free data and are described in detail in the following sections.

The model for the variable *pflow2* is first considered. According to Figure 32, the variable *pflow2* is affected by the variables *pdval2*, *pspeed2* and *ppress2*. Because the dynamics of the mass flow *pflow2* is negligible during the sampling time of 10 s, the static models were used for all the mass flows in this study. The model structure shown in Figure 34 was utilized for the variable *pflow2*. In the model, the second order and the third order terms, $pdval2^2$ and $pdval2^3$ were used also as inputs to the neural network, in order to get better fit. The multiple layer perception (MLP) structure for the neural network is used with one sigmoid hidden node and one linear output node. The parameters for the neural network are given in Appendix A.

The model output for the variable *pflow2* together with the measurement, and the model error are shown in Figure 35. The mean square error (MSE) of the model error is given in Table 11. The results validate that the selection of the model type and the identified parameters are proper.

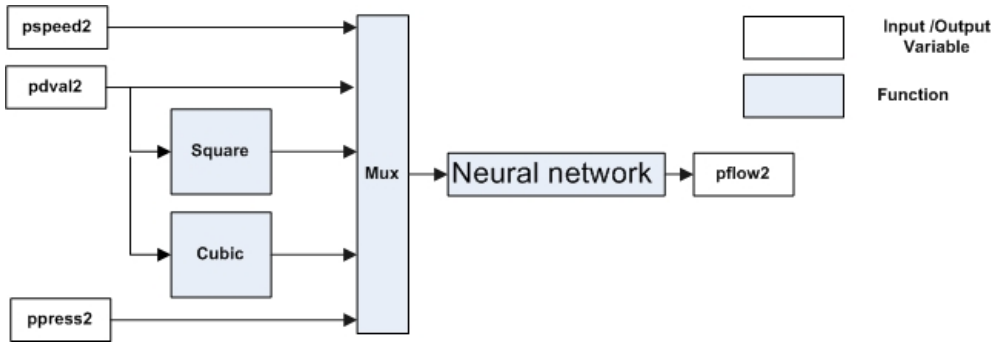

Figure 34. Model structure for the variable *pflow2*.

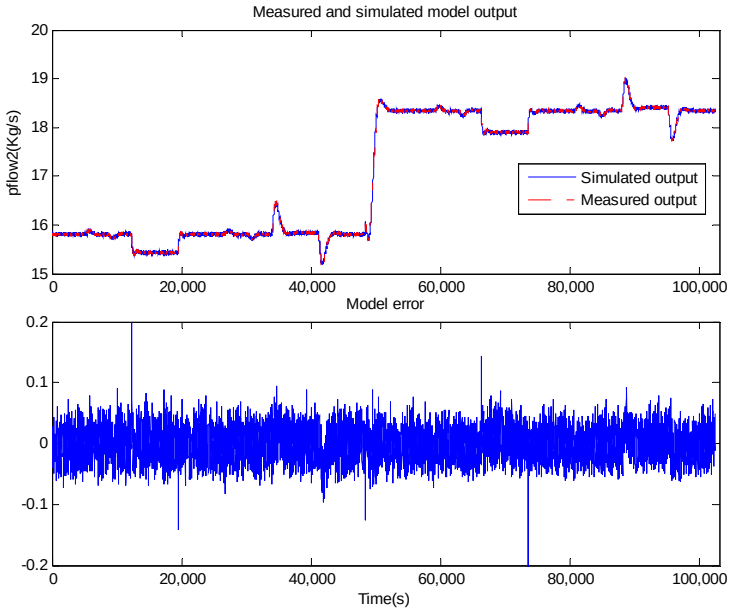

Figure 35. Measured and simulated value for the variable *pflow2* and the model error.

The model for the variable *pcon2* is considered next. It is obvious from the flowsheet in Figure 32 that the variable *pcon2* is directly determined by the following variables: consistency in the pine storage tank *spcon*, consistency of the dilution water *conlong*, mass flow of the dilution water *pdflow2*, and the mass flow from the pine storage tank *pflow2-pdflow2*. As the consistency in the storage tank is considered to be the boundary condition for the simulation, it therefore has a constant value of 4.5% and is taken as a parameter in the model. The consistency of the dilution water is changing during the simulation because it is affected by the consistencies of the three wipe pits in the short circulations. However, the value of *conlong* is around 0.02%, which is very small compared with the consistency in storage tank (4.5%). Moreover, the long short circulation of the dilution water has been excluded from the study. Therefore, the consistency of the dilution water is taken as a parameter in the model instead of an input variable, and estimated as follows.

$$conlong = \frac{wpcon1 + wpcon2 + wpcon3}{3} \tag{5.1}$$

Thus, if the variable *pdflow2* can be calculated from the variables *pdval2* and *pflow2*, then the physical mixing model can be used to calculate the variable *pcon2*. The structure of the model is shown in Figure 36, where MLP is used for the variable *pdflow2*. Due to the fact that *pdflow2* is not measurable, it is estimated for the neural network training from the variables *pon2*, *pflow2*, and *spcon* according to the physical mixing model. The parameters for the neural networks are given in Appendix A.

The model output for the variable *pcon2* together with the measurement, and the model error are shown in Figure 37. The MSE of the model error is given in Table 11. The results demonstrate that the selection of the model type and the identified parameters are correct.

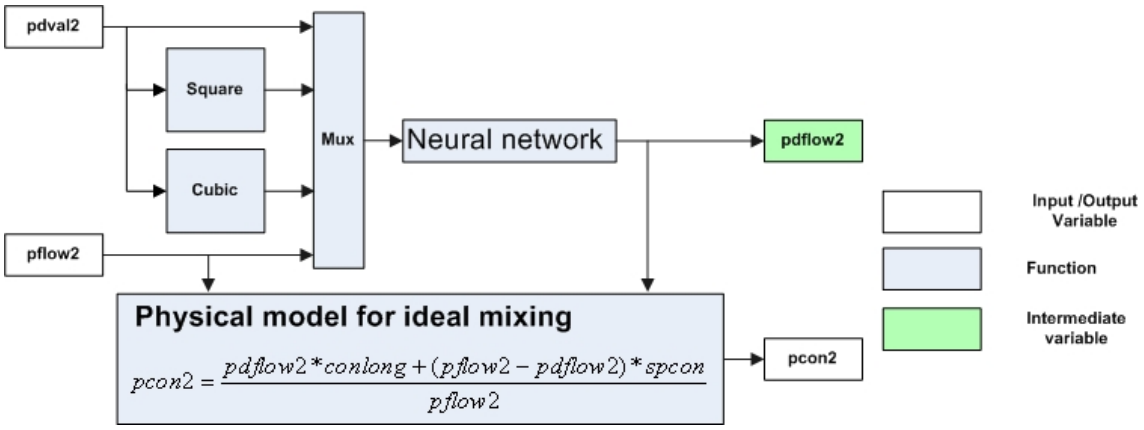

Figure 36. Model structure for the variable *pcon2*.

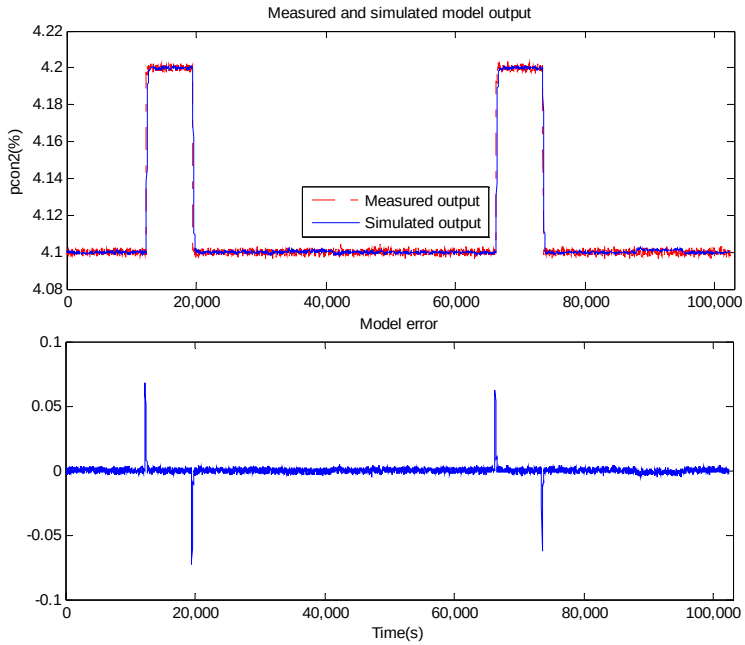

Figure 37. Measured and simulated value for the variable *pcon2* and the model error.

The model for the variable *conm2* is considered next. The models for the variables *cflow2*, *broflow2*, *ccon2* and *brocon2* have similar structures to those of the variables *pflow2* and *pcon2*. The parameters of these models are summarized in Appendix A.

It can be seen from the flowsheet in Figure 32 that *conm2*, the consistency after the mixing of the flow from the blend chest and the dilution water, is determined by the variables *blecon2*, *bleflow2*, *dflow2* and *conlong*. For the same reason, *conlong* in the model for *pcon2* is also considered as a parameter here and estimated using Equation 5.1. The variables *bleflow2* and *dflow2* can be calculated from the dilution water valve opening *mcval2*, because the level of the blend chest is controlled to follow the constant setpoint. Thus, if *blecon2* can be calculated, then the physical mixing model can be used to calculate the variable *conm2*. With the assumption that the level of the blend chest is constant and that mixing in the tank is ideal, the physical tank model can be used to calculate *blecon2* on the basis of the material balance. The physical tank model for the blend chest is:

$$\frac{d(M_b * blecon2)}{dt} = pflow2 * pcon2 + cflow2 * ccon2$$
$$+ broflow2 * brocon2 + f_o * sccon2 - bleflow2 * blecon2 \quad (5.2)$$
$$f_o = bleflow2 - pflow2 - cflow2 - broflow2$$

where M_b is the mass of the pulp in the blend chest ,which is taken as constant, and f_o is the overflow from the machine chest. Because the measurements from the simulator were sampled at 10 s intervals, the differential equation in Equation 5.2 can be discretized as

$$\frac{blecon2(k+1) - blecon2(k)}{\Delta t} * M_b = pflow2(k) * pcon2(k)$$
$$+ cflow2(k) * ccon2(k) + broflow2(k) * brocon2(k) \quad (5.3)$$
$$+ f_o(k) * sccon2(k) - bleflow2(k) * blecon2(k)$$

With further manipulation, the model for *blecon2* is

$$blecon2(k+1) = blecon2(k) + \frac{\Delta t}{M_b} * (pflow2(k) * pcon2(k) + cflow2(k) * ccon2(k) \quad (5.4)$$
$$+ broflow2(k) * brocon2(k) + f_o(k) * sccon2(k) - bleflow2(k) * blecon2(k))$$

where Δt is the sampling time of 10 s. M_b can be calculated from the parameters of the blend chest as $M_b = \rho_s * V_b = 1000 * 86.1 = 86100\,kg$, where ρ_s is the density of the stock (here taken as 1000 kg/m^3), and V_b is the volume of the blend chest (given as 86.1 m^3). The model structure for the variables *conm2* is shown in Figure 38.

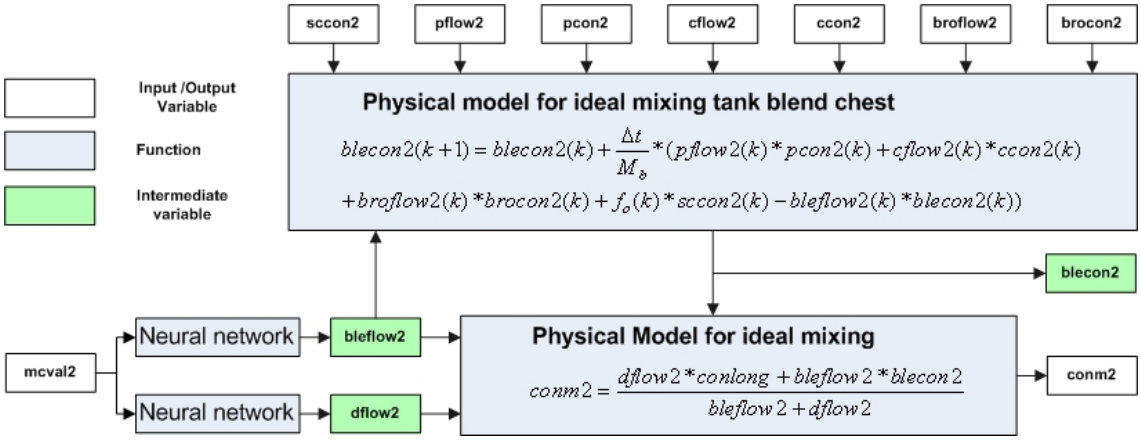

Figure 38. Model structure for the variable *conm2*.

Due to the fact that the intermediate variables *blecon2*, *bleflow2*, and *dflow2* are not measurable in the process, the variable *dflow2* is first estimated according to the material balance as $dflow2 = scflow2 - tf2$, which is used for the neural network training. MLP is also used for the variable *bleflow2*. However, the MLP is trained by minimizing the prediction error of the *conm2* model. Finally, the variable *blecon2* is not estimated, because there is no parameter to be identified in the physical model of the blend chest in Equation 5.4.

The model output for the variable *conm2* together with the measurement, and the model error are shown in Figure 39. The MSE of the model error is given in Table 11. The results validate the model type and the identified parameters

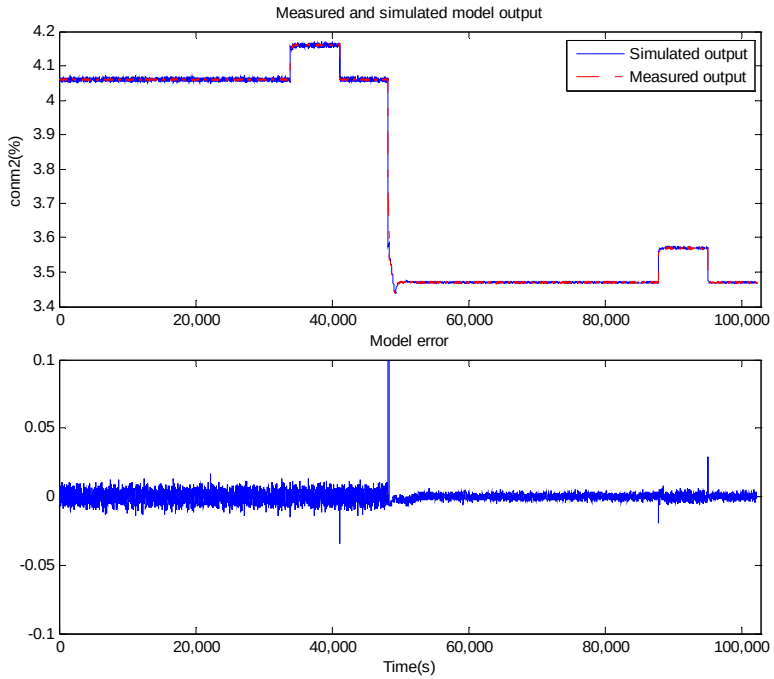

Figure 39. Measured and simulated value for the variable *conm2* and the model error.

The model for the variable *sccon2* is considered in the following. It can be seen from Figure 32 that the machine chest is located between the variables *conm2* and *sccon2*. According to the tank material balance, we have the following equations

$$\frac{d(M_m * sccon2)}{dt} = conm2 * mcflow2 - f_o * sccon2 - scflow2 * sccon2$$
$$mcflow2 = f_o + scflow2 \qquad (5.5)$$

where M_m is the mass of the pulp in the machine chest, and *mcflow2* is the mass flow to the machine chest. Since the machine chest has continuous overflow and the centrifugal pump between the blend chest and the machine chest has a constant rotation speed, M_m and *mcflow2* can be assumed to be constant. Thus, the transfer function between *conm2* and *sccon2* in the Laplace domain and in the Z domain can be derived from Equation 5.5 as

$$\frac{sccon2(s)}{conm2(s)} = \frac{\frac{mcflow2}{M_m}}{s + \frac{mcflow2}{M_m}} \quad \text{and} \quad \frac{sccon2(z)}{conm2(z)} = \frac{(1 - \exp(-1 * \frac{mcflow2}{M_m} * \Delta t))z}{z - \exp(-1 * \frac{mcflow2}{M_m} * \Delta t)} \tag{5.6}$$

As can be seen from Equation 5.6, this model always has a steady gain of 1, which implies that, in the steady state, *sccon2* and *conm2* are the same. In the discrete model, $\exp(-1 * \frac{mcflow2}{M_m} * \Delta t)$ was identified as a parameter and is shown in Appendix A.

The model output for the variable *sccon2* together with the measurement, and the model error are shown in Figure 40. The MSE of the model error is given in Table 11. The results validate the model type and the identified parameters.

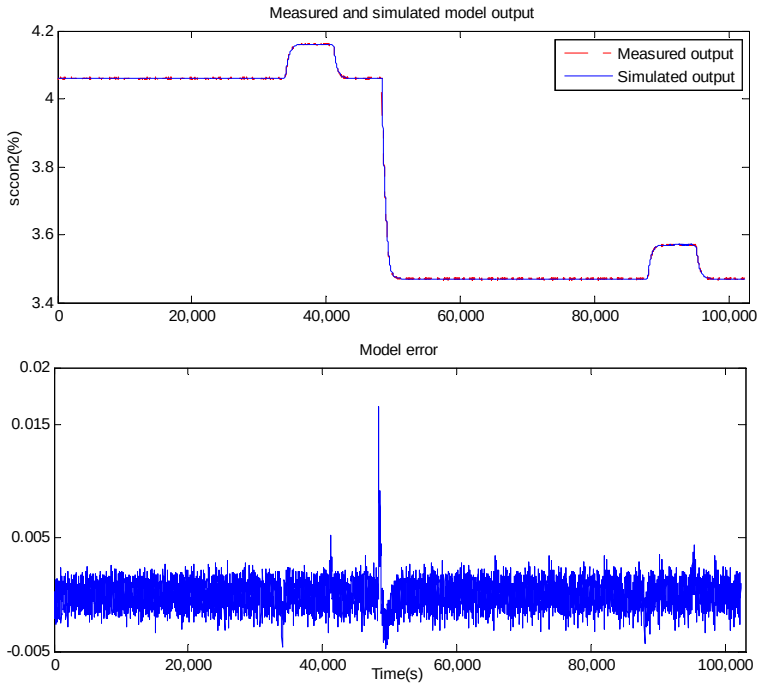

Figure 40. Measured and simulated value for the variable *sccon2* and the model error.

The causal digraph model, including the structure and the cause-effect models for the stock preparation of layer 2 have been formed in order to illustrate the principles applied in modelling the stock preparation process. The values of the mean square error (MSE) for the models *pflow2*, *pcon2*, *conm2*, *sccon2* with modelling data, are listed in the following table. Moreover, the models are also validated by the data from the experiments for stock preparations and short circulations. The values of MES for the model validation are also listed in the following table.

Table 11 MSE for the models *pflow2*, *pcon2*, *conm2*, *sccon2*

Model		*pflow2*	*pcon2*	*conm2*	*sccon2*
MSE	Data from stock preparation 2	$6.89*10^{-4}$	$1.29*10^{-6}$	$1.45*10^{-5}$	$1.43*10^{-6}$
	Data from stock preparation 1 & 3	$6.24*10^{-4}$	$1.69*10^{-6}$	$1.27*10^{-5}$	$2.35*10^{-6}$
	Data from short circulation 1	$6.57*10^{-4}$	$1.76*10^{-6}$	$1.49*10^{-5}$	$2.85*10^{-6}$
	Data from short circulation 2	$7.20*10^{-4}$	$1.78*10^{-6}$	$1.42*10^{-5}$	$2.26*10^{-6}$
	Data from short circulation 3	$6.50*10^{-4}$	$1.80*10^{-6}$	$1.48*10^{-5}$	$2.80*10^{-6}$

Due to the similarity between the stock preparations of the different layers, the procedure used in modelling the stock preparation of layers 1 and 3 is not considered here. The structure of the causal digraph of layers 1 and 3 is shown in Figure 51, while the parameters of the cause-effect models are shown in Appendix A.

5.2.1.2 Causal digraph construction for the short circulation of the layer 2

The structure of the causal digraph is first obtained from the flowsheet of the short circulation of layer 2 together with the process knowledge. The principle is illustrated in Figure 41. It can be seen clearly from the flowsheet that the thick stock flow rate *scflow2* is affected by the basis weight pump rotation speed *bwspeed2*, and that the mass flow through the headbox *headflow22* is affected by the slice opening of the head box *sliceopen2* and the rotation speed of the headbox feed pump *headspeed2*. It also can be seen from the flowsheet that the consistency of the accept stock in the hydrocyclone *acceptcon2* is affected by the thick stock flow *scflow2*, thick stock consistency *sccon2*, and the consistency in the wire pit *wpcon2*, because the thick stock is diluted by the wire pit water before it passes to the hydrocyclone. The variables *acceptcon2* and *headflow2* have an effect on the consistency in the headbox *headcon2*, because the

accept stock of the hydrocyclone is diluted again by the wire pit water, the mass flow rate of which can be determined by the variable *headflow22*. The structure for the variables *wpcon2* and *drybw2* can be easily obtained from the flowsheet. The reason why the variable *headflow22* has an effect on the variables *scflow2*, *acceptcon2* is explained later on in connection with the detailed modelling with fault-free simulation data. The arcs in the digraph are numbered and listed in Table 12 in accordance with the obtained causal structure.

The board machine model in APROS was run with the control loops closed for the short circulation of layer 2 in order to collect fault-free data for identification of the cause-effect models between the variables in the causal digraph shown in Figure 41. During the simulation, the setpoints of the variables *drybw123*, *sccon2*, *sliceopen2*, *jwratio2*, were manipulated in two different grades (see Figure 42). The sampling time for the data logging was 10 seconds.

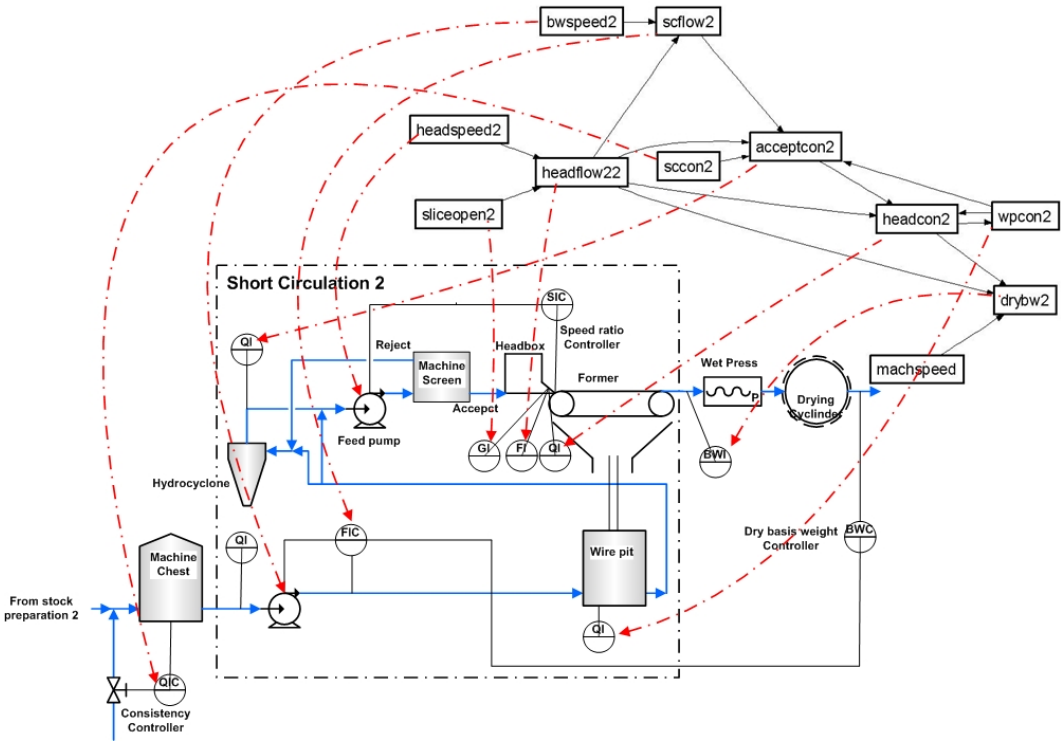

Figure 41. Causal digraph structure of short circulation 2 derived from the process flowsheet.

Table 12. The list of the digraph arcs in Figure 41.

No.	Arcs	No.	Arcs
1	<*headspeed2*, *headflow22*>	8	<*headflow22*, *acceptcon2*>
2	<*sliceopen2*, *headflow22*>	9	<*headflow22*, *headcon2*>
3	<*bwspeed2*, *scflow2*>	10	<*headflow22*, *drybw2*>
4	<*sccon2*, *acceptcon2*>	11	<*headcon2*, *wpcon2*>
5	<*scflow2*, *acceptcon2*>	12	<*headcon2*, *drybw2*>
6	<*acceptcon2*, *headcon2*>	13	<*wpcon2*, *acceptcon2*>
7	<*headflow22*, *scflow2*>	14	<*wpcon2*, *headcon2*>

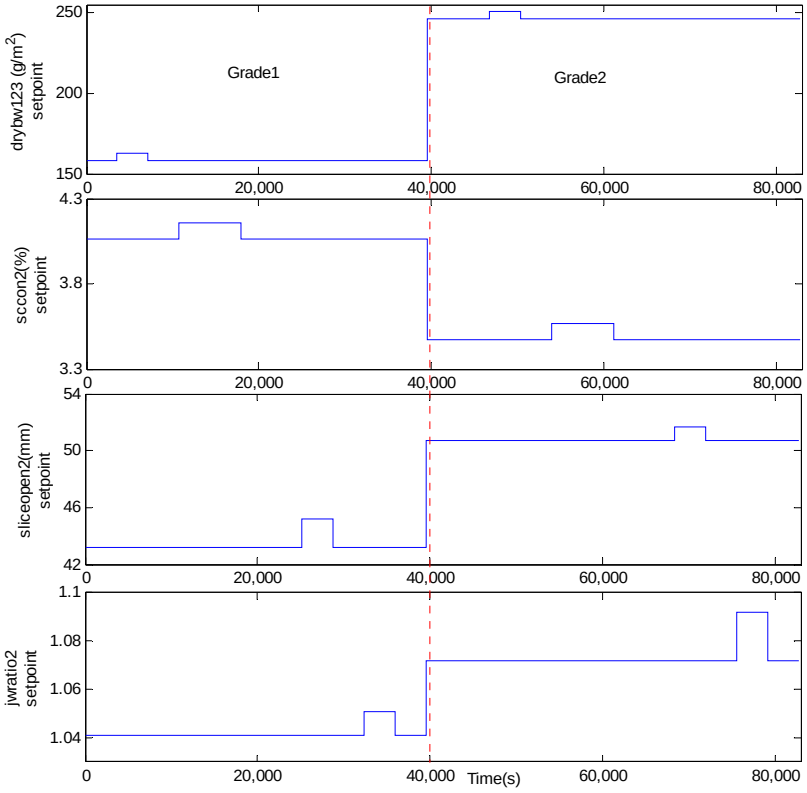

Figure 42. Setpoint manipulations for short circulation of the layer 2 in the fault-free simulation.

The cause-effect models between the variables in the digraph were identified using the fault-free data, and they are described in detail in the following sections.

The model for the variable *headflow2* is considered first. It is clear from the flowsheet presented in Figure 41 that the headbox mass flow is regulated by the variables *sliceopen2* and *headspeed2*. A simple static linear regression model was applied to describe the cause-effect relationship. The parameters of the model are given in Appendix A.

The model output for the variable *headflow22* together with the measurement, and the model error are shown in Figure 43. The MSE of the model error is given in Table 13. The results validate the model type and the identified parameters.

The model for the variable *scflow2* is considered next. The flowsheet presented in Figure 41 shows that the variable *scflow2* is affected by the basis weight pump rotation speed *bespeed2*. However, the fault-free simulation implies that the variable *headflow22* has an effect on the variable *scflow2*, as shown in Figure 44. It can be seen from Figure 44 that the thick stock flow remained constant during the period 25 200-28 800 s and the period 32 400-36 000 s, while the dry basis weight pump rotation speed decreased significantly. The main reason for this phenomenon is that the headbox mass flow *headflow22* increased during these two periods (see Figure 43) which, in turn, decreased the pressure in the accept outlet of the hydrocyclone and the output of the basis weight pump. The decreased pressure thus makes it possible to have the same thick stock flow with a lower rotation speed of the basis weight pump. For this reason, the variable *headflow22* is selected as another input for the variable *scflow2*.

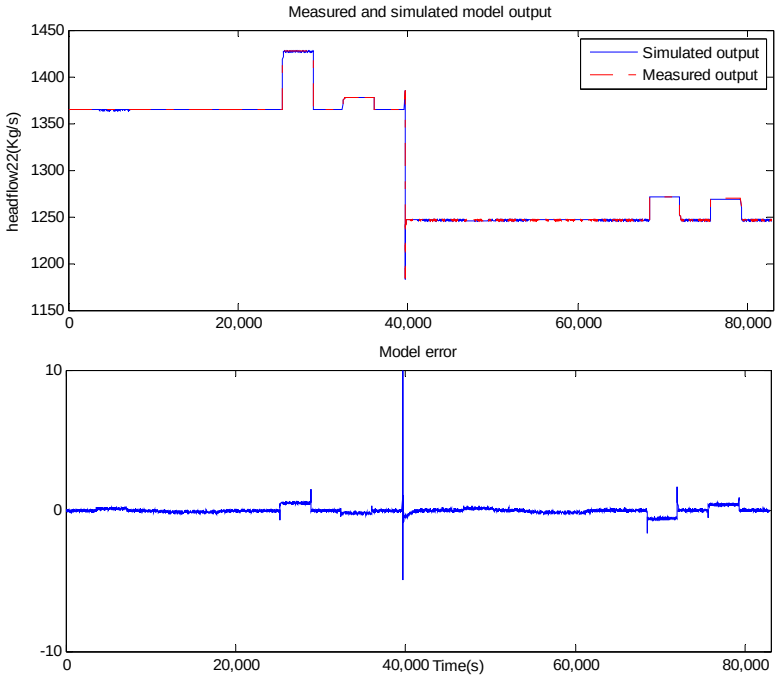

Figure 43. Measured and simulated value for the variable *headflow22* and the model error.

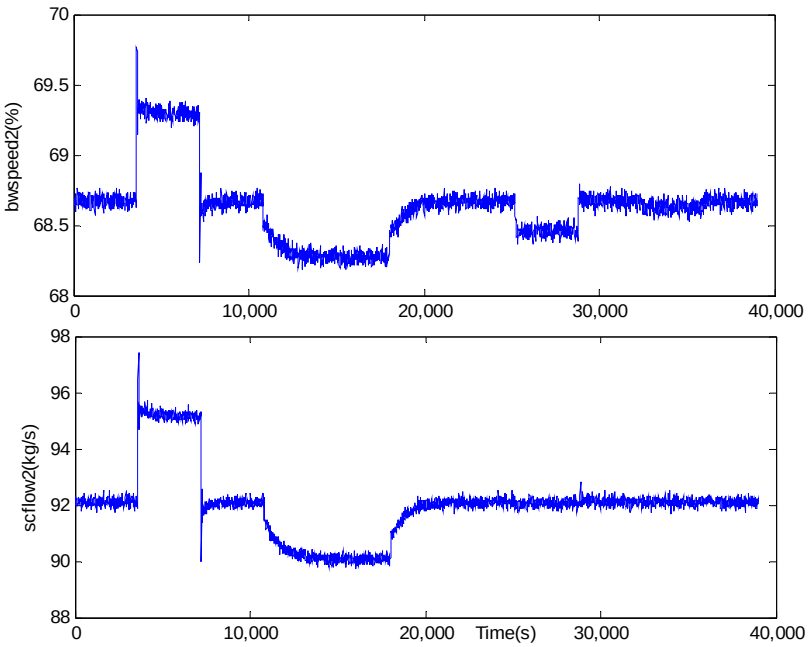

Figure 44. Variables *bwspeed2* and *scflow2* during the period of grade 1.

A simple static linear regression model structure is used. In order to get better fit of the model, the second order term *bwspeed2*^{2} is introduced as an extra input, while the square root of the variable *headflow22* is used instead of itself.

The model output for the variable *scflow22* together with the measurement, and the model error are shown in Figure 45. The MSE of the model error is given in Table 13. The results validate the model type and the identified parameters.

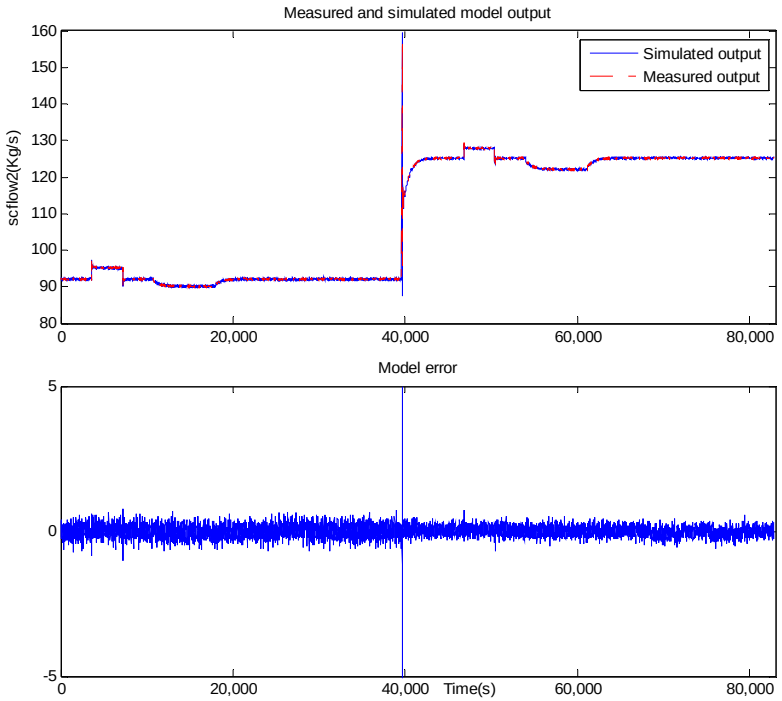

Figure 45. Measured and simulated value for the variable *scflow22* and the model error.

The model for the variable *acceptcon2* is considered next. The basic principle of the hydrocyclone operation is the mass flow and solid content splitters. The thick stock is diluted by the wire pit water before passing to the hydrocyclone. The diluted stock is split on the basis of the pressure differences between the inlet of the hydrocyclone and its two outlets: accept and reject. The solid content in the stock is split mainly on the basis of the density. Thus it is relatively natural to select the variables *scflow2*, *sccon2*,

wpcon2 as parent variables for *acceptcon2*. However, Figure 46 shows that the headbox flow *headflow22* also has an effect on the variable *acceptcon2*. Figure 44 and Figure 46 show that the variables *scflow2* and *sccon2* remained unchanged during the period 25 200-28 800 s and the period 32 400-36 000 s, while *acceptcon2* decreased. The flowsheet presented in Figure 41 shows that the headbox flow *headflow22* affects the variable *acceptcon2* in two ways. Firstly, when *headflow22* increases, then the pressure of the accept outlet of the hydrocyclone decreases, which leads to an increase in the mass flow of the dilution water from the wire pit, while the thick stock flow and consistency remain unchanged. This effect will lead to a decrease in the variable *acceptcon2*. Secondly, the increase in *headflow22* leads to an increase in the dilution water mass flow before the machine screen which, in turn, results in a decrease in the consistency of the stock feed back from the machine screen to the hydrocyclone. This effect will also cause a decrease in the variable *acceptcon2*. Therefore, the variable *headflow22* is selected as a parent variable for the variable *acceptcon2*.

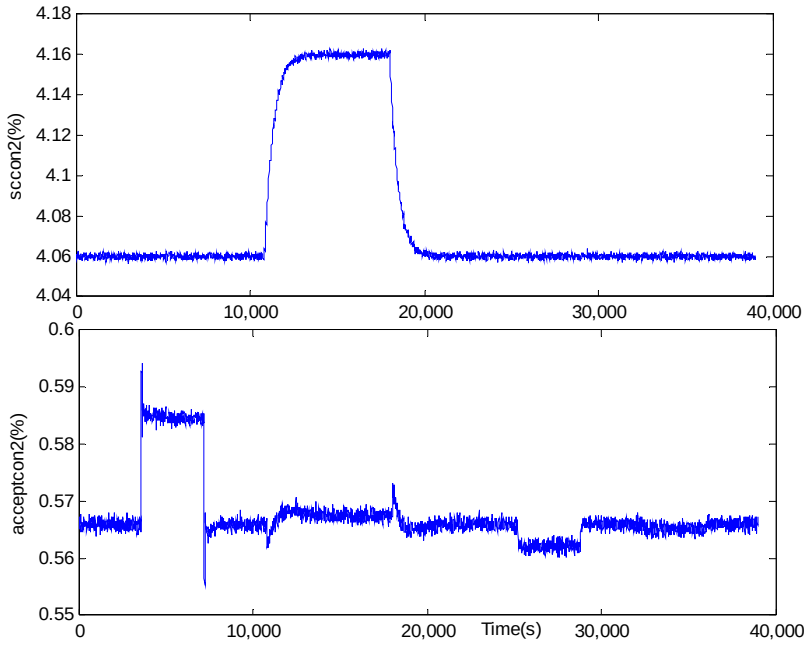

Figure 46. Variables *sccon2* and *acceptcon2* during the period of grade 1.

A simple, static linear regression model structure was used. The term *sccon2*scfow2* is introduced to depict the mixing process between the thick stock and the wire pit water. Moreover, the square root of the variable *headflow22* was used instead of itself in order to obtain better fit. The parameters are shown in Appendix A.

The model output for the variable *acceptcon2* together with the measurement, and the model error are shown in Figure 47. The MSE of the model error is given in Table 13. The results validate the model type and the identified parameters.

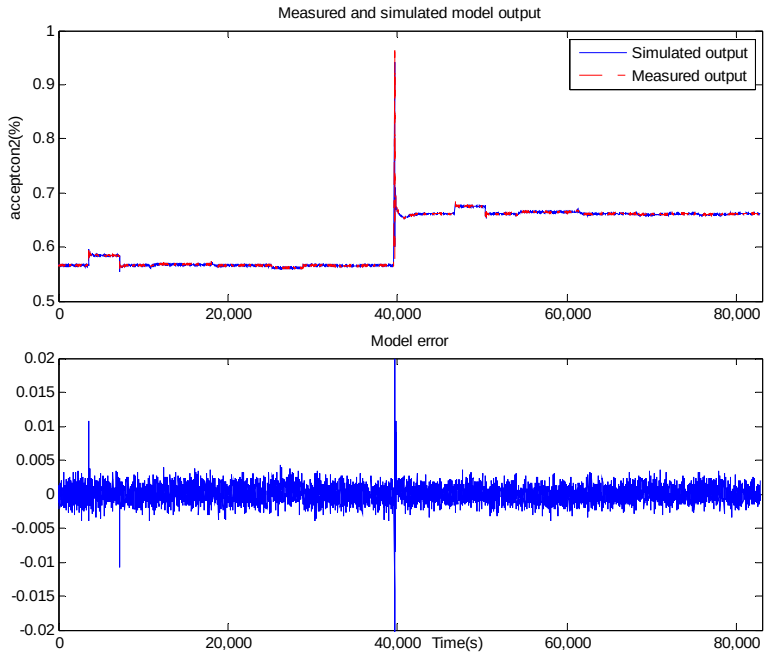

Figure 47. Measured and simulated value for the variable *acceptcon2* and the model error.

The model for the variable *headcon2* is considered in the following. The flowsheet presented in Figure 41 shows that the accept stock of the hydrocyclone is again diluted with the wire pit water before the headbox feed pump. In the machine screen the mass flow is split according to the pressure differences between the inlet and the two outlets. The solid content is mainly split on the basis of the particle size. Thus, the process

between the hydrocyclone and the headbox can be considered as a mixing process, except that part of the solid content does not reach the headbox because of the machine screen. Assuming the dilution water flow is affected by *headflow22*, and that the accept mass flow of the hydrocyclone is constant because the feed pump of the hydrocyclone is rotating at constant speed, then *headcon2* can be calculated as

$$\begin{aligned} headcon2 &= \frac{f_{ac} * acceptcon2 + f_{wp} * wpcon2}{headflow22} \\ f_{wp} &= \theta_1 * \sqrt{headflow22} + \theta_2 * headflow22 + \theta_3 \end{aligned} \tag{5.7}$$

where f_{ac} and f_{wp} are the mass flow from the hydrocyclone and the wire pit, respectively, and θ_1, θ_2, and θ_3 are the linear regression parameters. The equation can be further modified to

$$headcon2 = f_{ac} * \frac{acceptcon2}{headflow22} + \theta_1 * \frac{wpcon2}{\sqrt{headflow22}} + \theta_2 * wpcon2 + \theta_3 * \frac{wpcon2}{headflow22} \tag{5.8}$$

The structure of the static linear regression model is based on Equation 5.8. The parameters are identified using the least squares method, and thay are shown in Appendix A.

The model output for the variable *headcon2* together with the measurement, and the model error are shown in Figure 48. The MSE of the model error is given in Table 13. The results validate the model type and the identified parameters.

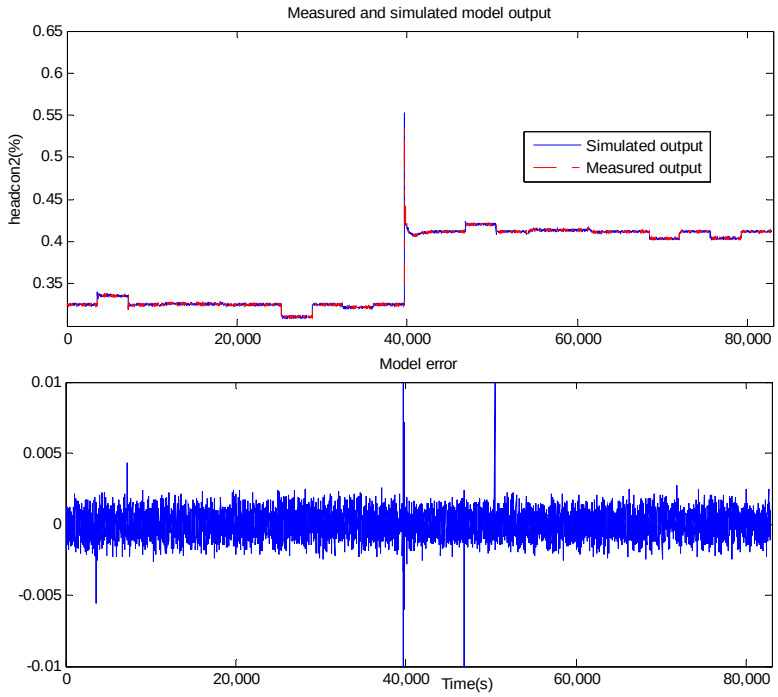

Figure 48. Measured and simulated value for the variable *headcon2* and the model error.

The model *wpcon2* is considered next. The flowsheet presented in Figure 41 shows that the water is drained after the stock is sprayed onto the wire. At the same time, part of the solid material passes through the wire section and is collected by the wire pit. The consistency of the white water under the wire *wwcon2* is calculated as

$$wwcon2 = \frac{headcon2 * headflow22 * \alpha}{headcon2 * headflow22 * \alpha + (100 - headcon2) * headflow22 * \beta} = \frac{headcon2 * \alpha}{headcon2 * \alpha + (100 - headcon2) * \beta} \quad (5.9)$$

where α is the percentage of the solid content that passes through the wire, and β is the percentage of water that passes through the wire. Typical values for α and β are 10% and 95%, respectively. Considering the fact that the headbox consistency *headcon2* is around 0.3% and is much smaller than 100, Equation 5.9 can be simplified as

$$wwcon2 = \frac{\alpha}{\alpha + (\frac{100}{headcon2} - 1) * \beta} \approx \frac{\alpha}{100 * \beta} * headcon2 \qquad (5.10)$$

Equation 5.10 implies that the gain from the variable *headcon2* to *wpcon2* is almost constant. It is also relatively common for the volume of the wire pit to be relatively large compared with the white water mass flow or the headbox mass flow *headflow22*, and this results in a large time constant for the first order tank model. Thus, it is possible to use a first order discrete model to describe the cause-effect relationship between the variables *headcon2* and *wpcon2*.

The model output for the variable *wpcon2* together with the measurement, and the model error are shown in Figure 49. The MSE of the model error is given in Table 13. The results validate the model type and the identified parameters.

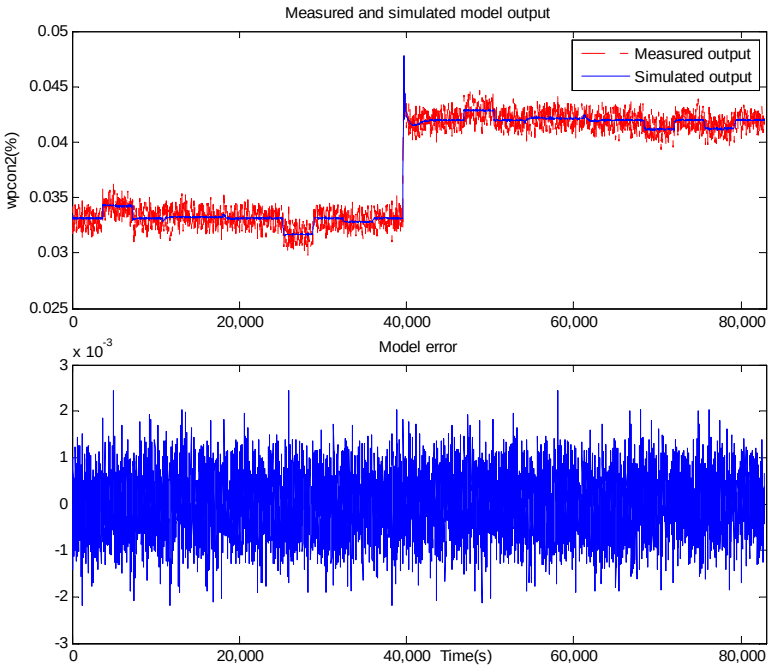

Figure 49. Measured and simulated value for the variable *wpcon2* and the model error.

The models for the variables *drybw2* and *drybw123* are considered next. It can be seen clearly from the flowsheet presented in Figure 41 that the dry basis weight of layer 2 is related to the variables *headflow22*, *headcon2* and *machspeed* according to the formula

$$drybw2 = \frac{headflow22 * headcon2 * 1000}{machspeed * w2} * \eta \tag{5.11}$$

where $w2$ is the width of the web, and η is the retention rate. The number 1000 comes from the fact that *headflow22* has the unit kg/m and the variable *drybw2* has the unit g/m^2. For layer 2, the web width is 6.2 meter and the retention rate η is determined from the modelling data. Therefore the total dry basis weight of the three-layered board after the web merge is calculated from the variables *drybw1*, *drybw2*, and *drybw3* as

$$drybw123 = (drybw1 + drybw2 + drybw3) * \delta \tag{5.12}$$

where δ is the retention rate during the web combine, and is determined from the modelling data.

The model output for the variable *drybw123* together with the measurement, and the model error are shown in Figure 50. The MSE of the model error is given in Table 13. The results validate the model type and the identified parameters.

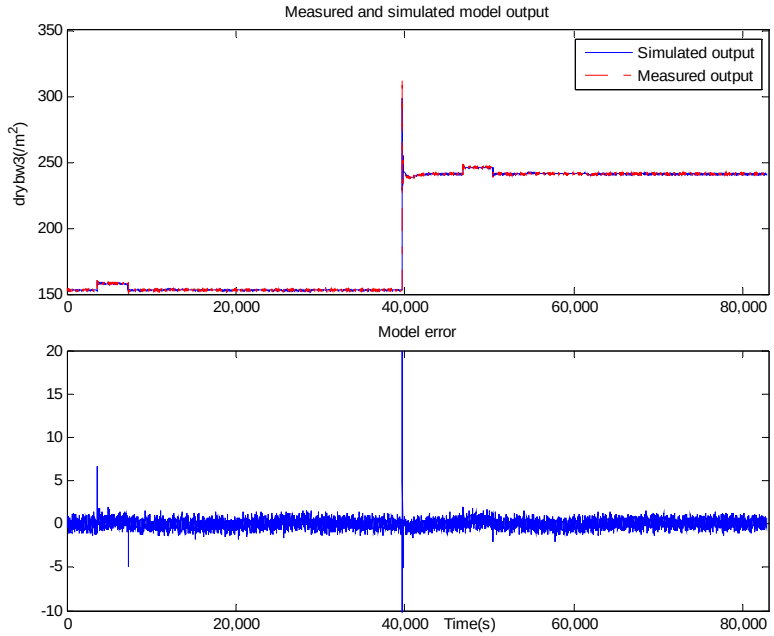

Figure 50. Measured and simulated value for the variable *drybw123* and the model error.

So far, the causal digraph model, which includes the structure and the cause-effect models for the short circulation of layer 2, have been formed to illustrate the principles utilized in modelling the short circulation process. The values of the mean square error (MSE) for the models *headflow22*, *scflow2*, *acceptcon2*, *headcon2*, *wpcon2*, *drybw123*, are listed in the following table.

Table 13. MSE for the models *headflow22*, *scflow2*, *acceptcon2*, *headcon2*, *wpcon2*, *drybw123*.

Model	*headflow22*	*scflow2*	*acceptcon2*	*headcon2*	*wpcon2*	*drybw123*
MSE	0.179	0.144	$5.31*10^{-6}$	$1.87*10^{-6}$	$4.12*10^{-7}$	2.76

Due to the similarity between the short circulations of the different layers, the procedure used in modelling the short circulation of both layers 1 and 3 is considered here. The overall causal digraph model, obtained by combining the stock preparation digraph models and the short circulation models, is presented in Figure 51. The cause-effect models between the variables are given in Appendix A.

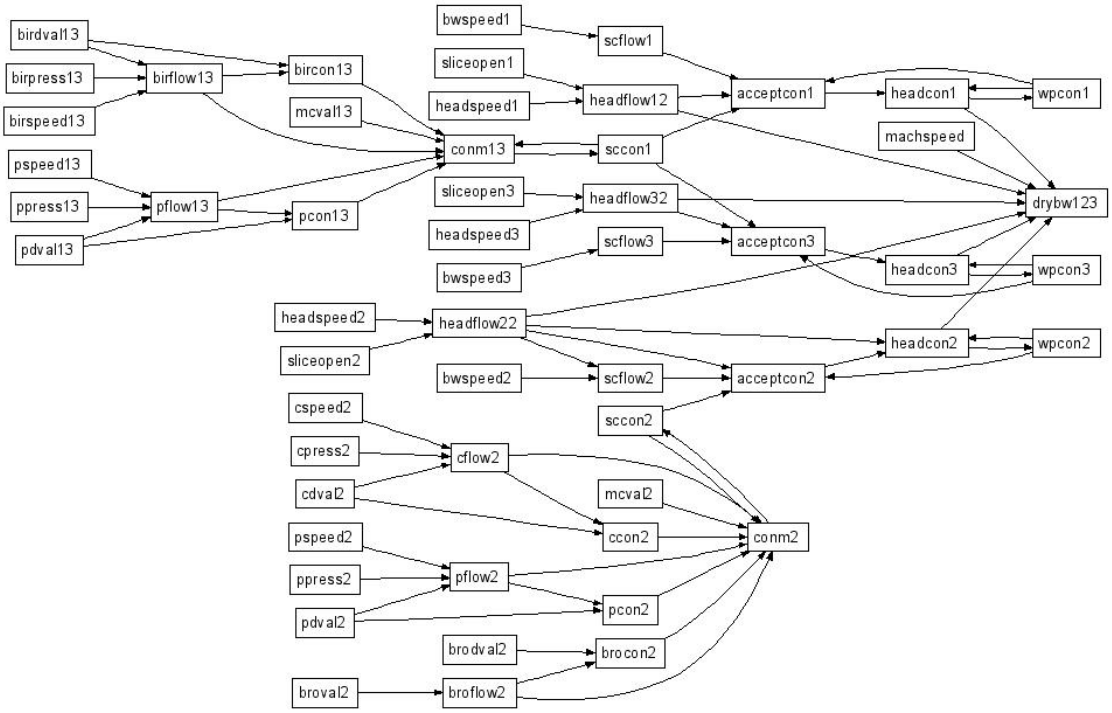

Figure 51. The causal digraph structure for the two stock preparations and the three short circulations of the board machine.

5.2.2 Construction of the inter-arc knowledge matrix

In order to perform the inference between the arcs, the inter-arc knowledge matrix first needs to be formed according to Equations 3.9, 3.10 and 3.11, and using the process knowledge presented in Section 5.1. For the sake of the simplicity, only the inter-arc knowledge matrices for the stock preparation of layer 2 and the short circulation of layer 2 are shown here.

5.2.2.1 Inter-arc knowledge matrix for the stock preparation of layer 2

In the causal digraph model for the stock preparation of layer 2 shown in Figure 32, the knowledge matrices of the nodes with output arcs were first formed on the basis of the process knowledge.

The knowledge matrix $\mathbf{M}_{pdval2} = \begin{bmatrix} 1 & 1 \\ 0 & 1 \end{bmatrix}$ was formed for the node *pdval2*. It represents the relationship between the arc <*pdval2*, *pflow2*> and <*pdval2*, *pcon2*>. It can be seen from matrix $\mathbf{M}_{pdval2}$ that the inconsistency of the arc <*pdval2*, *pcon2*> does not always result in an inconsistency in another output arc, while the inconsistency of the arc <*pdval2*, *pflow2*> always results in an inconsistency in arc <*pdval2*, *pcon2*>. The reason for this is that the dilution water valve opening has a greater influence on the dilution water flow than on the total mass flow of the pine line. Thus, the noncommutative matrix $\mathbf{M}_{pdval2} = \begin{bmatrix} 1 & 1 \\ 0 & 1 \end{bmatrix}$ is used to represent the knowledge between the arc <*pdval2*, *pflow2*> and <*pdval2*, *pcon2*>. The noncommutative knowledge matrix $\mathbf{M}_{cdval2} = \begin{bmatrix} 1 & 1 \\ 0 & 1 \end{bmatrix}$ for the node *cdval2* was formed, which represents the relationship between the arc <*cdval2*, *cflow2*> and <*cdval2*, *ccon2*>, was formed for the same reason.

The commutative knowledge matrix $\mathbf{M}_{pflow2} = \begin{bmatrix} 1 & 0 \\ 0 & 1 \end{bmatrix}$ was formed for the node *pflow2*. It represents the relationship between the arc <*pflow2*, *pcon2*> and <*pflow2*, *conm2*>. The reason for this is that a process fault at the dilution point in the pine line, which causes the inconsistency in the arc < *pflow2*, *pcon2*>, e.g. the fluctuation of the variable *spcon*, does not affect transportation of the solid content from *pflow2* sensor to the blend chest (See Equation 5.4). Furthermore, a process fault between the dilution point and the *pflow2* sensor, e.g. a pipe leakage, causing the inconsistency in arc <*pflow2*, *pcon2*>, does not affect transportation of the solid content from *pflow2* sensor to the blend chest either. However, in the case that a process fault occurs after the *pflow2* sensor in the pine line, e.g. a pipe leakage, causing the inconsistency of the arc <*pflow2*, *conm2*>, then this has no/ effect on the mixing model of the dilution point, which is represented by the arc <*pflow2*, *pcon2*>. Similarly, the commutative knowledge matrices $\mathbf{M}_{cflow2} = \begin{bmatrix} 1 & 0 \\ 0 & 1 \end{bmatrix}$ and $\mathbf{M}_{broflow2} = \begin{bmatrix} 1 & 0 \\ 0 & 1 \end{bmatrix}$ were formed for the node *cflow2* and *broflow2*,

which represent the relationships between the arc <*cflow2*, *ccon2*> and <*cflow2*, *conm2*>, the arc <*broflow2*, *brocon2*> and <*broflow2*, *conm2*>, respectively.

For the nodes *ppress2*, *pspeed2*, *cpress2*, *cspeed2*, *broval2*, *brodval2*, *pcon2*, *ccon2*, *brocon2*, which have only one output, the scalar 1 was assigned as their knowledge matrices.

The knowledge matrix $\mathbf{M}_{sp2}$ for the stock preparation of layer 2 is formed by merging these knowledge matrices for the nodes, as shown below:

$$\begin{aligned}
&\mathbf{M}_{pdval2} = \begin{bmatrix} 1 & 1 \\ 0 & 1 \end{bmatrix}; \mathbf{M}_{cdval2} = \begin{bmatrix} 1 & 0 \\ 0 & 1 \end{bmatrix}; \mathbf{M}_{pflow2} = \begin{bmatrix} 1 & 0 \\ 0 & 1 \end{bmatrix}; \mathbf{M}_{cflow2} = \begin{bmatrix} 1 & 0 \\ 0 & 1 \end{bmatrix}; \\
&\mathbf{M}_{broflow2} = \begin{bmatrix} 1 & 0 \\ 0 & 1 \end{bmatrix}; \mathbf{M}_{ppress2} = 1; \mathbf{M}_{pspeed2} = 1; \mathbf{M}_{cpress2} = 1; \mathbf{M}_{cspeed2} = 1; \\
&\mathbf{M}_{broval2} = 1; \mathbf{M}_{brodval2} = 1; \mathbf{M}_{pcon2} = 1; \mathbf{M}_{ccon2} = 1; \mathbf{M}_{brocon2} = 1; \\
&\mathbf{M}_{sp2} = \text{blockdiag}(\mathbf{M}_{pdval2}, \mathbf{M}_{cdval2}, \mathbf{M}_{pflow2}, \mathbf{M}_{cflow2}, \mathbf{M}_{broflow2}, \mathbf{M}_{ppress2}, \mathbf{M}_{pspeed2} \\
&\qquad \mathbf{M}_{cpress2}, \mathbf{M}_{cspeed2}, \mathbf{M}_{broval2}, \mathbf{M}_{brodval2}, \mathbf{M}_{pcon2}, \mathbf{M}_{ccon2}, \mathbf{M}_{brocon2})
\end{aligned} \tag{5.13}$$

The arcs represented by each row of the matrix $\mathbf{M}_{sp2}$ are shown in Table 10.

5.2.2.2 Inter-arc knowledge matrix for the short circulation of layer 2

In the causal digraph model for the short circulation of layer 2 shown in Figure 41, the knowledge matrices of nodes with output arcs were first formed on the basis of the process knowledge.

The knowledge matrix

$$\mathbf{M}_{headflow22} = \begin{bmatrix} 1 & 1 & 1 & 0 \\ 0 & 1 & 0 & 0 \\ 0 & 1 & 1 & 0 \\ 0 & 0 & 0 & 1 \end{bmatrix} \tag{5.14}$$

was formed for the node *headflow22*. It represents the relationship between the arc <*headflow22*, *scflow2*>, <*headflow22*, *acceptcon2*>, <*headflow22*, *headcon2*> and <*headflow22*, *drybw123*>. First of all, the arc <*headflow22*, *scflow2*> represents the cause-effect relationship from the variable *headflow22* to *scflow2*, because the mass flow through the headbox affects the pressure of the outlet of the basis weight pump. The arc <*headflow22*, *acceptcon2*> represents the cause-effect relationship from the variable *headflow22* to *acceptcon2* by determining the mixing ratio of thick stock to white water. The arc <*headflow22*, *headcon2*> represent the cause-effect relationship from the variable *headflow22* to *headcon2*, in determining the mixing ratio of the hydrocyclone accept stock to the white water. Thus, the inconsistency in the arc <*headflow22*, *scflow2*>, e.g. a plug in the accept outlet of the hydrocyclone, implies that the pipe network from basis weight pump through the accept outlet of the hydrocyclone towards the headbox feed pump has changed which, in turn, results in the inconsistency in the arcs <*headflow22*, *acceptcon2*> and <*headflow22*, *headcon2*>, because the mixing ratios have changed. In contrast, changes in the mixing ratio do not always result in an inconsistency in the arc <*headflow22*, *scflow2*>, e.g. a plug in the reject outlet of the hydrocyclone. Furthermore, the mixing ratios represented by <*headflow22*, *acceptcon2*> and <*headflow22*, *headcon2*> do not always change simultaneously. For example, a plug in the reject outlet of the hydrocyclone causes a change in the mixing ratio before the hydrocyclone, while the mixing ratio after hydrocyclone remains constant. On the other hand, a plug in the accept outlet of the hydrocyclone or a plug in the pipe from the wire pit to the headbox feed pump causes an inconsistency in both arcs. Finally, a fault that occurs on the arc <*headflow22*, *drybw123*> is located after the headbox, and has no relationship with faults taking place before the headbox.

The knowledge matrix $\mathbf{M}_{headcon2} = \begin{bmatrix} 1 & 1 \\ 1 & 1 \end{bmatrix}$ was formed for the node *headcon2*. It represents the relationship between the arcs <*headcon2*, *wpcon2*> and <*headcon2*, *drybw2*>. It is obvious that faults on these two arcs always occur simultaneously in accordance with the solid content material balance. When a larger or smaller proportion of the fibre in the headbox is transported to the final products, the proportion of fibre passing to the wire pit changes accordingly.

The knowledge matrix $\mathbf{M}_{wpcon2} = \begin{bmatrix} 1 & 0 \\ 0 & 1 \end{bmatrix}$ was formed for the node *wpcon2*. It represents the relationship between the arcs <*wpcon2*, *acceptcon2*> and <*wpcon2*, *headcon2*>. The arc <*wpcon2*, *acceptcon2*> describes the cause-effect relationship from the variable *wpcon2* to *acceptcon2*, which is the accept ratio of the hydrocyclone. Similarly, the arc <*wpcon2*, *headcon2*> describes the accept ratio of the machine screen. Therefore, these two arcs have no effect on each other.

For the nodes *headspeed2*, *sliceopen2*, *bwspeed2*, *sccon2*, *scflow2*, *acceptcon2*, which have only one output, the scalar 1 was assigned as their knowledge matrices.

The knowledge matrix $\mathbf{M}_{sc2}$ for the short circulation of layer 2 is formed by combining these knowledge matrices for the nodes as shown below:

$$\mathbf{M}_{headspeed2} = 1;\ \mathbf{M}_{sliceopen2} = 1;\ \mathbf{M}_{bwspeed2} = 1;\ \mathbf{M}_{sccon2} = 1;\ \mathbf{M}_{scflow2} = 1;$$
$$\mathbf{M}_{acceptcon2} = 1;\ \mathbf{M}_{headflow22} = \begin{bmatrix} 1 & 1 & 1 & 0 \\ 0 & 1 & 0 & 0 \\ 0 & 1 & 1 & 0 \\ 0 & 0 & 0 & 1 \end{bmatrix};\ \mathbf{M}_{headcon2} = \begin{bmatrix} 1 & 1 \\ 1 & 1 \end{bmatrix};\ \mathbf{M}_{wpcon2} = \begin{bmatrix} 1 & 0 \\ 0 & 1 \end{bmatrix}; \quad (5.15)$$
$$\mathbf{M}_{sc2} = \text{blockdiag}(\mathbf{M}_{headspeed2}, \mathbf{M}_{sliceopen2}, \mathbf{M}_{bwspeed2}, \mathbf{M}_{sccon2}, \mathbf{M}_{scflow2}$$
$$\mathbf{M}_{acceptcon2}, \mathbf{M}_{headflow22}, \mathbf{M}_{headcon2}, \mathbf{M}_{wpcon2})$$

The arcs represented by each row of the matrix $\mathbf{M}_{sc2}$ are shown in Table 12.

The obtained inter-arc knowledge matrix $\mathbf{M}_{sc2}$ needs to be further modified by Equation 3.11 according to the knowledge between the arcs that do not share parent node. The following knowledge is considered.

- The arcs <*scflow2*, *acceptcon2*>, <*sccon2*, *acceptcon2*>, and <*wpcon2*, *acceptcon2*> describe the hydrocyclone accept ratio, and the arc <*headflow22*, *acceptcon2*> describes the mixing ratio of the thick stock to white water. A fault of the hydrocyclone accept ratio change usually implies a plug problem in the hydrocyclone which always changes the mixing ratio of thick stock to white water. In contrast, a change in the mixing ratio does not always result in a change in the hydrocyclone accept ratio, e.g. a pipe plug after hydrocyclone. Thus $\mathbf{M}_{sc2}$ is accordingly modified as

$$\mathbf{M}_{sc2}(5,4) = \mathbf{M}_{sc2}(5,8) = \mathbf{M}_{sc2}(5,13) = \mathbf{M}_{sc2}(4,5) = \mathbf{M}_{sc2}(4,8) = \mathbf{M}_{sc2}(4,13)$$
$$= \mathbf{M}_{sc2}(13,4) = \mathbf{M}_{sc2}(13,5) = \mathbf{M}_{sc2}(13,8) = 1 \quad (5.16)$$

- The arcs <*headspeed2*, *headflow22*> and <*sliceopen2*, *headflow22*> describe the pipe network from the headbox feed pump to the headbox, while the arcs <*acceptcon2*, *headcon2*> and <*wpcon2*, *headcon2*> describe the accept ratio

of the machine screen. Therefore, for the same reason explained in item 1, an inconsistency in the arcs <*acceptcon2*, *headcon2*> and <*wpcon2*, *headcon2*> always results in an inconsistency in the arcs <*headspeed2*, *headflow22*> and <*sliceopen2*, *headflow22*>, but not vice versa. Furthermore, an inconsistency of the arc <*headspeed2*, *headflow22*> and <*sliceopen2*, *headflow22*> always occurs simultaneously, because they describe the same pipe network. Thus, $\mathbf{M}_{sc2}$ is accordingly modified as

$$\begin{aligned}&\mathbf{M}_{sc2}(1,2)=\mathbf{M}_{sc2}(2,1)=\mathbf{M}_{sc2}(6,14)=\mathbf{M}_{sc2}(6,1)=\mathbf{M}_{sc2}(6,2)\\&=\mathbf{M}_{sc2}(14,6)=\mathbf{M}_{sc2}(14,1)=\mathbf{M}_{sc2}(14,2)=1\end{aligned} \tag{5.17}$$

- A change in the pipe network leading to an inconsistency in the arcs <*headflow22*, *acceptcon2*> and <*headflow22*, *headcon2*> has an effect on the pipe network between the headbox feed pump and the headbox, leading to an inconsistency in the arcs, <*headspeed2*, *headflow22*> and <*sliceopen2*, *headflow22*>, but not vice versa. Thus $\mathbf{M}_{sc2}$ is accordingly modified as

$$\mathbf{M}_{sc2}(8,1)=\mathbf{M}_{sc2}(8,2)=\mathbf{M}_{sc2}(9,1)=\mathbf{M}_{sc2}(9,2)=1 \tag{5.18}$$

The inter-arc knowledge matrices for the stock preparation and short circulation of the layer 2 have now been formed. The inter-arc knowledge matrices for the other stock preparation and short circulations can be formed in a similar fashion. The knowledge matrix **M** for the whole digraph model shown in Figure 51 can be formed as

$$\mathbf{M}=\text{blockdiag}\left(\mathbf{M}_{sp13},\mathbf{M}_{sp2},\mathbf{M}_{sc1},\mathbf{M}_{sc2},\mathbf{M}_{sc3}\right) \tag{5.19}$$

The matrix **M** was used to locate the process fault on the arcs and this, in turn, helps to identify the faulty process component in the case of a process type of fault.

5.3 Fault scenario study

Four different fault scenarios were selected for the study on the basis of an interview with the plant operator. The scenarios were a consistency sensor fault in the stock preparation of layer 2, a retention drop fault, a headbox feed pump fault, and a hydrocyclone plug fault in the short circulation of layer 2.

5.3.1 Consistency sensor fault in the stock preparation of layer 2

Consistency sensors are some of the most important process instruments in papermaking. They are used in many parts of the process, primarily in stock preparation and in the short circulation, where the quality of the stock and paper are controlled. For example, one of the main quality variables, the dry basis weight, is controlled with measurements from the mass flow and consistency sensors in the thick stock flow out of the machine chest.

The performance of the consistency sensors also plays an important role in the economics of paper mills. In the stock preparation, as seen in Figure 30, the consistency of each individual pulp line is controlled with dilution water, while the setpoint of the mass flow for the each pulp line is calculated from the recipes and the measured consistencies. Thus, accurate measurement of the individual stock components before mixing is crucial in guaranteeing that the correct recipes are prepared. The great importance of the consistency sensors is a considerable incentive to maintain and calibrate them more frequently than the other types of sensor.

A fault in the consistency sensor of the pine line in the stock preparation of layer 2 was studied as an example, because there are five consistency sensors in the process shown in Figure 30. Using the board machine model in APROS, the fault was simulated by introducing a -0.1% negative bias to the selected sensor. The total simulation time was 43 200 seconds (12 hours) with 10 seconds as the sampling time. Grade 1 was in the first 5 hours and grade 2 in the last 7 hours. The fault was introduced during the time period 3 600-10 800 s and the time period 28 800-36 000 s, respectively, for the two different board grades. Due to the effect of the controller for pine consistency, a faulty measurement tries to track its setpoint, which makes it difficult to notice the occurrence of a fault. Furthermore, the controller will drive the real value of the pine consistency higher than the setpoint due to the faulty measurement, which lead to an increase in the ratio of pine in the final stock. Since the pine pulp is usually more expensive than CTMP, more money will be spent on manufacturing the same amount of production. The real value of the pine consistency, the measured value of the pine consistency and the ratio of the pine consistency to CTMP, are shown in Figure 52.

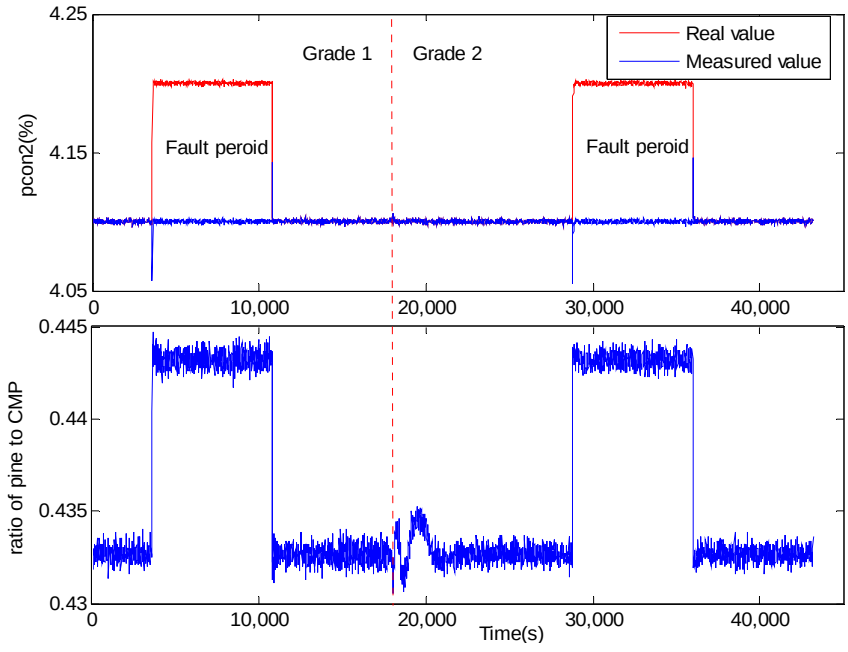

Figure 52. Effect of fault scenario 1.

5.3.2 A retention drop fault in the short circulation of layer 2

The paper web is formed on the wire, onto which the stock is sprayed from the headbox. The fibre materials are retained on the wire, while the water flows through the web and the wire. Retention is a measure of how much of the original solid material is retained on the wire, and is mainly dependent on the structure of the wire, the composition of the stock, e.g. the level of flocculation, and the chemical state of the process. A sudden drop in retention can occur in the process due to a change in the chemical state or missoperation of the former.

Using the board machine model in APROS, the fault was simulated by changing the retention rate of the former from 90% to 87%. The total simulation time was 43 200 seconds (12 hours) with 10 seconds as the sampling time. Grade 1 was in the first 5 hours and grade 2 in the last 7 hours. A fault was introduced during the time period 3 600-10 800 s and the time period 28 800-36 000 s respectively for the two different board grades. Due to the effect of the fault, the fibre transport ability was impaired, which means a lower percentage of the fibre can reach the final production. Although the quality control for the dry basis weight maintained the paper quality in accordance with the setpoint, the paper machine was running inefficiently.

5.3.3 A headbox feed pump fault in the short circulation of layer 2

The headbox feed pump is used to supply stock to the headbox. Its main task is to provide a constant flow and pressure to the headbox without any pulsations. The demands on pump reliability and structure are extremely high. Any faults or malfunctions in the headbox feed pump will be very quickly reflected in the quality of the product (Weise et al., 2000, p160).

In APROS, the characteristic of the pump is described by a pump curve – a parabola shaped curve that is defined by the parameters maximum head, nominal head and

nominal volumetric flow. Using the board machine model in APROS, the headbox feed pump fault was simulated by changing the maximum head and the nominal head from 24 m to 23 m and 20.5 m to 19.5 m, respectively. The total simulation time was 39 600 seconds (11 hours) with 10 seconds as the sampling time. Grade 1 was in the first 5 hours and grade 2 in the last 6 hours. The fault was introduced during the time period 3 600-10 800 s and the time period 25 200-32 400 s, respectively, for the two different board grades.

In reality, the corresponding fault is a head drop in the pump due to the cavitation phenomenon. A sudden drop in the maximum and nominal head reduces the performance. Although the jet:wire ratio controller increases the rotation speed of the pump in order to track the setpoint, a higher ration speed increases the energy consumption and produces more pulsation in the pressure in the headbox.

5.3.4 A hydrocyclone plug fault in the short circulation of layer 2

Hydrocyclones are a part of the stock cleaning system in the approach flow system. They are used to remove unwanted particles and impurities such as shives, pieces of bark and sand so that they do not end up in the product (Weise et al., p.146). The hydrocyclones are usually located between the wire pit and the deculator, but in the studied board machine there is no deculator, so the stock is fed straight to the headbox after hydrocyclone cleaning.

The operating principle of the hydrocyclones is centrifugal cleaning. Particles that have different density or shape compared to the wood fibres are removed from the reject outlet. As a result, the reject outlet is vulnerable to plugging. Shives, pieces of bark or some pitch particles in the feedstock can become stuck in the reject outlet of the hydrocyclone and plug it later on.

The phenomena involved in hydrocyclone plugging are twofold. First, the pressure loss between the inlet of the hydrocyclone and the reject outlet is increased by the presence of the plug which, in turn, results in a decrease in the reject mass flow and an increase in the accept mass flow. Second, the fibre or solid content accept ratio is increased due to the plug, which affects the quality variable of the board, the dry basis weight.

Using the board machine model in APROS, a hydrocyclone plug fault was simulated by changing the reject outlet parameter 'pressure lost coefficient' from 7 to 9 and the accept ratio for fibre from 0.85 to 0.87. The total simulation time was 39 600 seconds (11 hours) with 10 seconds as the sampling time. Grade 1 was in the first 5 hours and grade 2 in the last 6 hours. The fault was introduced during the time period 3 600-10 800 s and the time period 25 200-32 400 s, respectively, for the two different board grades.

5.4 Fault diagnosis results with the enhanced dynamic causal digraph method

The proposed EDCDG method was applied using the causal digraph model (See Figure 51 in Section 5.2.1 and Appendix A), the inter-arc knowledge matrix (See Equation 5.19 in Section 5.2.2) and the faulty data obtained from the fault scenario simulation in APROS. The procedures - residual generation, different fault effect separation and residual modification, fault detection, fault isolation and locating the fault on the arcs, have already been dealt with. The results for the four fault scenarios are presented in the following.

5.4.1 Fault diagnosis results for the consistency sensor fault in the pine line

The first fault scenario is a sensor fault for the fibre consistency in the pine line of the stock preparation for layer 2. The *GRs* were first generated using the data collected from

the simulation of fault scenario 1. Next, residual detection was performed using the CUSUM method. The only detected variable was *pcon2*, whose global simulation value, global residual and the detected result are illustrated in Figure 53. Thirdly, the fault isolation rules clearly inferred that the fault was local, and the fault nature rules that it was a sensor fault according to the local residuals shown in Figure 54. Finally, the fault propagation path for the fault period is shown as the result of fault diagnosis in Figure 55. Due to the nature of the fault, neither fault separation nor inference between the arcs was performed.

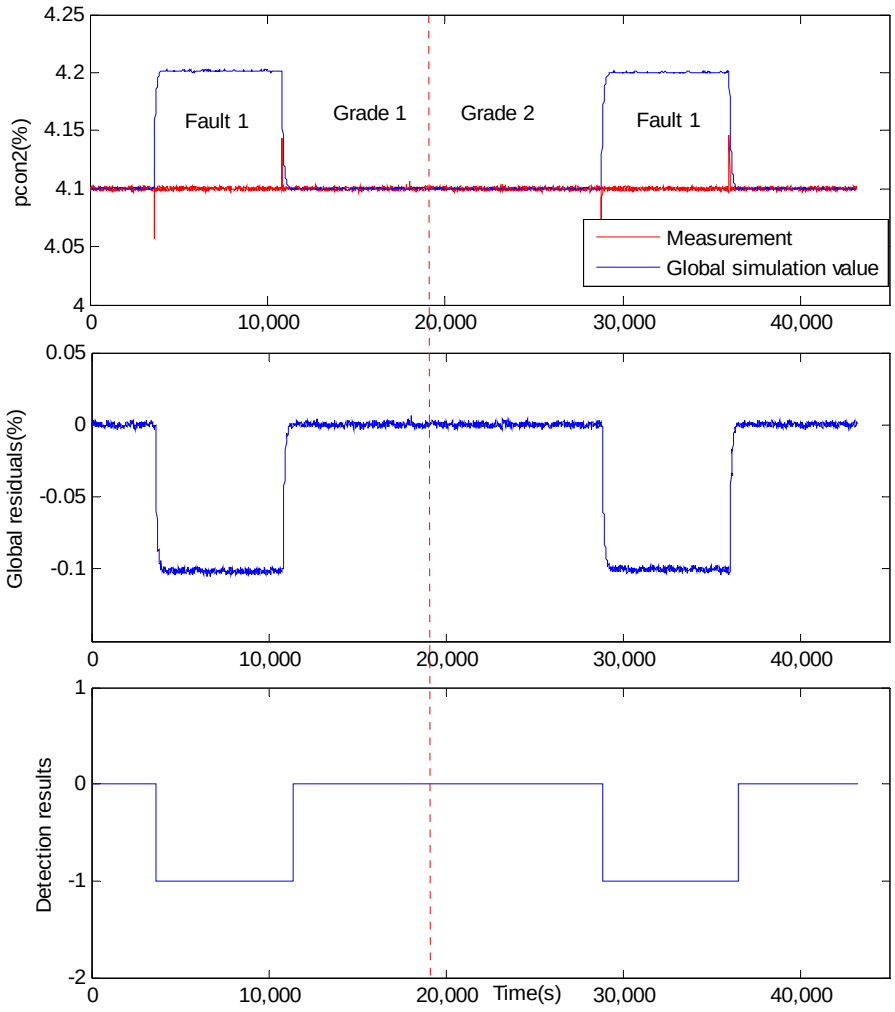

Figure 53. Global residual and detection results for the variable *pcon2*.

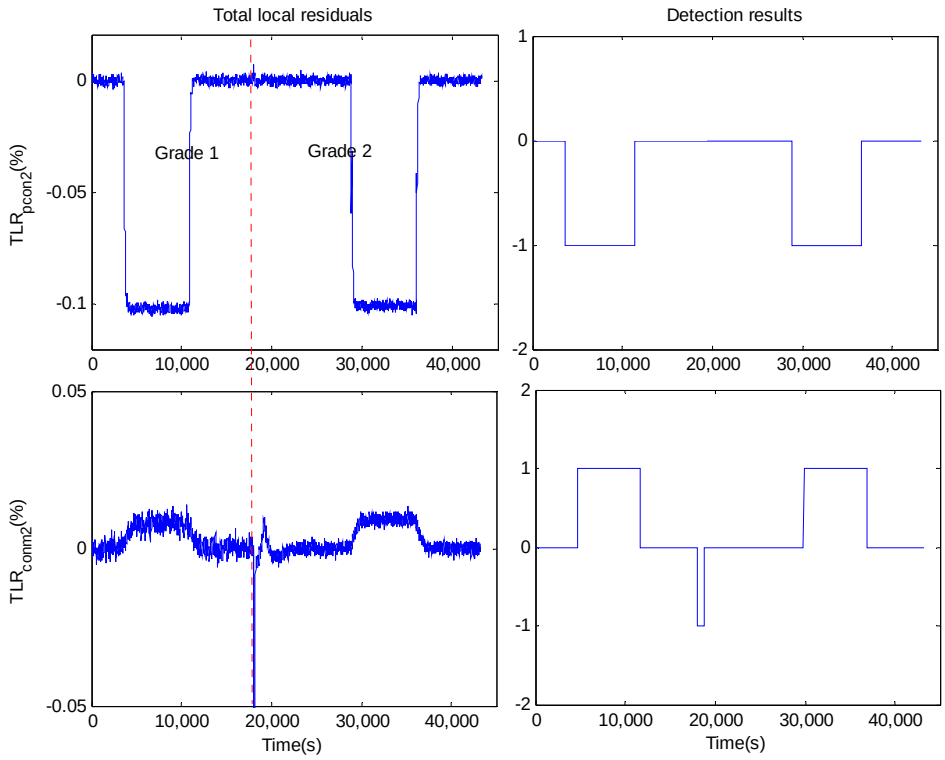

Figure 54. TLR_{pcon2} and TLR_{conm2}.

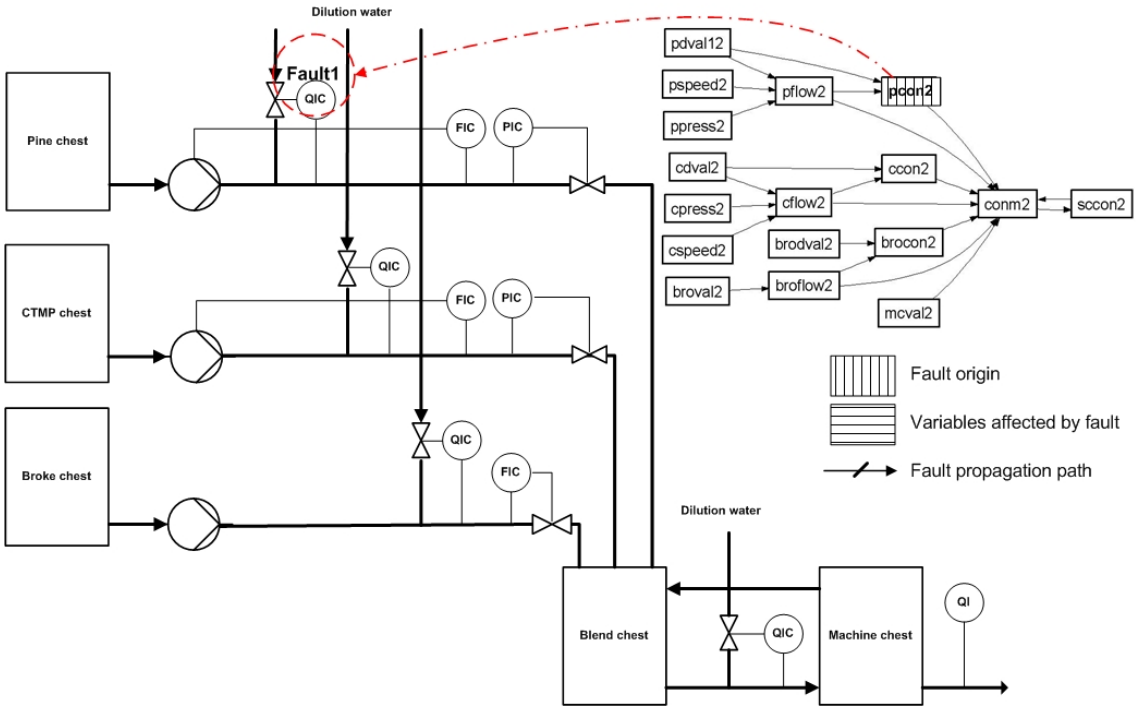

Figure 55. Fault diagnosis results for the fault scenario 1.

5.4.2 Fault diagnosis results for the process fault in the retention drop

The second fault scenario is a process fault in the retention drop of the short circulation for layer 2. The *GRs* were first generated using the data collected from the simulation of fault scenario 2. Next, the global residual detection was performed using the CUSUM method. The detection set was formed by the variables: *acceptcon2*, *headcon2* and *wpcon2*, whose global residuals and detection results are shown in Figure 56.

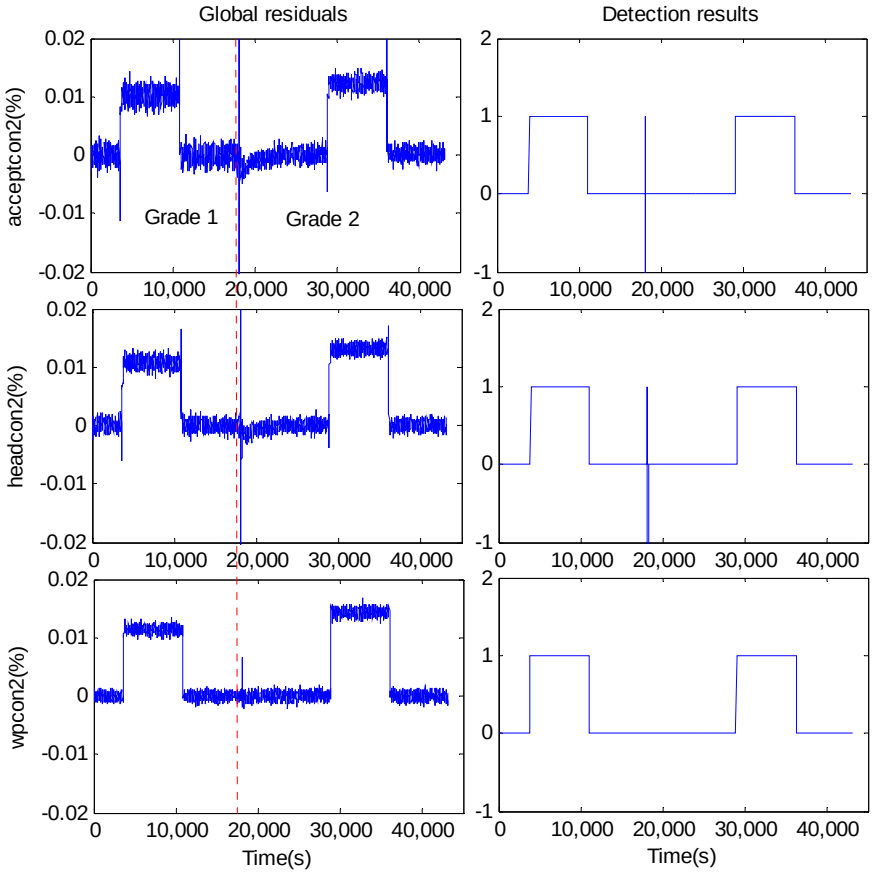

Figure 56. Global residuals and the detection results for the variables *acceptcon2*, *headcon2*, *wpcon2*.

Next, the local residuals were generated for the variables in the detection set, some of which are shown in Figure 57. The fault isolation rules and fault nature rules were then applied to the generated *LR*s. The origin of the fault was located on the variable *wpcon2*,

while the nature of the fault was identified as a process fault. The preliminary fault propagation path was therefore formed, as shown in Figure 58.

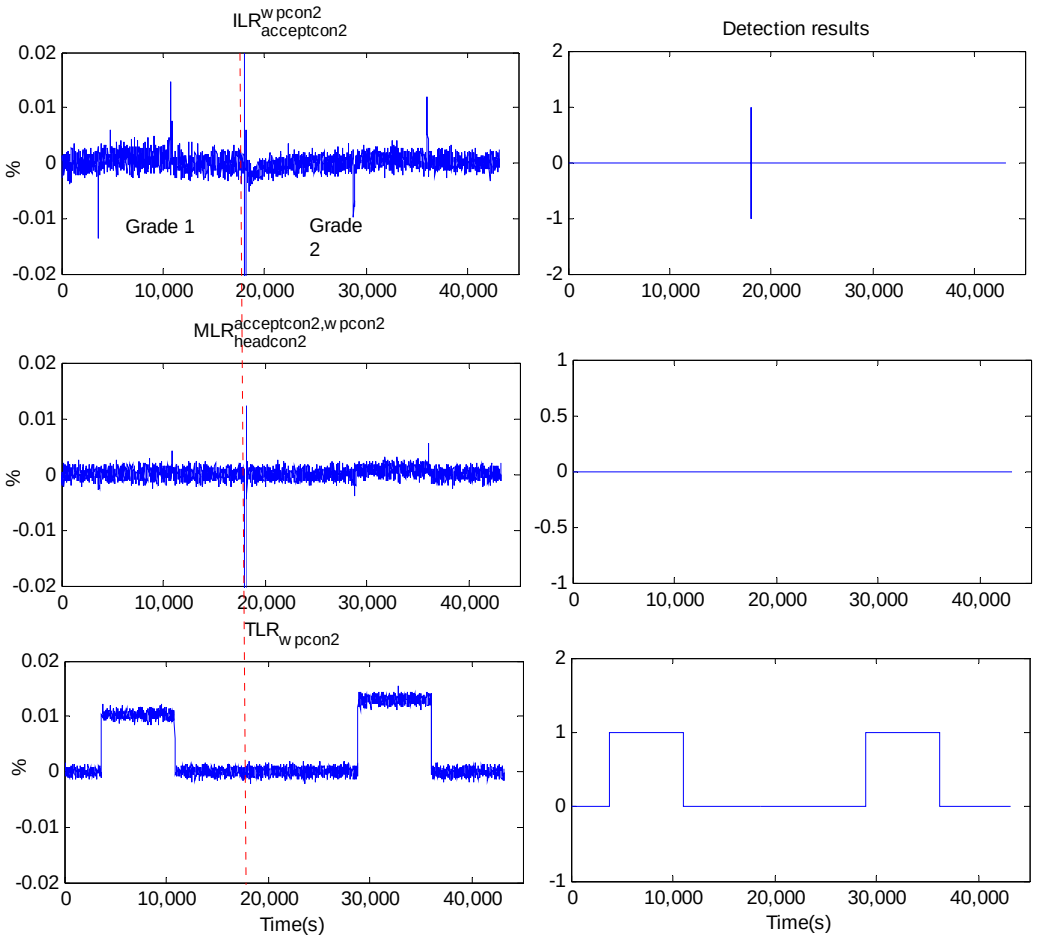

Figure 57. $ILR_{acceptcon2}^{wpcon2}$, $MLR_{headcon2}^{\text{acceptcon2},wpcon2}$ and TLR_{wpcon2}.

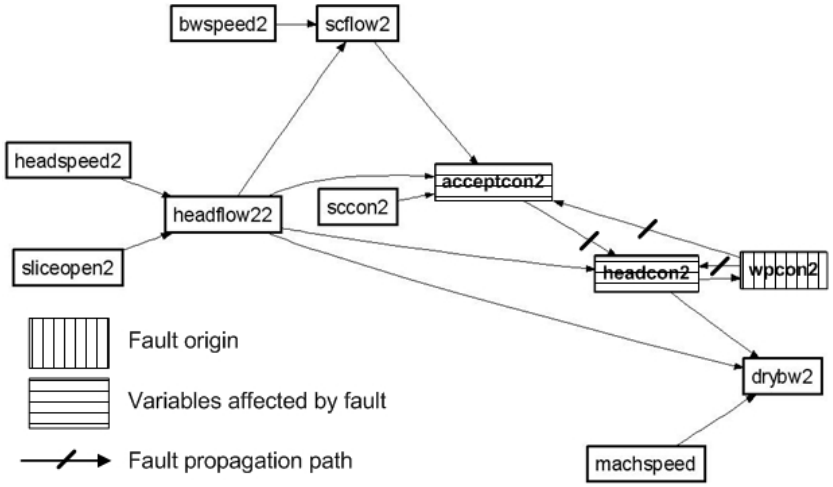

Figure 58. The preliminary fault propagation path of fault scenario 2.

Since the identified fault is a process fault, the approach for separating fault effects was applied to those variables whose parent nodes had global detections. The fault separation set $FSS = \{drybw2\}$ was first formed according to Equation 3.6, provided $IndexU_{drybw2} = \{headcon2\}$. The different fault effects were then calculated as

$$\begin{aligned} contp_{drybw2}^{headcon2} &= GR_{drybw2} - ILR_{drybw2}^{headcon2} \\ contl_{drybw2} &= TLR_{drybw2} \end{aligned} \tag{5.20}$$

The generated fault effects are shown in Figure 59.

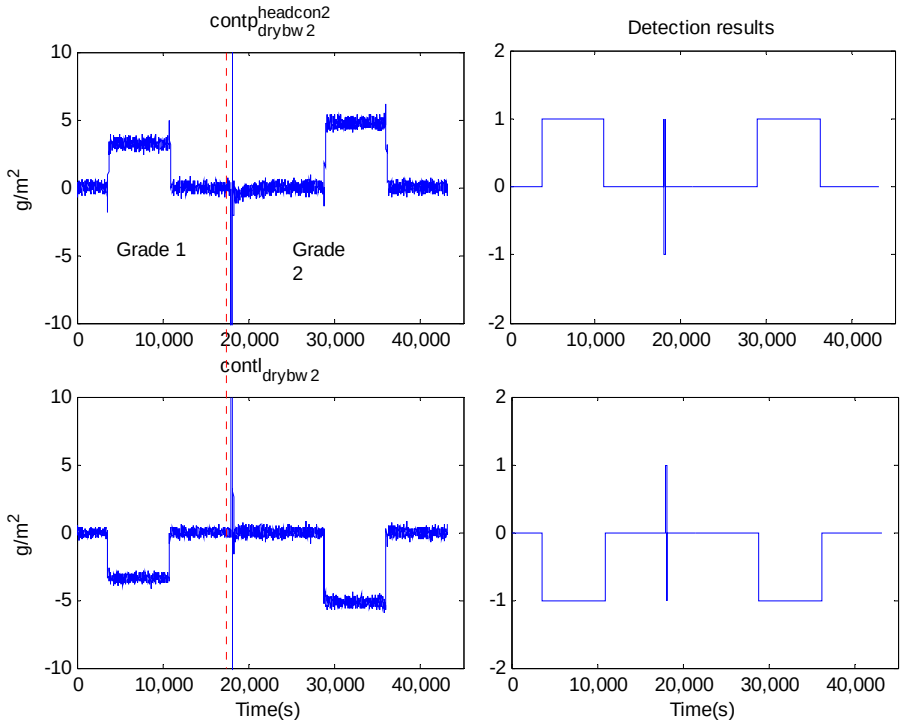

Figure 59. $contp_{drybw2}^{headcon2}$ and $contl_{drybw2}$.

Thus in the third step of the fault effect separation, the set PFE_{drybw2} is formed as $\left\{contp_{drybw2}^{headcon2}\right\}$, while the set NFE_{drybw2} is an empty set.

In the fourth step, the CUSUM method was applied to the local fault effect contribution $contl_{drybw2}$ and the element in the set PFE_{drybw2}, according to the algorithm in Figure 12. The detection results shown in Figure 59 indicate that there are two fault effects on the variable *drybw2*. The first one is the fault effect propagated from the variable *headcon2* with a positive direction, while the second fault is the local fault on the variable *drybw2* with a negative direction. Cancellation of these two fault effects makes the global residual of the variable *drybw2* disappear, as shown in Figure 60.

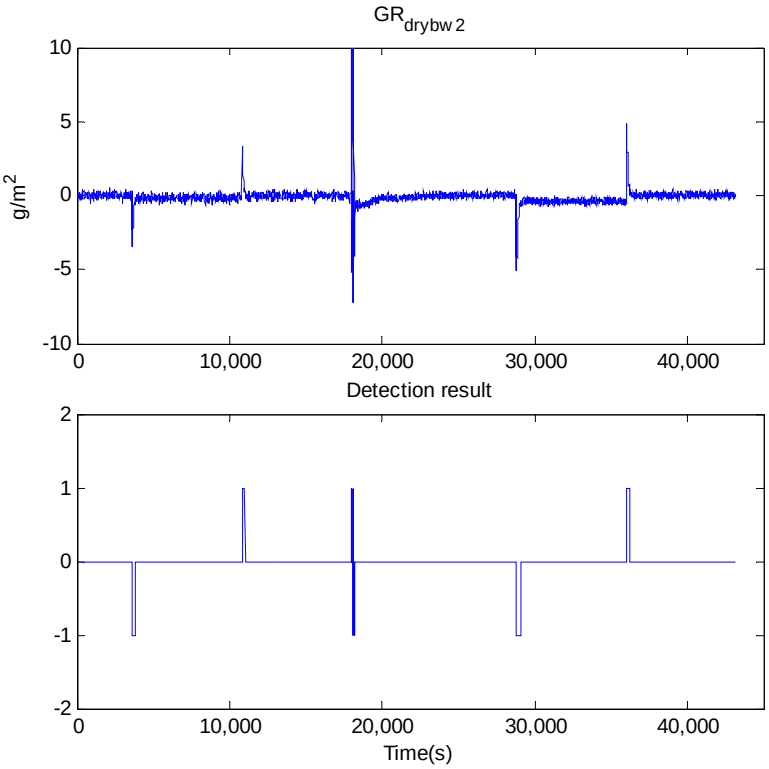

Figure 60. GR_{drybw2} and the detection result.

Therefore, the preliminary fault propagation path in Figure 58 was then modified as shown in Figure 61.

Since the identified fault is a process fault, location of the process fault is performed in order to find the responsible process component. However, spurious results were produced due to the multiple fault origins and the multiple input arcs for each fault origin. In Figure 61 the input arcs for fault origin nodes *wpcon2* and *drybw2* are {<*headcon2*, *wpcon2*>} and {<*headcon2*, *drybw2*>, <*headflow22*, *drybw2*>, <*machspeed*, *drybw2*>}, respectively. Thus the number of sets of suspected arcs is $1 \cdot (2^3 - 1) = 8$, which are {<*headcon2*, *wpcon2*>, <*headcon2*, *drybw2*>}, {<*headcon2*, *wpcon2*>, <*headflow22*, *drybw2*>}, {<*headcon2*, *wpcon2*>, <*machspeed*, *drybw2*>}…

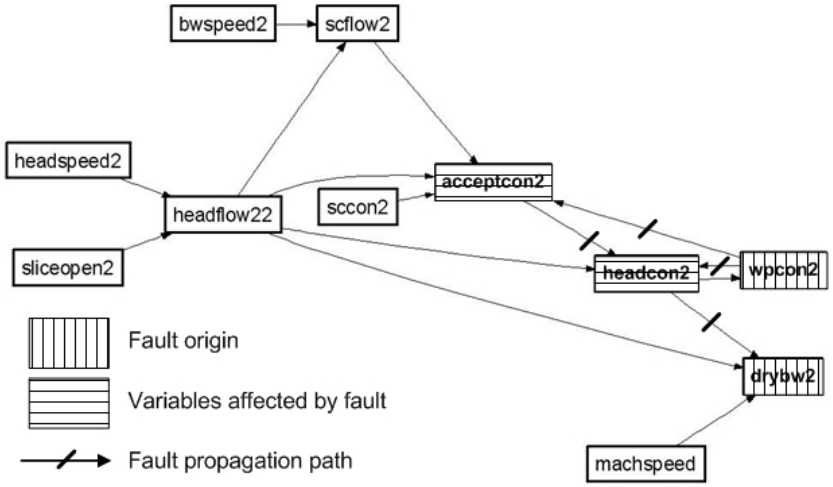

Figure 61. Fault propagation path of the fault scenario 2.

Since the fault origins were located in the short circulation of layer 2, only the sub matrix $\mathbf{M}_{sc2}$ of the whole digraph matrix **M** was tested with the 8 sets of suspected arcs according to Equation 3.13. The set of suspected arcs {<*headcon2*, *wpcon2*>, <*headflow22*, *drybw2*>} is considered as an example. The **sv** for this set is

$$\mathbf{sv} = \begin{bmatrix} 0 & 0 & 0 & 0 & 0 & 0 & 0 & 0 & 0 & 1 & 1 & 0 & 0 & 0 \end{bmatrix} \tag{5.21}$$

and the test with Equation 3.13 is performed as follows:

$$\begin{aligned} &NUM(\mathbf{sv}) = 2 \neq NUM(\mathbf{sv} \cdot \mathbf{M}_{sc2}) = \\ &NUM(\begin{bmatrix} 0 & 0 & 0 & 0 & 0 & 0 & 0 & 0 & 0 & 1 & 1 & 1 & 0 & 0 \end{bmatrix}) = 3 \end{aligned} \tag{5.22}$$

Thus, the set {<*headcon2*, *wpcon2*>, <*headflow22*, *drybw2*>} cannot be a possible result. The set {<*headcon2*, *wpcon2*>, <*headcon2*, *drybw2*>} is considered as another example. The **sv** for the set is

$$\mathbf{sv} = \begin{bmatrix} 0 & 0 & 0 & 0 & 0 & 0 & 0 & 0 & 0 & 0 & 1 & 1 & 0 & 0 \end{bmatrix} \tag{5.23}$$

and the test with Equation 3.13 is performed as follows:

$$\begin{aligned} &NUM(\mathbf{sv}) = 2 = NUM(\mathbf{sv} \cdot \mathbf{M}_{sc2}) = \\ &NUM(\begin{bmatrix} 0 & 0 & 0 & 0 & 0 & 0 & 0 & 0 & 0 & 0 & 2 & 2 & 0 & 0 \end{bmatrix}) = 2 \end{aligned} \tag{5.24}$$

Thus, this set is accepted as a possible result. After testing all the sets of suspected arcs, only four were left as possible results: {<*headcon2*, *wpcon2*>, <*headcon2*, *drybw2*>}, {<*headcon2*, *wpcon2*>, <*headcon2*, *drybw2*>, <*headflow22*, *drybw2*>} {<*headcon2*, *wpcon2*>, <*headcon2*, *drybw2*>, <*machspeed*, *drybw2*>} and {<*headcon2*, *wpcon2*>, <*headcon2*, *drybw2*>, <*headflow22*, *drybw2*>, <*machspeed*, *drybw2*>}. Using the inference mechanism between the arcs reduced the number of possible results from 21 to 4.

The fault diagnosis results, i.e. the four sets of suspected arcs, provide valuable information needed in identifying the faulty process component in the case of a process fault. The four sets consist of the common arcs <*headcon2*, *wpcon2*> and <*headcon2*, *drybw2*>. The first arc corresponds to the process components: a former section and the white water tray, while the second arc, <*headcon2*, *drybw2*>, corresponds to the process components: a former section, a wet press and a drying group. Thus, the suspected process component is the former section, since it is located on both arcs. The result is illustrated in Figure 62. Moreover, the direction of the TLR_{wpcon2}, as shown in Figure 57, implies that the direction of the fault is a drop in fibre retention, rather than an increase in fibre retention.

In this fault scenario, the fault effects separation approach was applied to locate the correct fault origins; using the inference mechanism between the arcs significantly

decreased the number of possible fault results and the process fault was located on the arcs, which subsequently helps in identifying the faulty process component, i.e. a former section.

The improvement in the enhanced method over the conventional one can be seen clearly when comparing the results. Firstly in the terms of fault detection, the conventional method only detected 3 variables, *acceptcon2*, *headcon2*, and *wpcon2*, while the enhanced method was able to detect one more variable, *drybw2*, with the modified residuals. Secondly, the result of the fault isolation was improved by the inference between the arcs. The conventional method identified the fault origin variables, *wpcon2* and *drybw2*, while the suspected arcs were also identified by the proposed method. In addition, the corresponding possible faulty process component was identified as a former section.

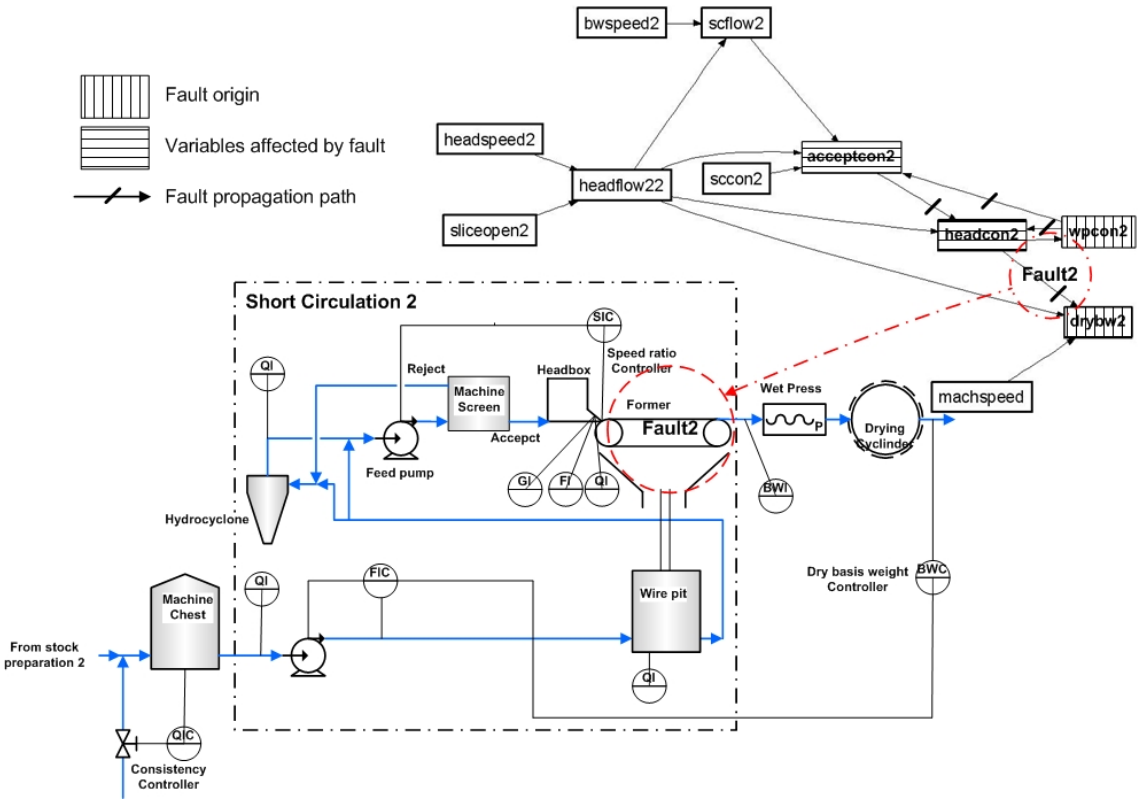

Figure 62. Fault diagnosis results for the fault scenario 2.

5.4.3 Fault diagnosis results for the process fault of the headbox feed pump head drop

The third fault scenario is a process fault in the drop of the headbox feed pump head in the short circulation for layer 2. The *GRs* were first generated using the data collected from the simulation of the fault scenario 3. Next, the global residuals detection was performed using the CUSUM method. The detection set was formed by the variables: *headflow22*, and *headcon2*, the global residuals and detection results of which are shown in Figure 63.

Next, the local residuals were generated for the variables in the detection set, some of which are shown in Figure 64. The fault isolation rules and fault nature rules were then applied to the generated *LR*s. The fault origin was located on the variable *headflow22*, while the nature of the fault was identified as a process fault. The preliminary fault propagation path was therefore formed, as shown in Figure 65.

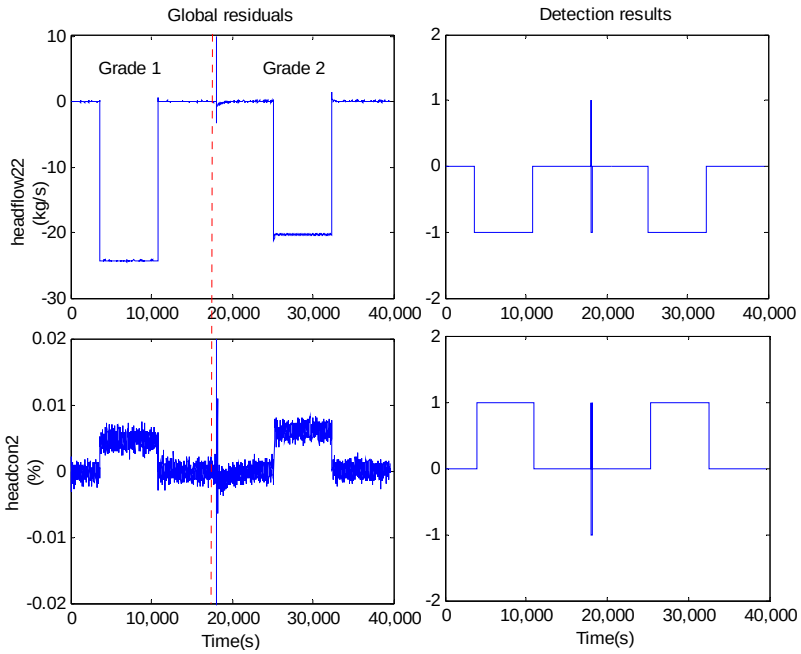

Figure 63. Global residuals and detection results for the variables *headflow22* and *headcon2*.

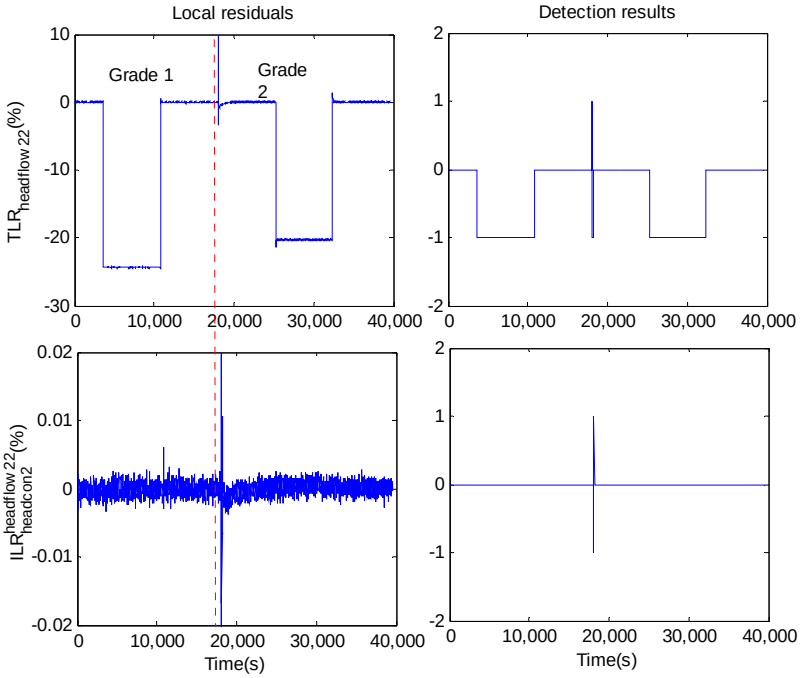

Figure 64. $TLR_{headflow22}$ and $ILR^{headflow22}_{headcon2}$.

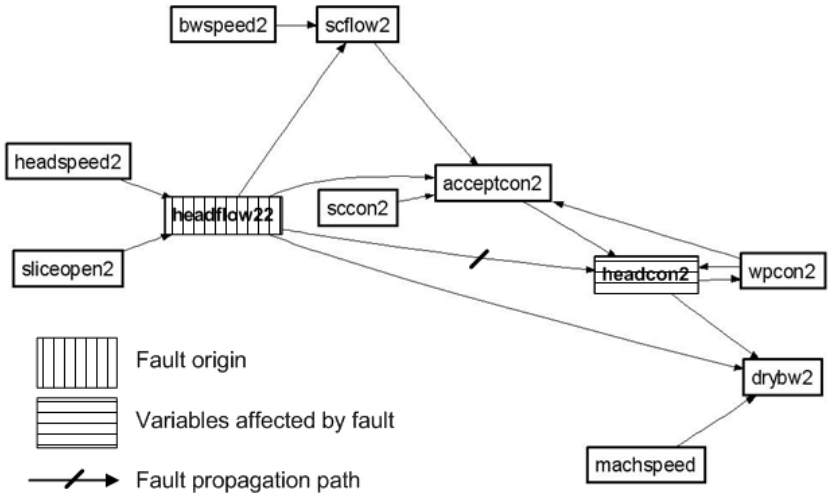

Figure 65. The preliminary fault propagation path of the fault scenario 3.

Since the identified fault is a process fault, the approach for separating fault effects was applied to the variables whose parent nodes had global detections. The fault separation

set $FSS = \{drybw2, acceptcon2, wpcon2, scflow2\}$ was first formed according to Equation 3.6 with $IndexU_{drybw2} = \{headcon2, headflow22\}$, $IndexU_{acceptcon2} = \{headflow22\}$ and $IndexU_{wpcon2} = \{headcon2\}$. Secondly, the different fault effects were calculated for the variables *drybw2*, *acceptcon2* and *wpcon2,* respectively, as

$$
\begin{aligned}
contp_{drybw2}^{headcon2} &= GR_{drybw2} - ILR_{drybw2}^{headcon2} \\
contp_{drybw2}^{headflow22} &= GR_{drybw2} - ILR_{drybw2}^{headflow22} \\
contl_{drybw2} &= TLR_{drybw2} \\
contp_{acceptcon2}^{headflow22} &= GR_{acceptcon2} - ILR_{acceptcon2}^{headflow22} \\
contl_{acceptcon2} &= TLR_{acceptcon2} \\
contp_{wpcon2}^{headcon2} &= GR_{wpcon2} - ILR_{wpcon2}^{headcon2} \\
contl_{wpcon2} &= TLR_{wpcon2} \\
contp_{scflow2}^{headflow22} &= GR_{scflow2} - ILR_{scflow2}^{headflow22} \\
contl_{scflow2} &= TLR_{scflow2}
\end{aligned}
\tag{5.25}
$$

The contributions of the fault effects generated for the variables *drybw2*, *acceptcon2* and *wpcon2* are shown in Figure 66, Figure 67, Figure 68 and Figure 69, respectively.

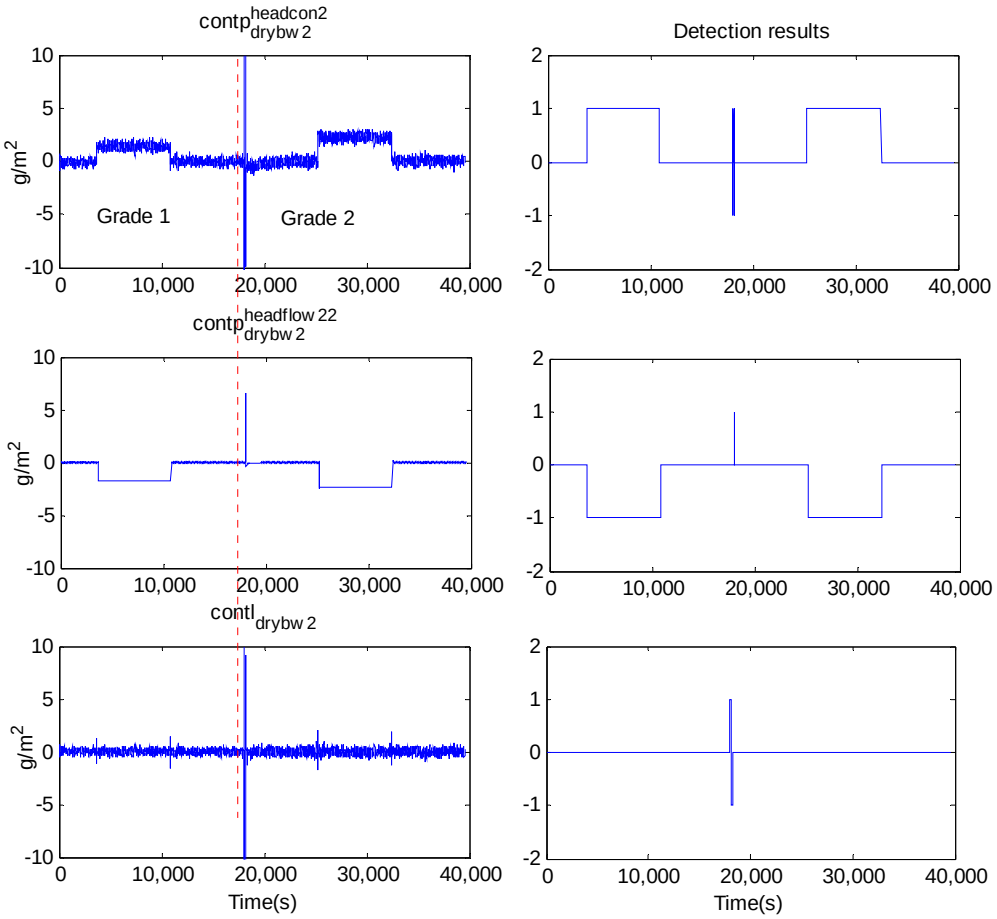

Figure 66. $contp^{headcon2}_{drybw2}$, $contp^{headflow22}_{drybw2}$ and $contl_{drybw2}$.

Thus, in the third step of the fault effect separation, the set PFE_{drybw2}, NFE_{drybw2}, $PFE_{acceptcon2}$, $NFE_{acceptcon2}$, $PFE_{headcon2}$, $NFE_{headcon2}$, $PFE_{scflow2}$ and $NFE_{scflow2}$, are formed as $\{contp^{headcon2}_{drybw2}\}$, $\{contp^{headflow22}_{drybw2}\}$, $\{contp^{headflow22}_{acceptcon2}\}$, empty set, $\{contp^{headcon2}_{wpcon2}\}$, empty set, empty set and $\{contp^{headflow22}_{scflow2}\}$, respectively.

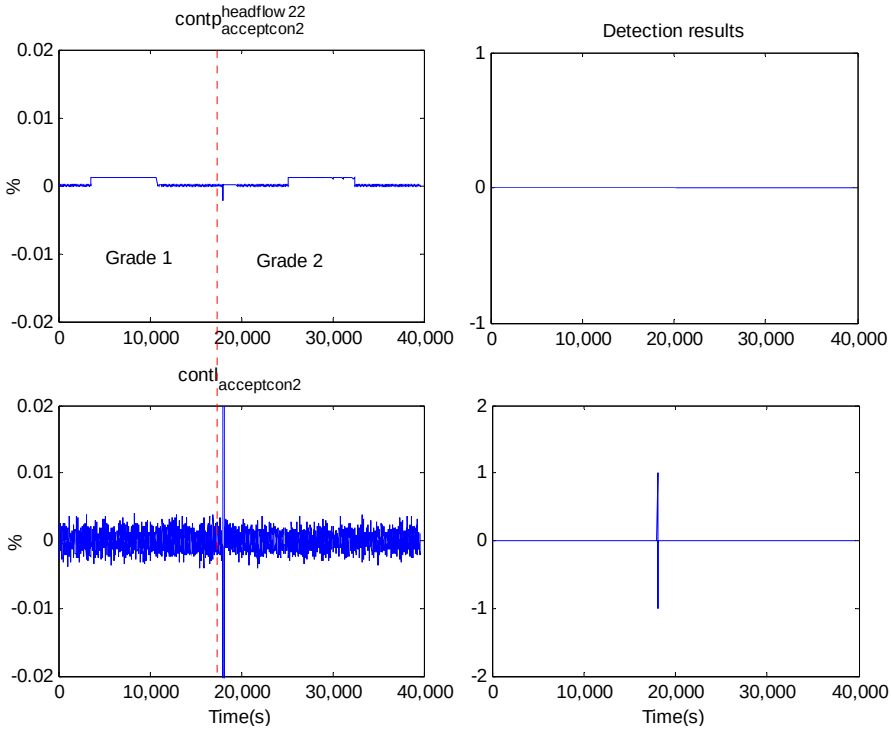

Figure 67. $contp^{headflow22}_{acceptcon2}$ and $contl_{acceptcon2}$.

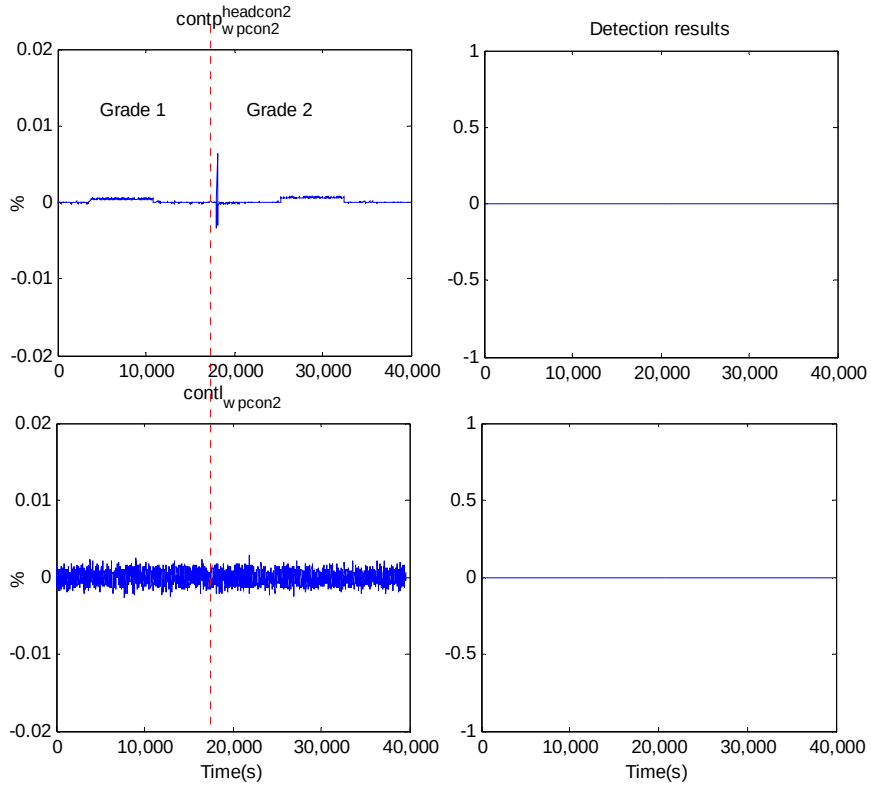

Figure 68. $contp^{headcon2}_{wpcon2}$ and $contl_{wpcon2}$.

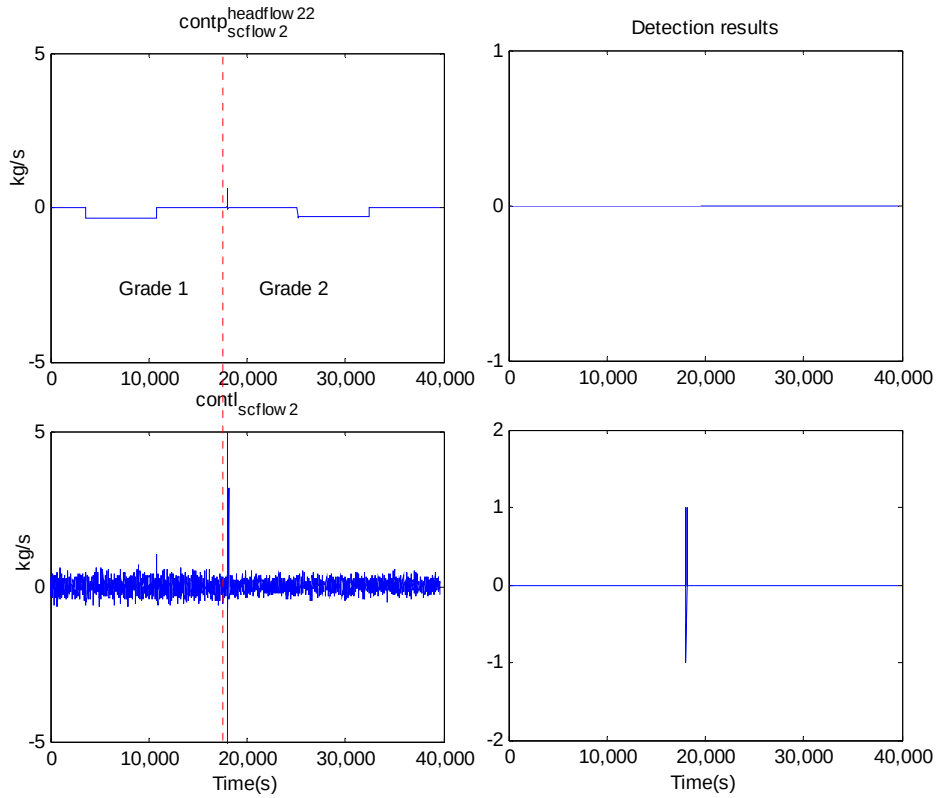

Figure 69. $contp_{scflow2}^{headflow22}$ and $contl_{scflow2}$.

In the fourth step, the CUSUM method was applied to the local fault effect contributions and the fault effect contributions from the parent nodes according to the algorithm in Figure 12. The detection results shown in Figure 66 imply that there are no local fault effects, while the variable *drybw2* is detected because of the fault effects propagated from the variables *headcon2* and *headflow22*. In the figure, the fault effect contribution from *headcon2* is positive, while that from *headflow22* is negative. The different directions of the fault effects from the parent nodes cancelled out each other, which makes the global residual of the variable *drybw2* to disappear, as shown in the following.

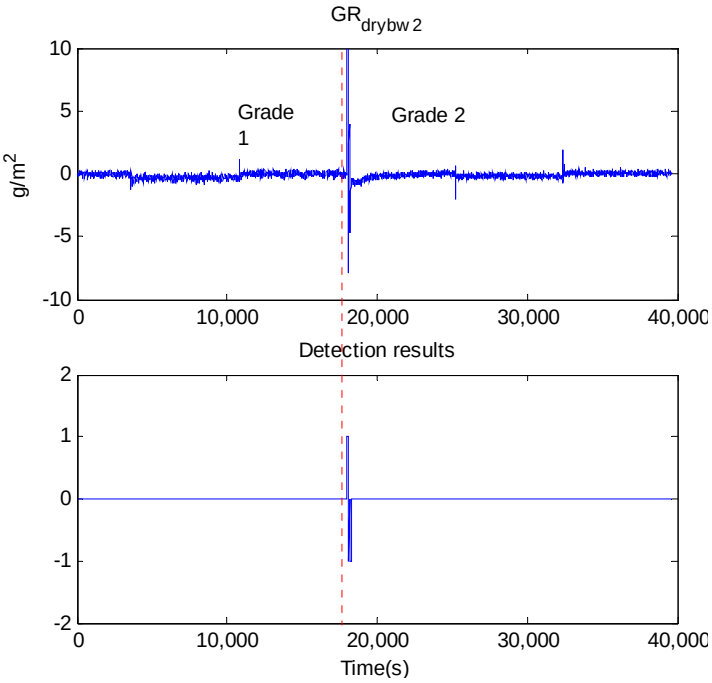

Figure 70. GR_{drybw2} and the detection result.

Furthermore, it can be seen from Figure 67, Figure 68 and Figure 69 that there are no detections for $contp_{acceptcon2}^{headflow22}$, $contl_{acceptcon2}$, $contp_{wpcon2}^{headcon2}$, $contl_{wpcon2}$, $contp_{scflow2}^{headflow22}$ and $contl_{scflow2}$. This implies that there is neither a significant local fault effect nor any significant fault effects from the parent nodes. Thus, the variables *acceptcon2*, *wpcon2* and *scflow2* are considered as fault free. The preliminary fault propagation path in Figure 65 was therefore subsequently modified as in Figure 71.

Since the identified fault is a process fault, location of the process fault is performed to find the responsible process component. In Figure 71, the input arcs for fault origin node *headflow22* are <*headspeed2*, *headflow22*> and <*sliceopen2*, *headflow22*>. Thus, the number of sets of suspected arcs is $(2^2 - 1) = 3$, which are {<*headspeed2*, *headflow22*>}, {<*sliceopen2*, *headflow22*>}, and {<*headspeed2*, *headflow22*>, <*sliceopen2*, *headflow22*>}.

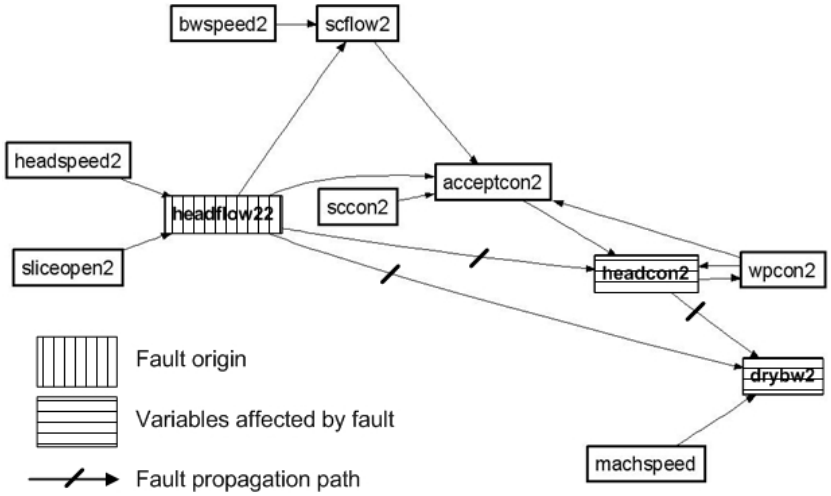

Figure 71. Fault propagation path of the fault scenario 3.

Since the fault origins were located in the short circulation of layer 2, only the sub matrix $\mathbf{M}_{sc2}$ of the whole digraph matrix **M** was tested to test with the 3 sets of suspected arcs according to Equation 3.13. The set of suspected arcs {<*headspeed2*, *headflow22*>} is considered as an example. The **sv** for this set is

$$\mathbf{sv} = \begin{bmatrix} 1 & 0 & 0 & 0 & 0 & 0 & 0 & 0 & 0 & 0 & 0 & 0 & 0 & 0 \end{bmatrix} \tag{5.26}$$

and the test with Equation 3.13 is performed as follows:

$$\begin{aligned} &NUM(\mathbf{sv}) = 1 \neq NUM(\mathbf{sv} \cdot \mathbf{M}_{sc2}) = \\ &NUM(\begin{bmatrix} 1 & 1 & 0 & 0 & 0 & 0 & 0 & 0 & 0 & 0 & 0 & 0 & 0 & 0 \end{bmatrix}) = 2 \end{aligned} \tag{5.27}$$

Thus the set {<*headspeed2*, *headflow22*>} cannot be a possible result. The set {<*headspeed2*, *headflow22*>, <*sliceopen2*, *headflow22*>} is considered as another example. The **sv** for the set is

$$\mathbf{sv} = \begin{bmatrix} 1 & 1 & 0 & 0 & 0 & 0 & 0 & 0 & 0 & 0 & 0 & 0 & 0 & 0 \end{bmatrix} \tag{5.28}$$

and the test with Equation 3.13 is performed as follows:

$$\begin{aligned} &NUM(\mathbf{sv}) = 2 = NUM(\mathbf{sv} \cdot \mathbf{M}_{sc2}) = \\ &NUM(\begin{bmatrix} 2 & 2 & 0 & 0 & 0 & 0 & 0 & 0 & 0 & 0 & 0 & 0 & 0 & 0 \end{bmatrix}) = 2 \end{aligned} \tag{5.29}$$

Thus this set is accepted as a possible result. After testing all the sets of suspected arcs, only one was left as a possible result, {<*headspeed2*, *headflow22*>, <*sliceopen2*, *headflow22*>}. Using the inference mechanism between the arcs decreased the number of possible results decreased from 3 to 1.

The fault diagnosis results, i.e. the set of suspected arcs, provide valuable information needed in identifying the faulty process component in the case of a process fault. The sets consisted of the arcs, <*headspeed2*, *headflow22*> and <*sliceopen2*, *headflow22*>. Both of these arcs represent the pipe networks between the headbox feed pump and the headbox. Thus, the suspected process components are the pipe components located in this network. In actual fact in this case it is impossible to distinguish between different pipe component faults, e.g. a headbox feed pump fault, and a pipe plug or wear. The result is illustrated in Figure 72. Moreover, the direction of the $TLR_{headflow22}$, as shown in Figure 64, implies that the fault is a head drop in the headbox feed pump or a plug in the pipe.

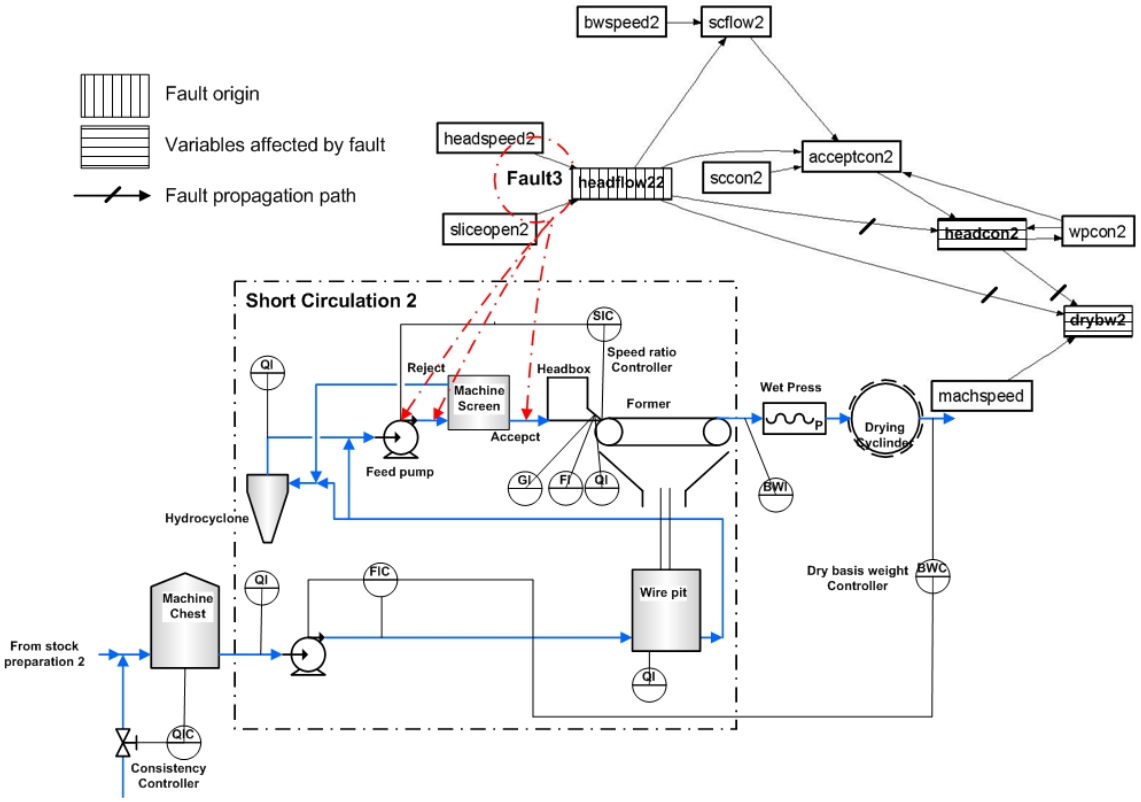

Figure 72. Fault diagnosis results for fault scenario 3.

In this fault scenario, the fault effects separation approach was applied to locate the correct fault origins; using the inference mechanism between the arcs, the number of possible fault results decreased and the process fault was located on the arcs. This subsequently helps to identify the faulty process components, e.g. the pipe network between the headbox feed pump and the headbox.

5.4.4 Fault diagnosis results for the process fault of the hydrocyclones plug

The fourth fault scenario is a process fault caused by a hydrocyclone plug in the short circulation for layer 2. The *GRs* were first generated using the data collected from the simulation of fault scenario 4. Next, the global residual detection was performed using the CUSUM method. The detection set was formed by the variables *headflow22*,

acceptcon2, *headcon2*, and *drybw2*, the global residuals and detection results of which are shown in Figure 73.

Next, the local residuals were generated for the variables in the detection set, some of which are shown in Figure 74. The fault isolation rules and fault nature rules were then applied to the generated *LR*s. The origin of the fault was located in the variable *headflow22* and *acceptcon2*, while the nature of the fault was identified as a process fault. The preliminary fault propagation path was formed, as shown in Figure 65.

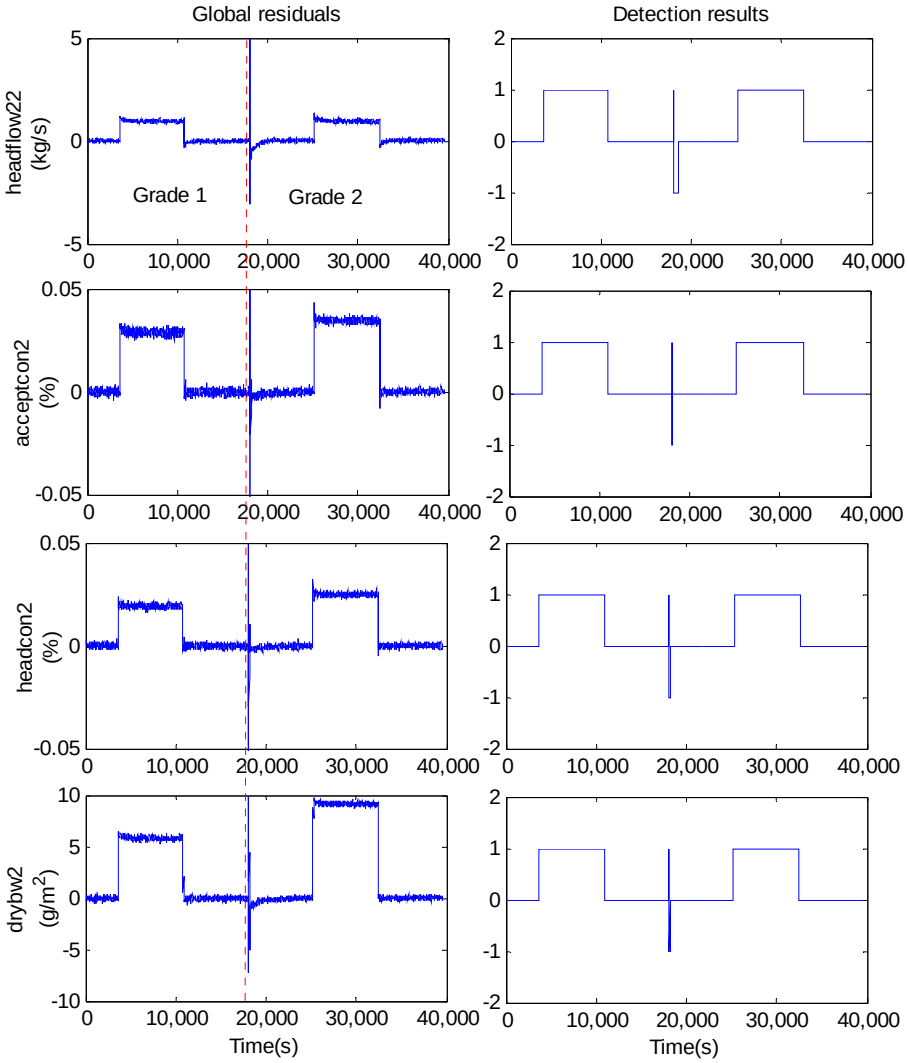

Figure 73. Global residuals and detection results for the variables *headflow22*, *acceptcon2*, *headcon2*, *drybw2*.

Since the identified fault is a process fault, the approach for separating fault effects was applied to the variables whose parent nodes have global detections. The fault separation set $FSS = \{scflow2, wpcon2\}$ was first formed according to Equation 3.6 using $IndexU_{scflow2} = \{headflow22\}$ and $IndexU_{wpcon2} = \{headcon2\}$. The different fault effects were then calculated for the variables *scflow2* and *wpcon2* respectively as

$$\begin{aligned} contp_{scflow2}^{headflow22} &= GR_{scflow2} - ILR_{scflow2}^{headflow22} \\ contl_{scflow2} &= TLR_{scflow2} \\ contp_{wpcon2}^{headcon2} &= GR_{wpcon2} - ILR_{wpcon2}^{headcon2} \\ contl_{wpcon2} &= TLR_{wpcon2} \end{aligned} \tag{5.30}$$

The generated contributions of the fault effect for the variables *scflow2* and *wpcon2* are shown in Figure 76 and Figure 77 respectively.

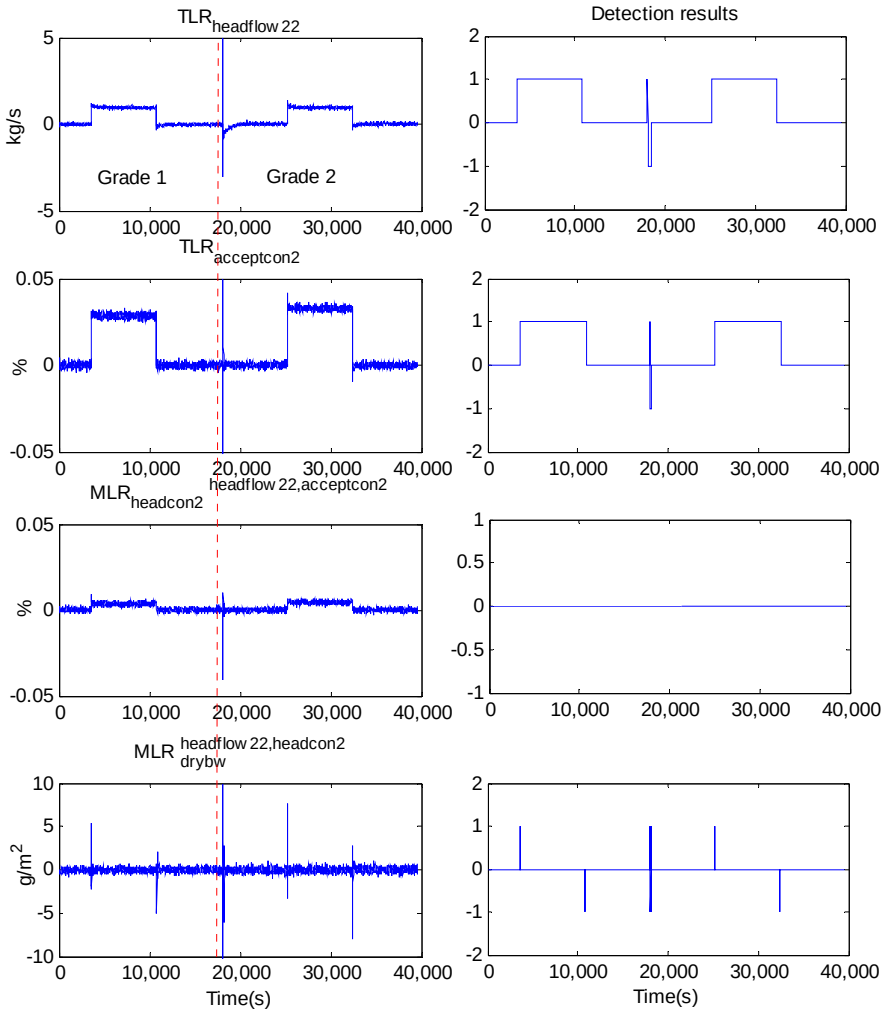

Figure 74. $TLR_{headflow22}$, $TLR_{acceptcon2}$, $MLR_{headcon2}^{headflow22,acceptcon2}$ and $MLR_{drybw2}^{headflow22,headcon2}$.

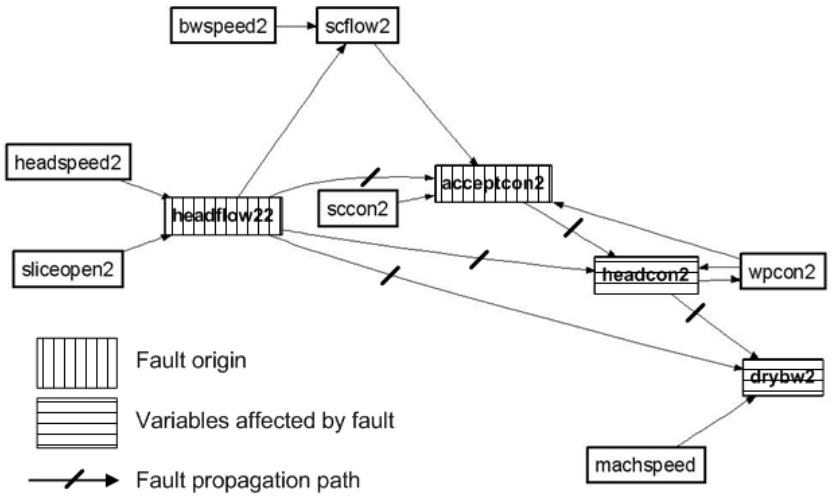

Figure 75. The preliminary fault diagnosis results for fault scenario 4.

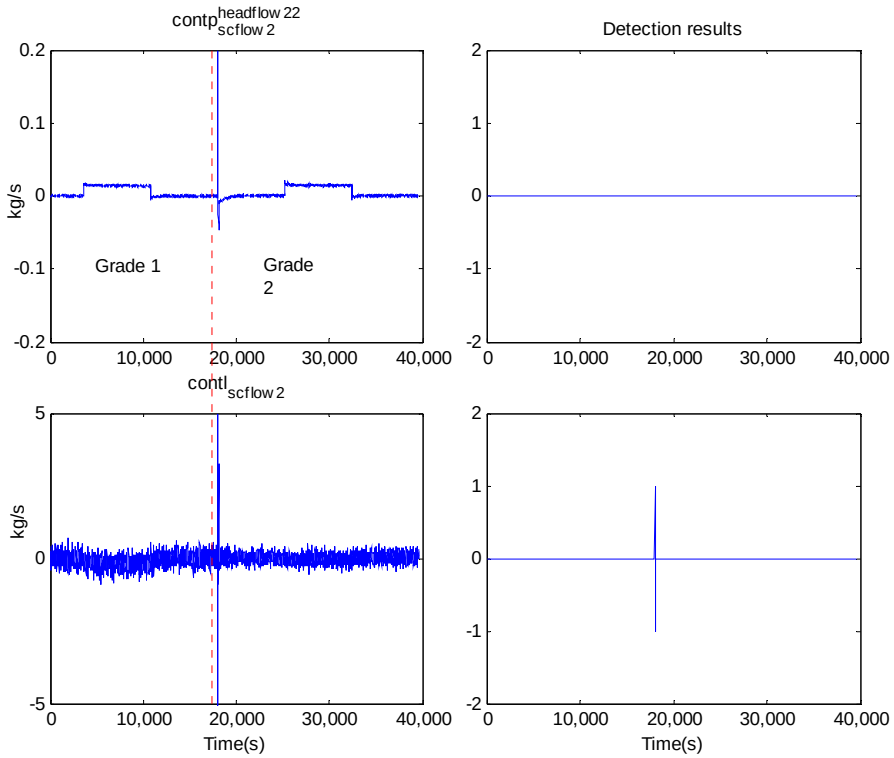

Figure 76. $contp_{scflow2}^{headflow22}$ and $contl_{scflow2}$.

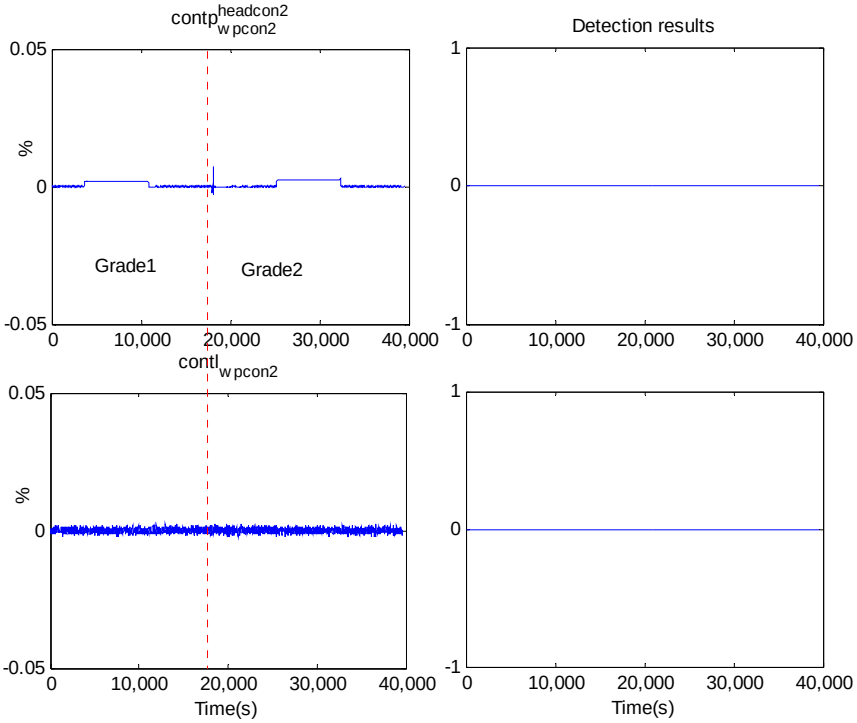

Figure 77. $contp_{wpcon2}^{headcon2}$ and $contl_{wpcon2}$.

In the third step of the fault effect separation, the set $PFE_{scflow2}$, $NFE_{scflow2}$, $PFE_{headcon2}$ and $NFE_{headcon2}$, are therefore formed respectively as $\{contp_{scflow2}^{headflow22}\}$, empty set, $\{contp_{wpcon2}^{headcon2}\}$, and empty set.

In the fourth step, the CUSUM method was applied to the local fault effect contributions and the fault effect contributions from the parent nodes according to the algorithm in Figure 12. The detection results shown in Figure 76 imply that both the local fault effects and the fault effects from the variable *headflow22* are too small to be detected. The same detection results were obtained for the variable *wpcon2*, as shown in Figure 77. Therefore these two variables are declared as fault free and the fault propagation path in Figure 75 remains the same.

Since the identified fault is a process fault, location of the process fault is performed in order to find the responsible process component. However, spurious results were produced due to the multiple fault origins and the multiple input arcs for each fault origin. In Figure 75 the input arcs for the fault origin nodes *headflow22* and *acceptcon2* are {<*headspeed2*, *headflow22*>, <*sliceopen2*, *headflow22*>} and {<*scflow2*, *acceptcon2*>, <*headflow22*, *acceptcon2*>, <*sccon2*, *acceptcon2*>, <*wpcon2*, *acceptcon2*>} respectively. Thus, the number of sets of suspected arcs is $(2^2-1)\cdot(2^4-1)=45$, which are {<*headspeed2*, *headflow22*>, <*scflow2*, *acceptcon2*>}, {<*sliceopen2*, *headflow22*>, <*headflow22*, *acceptcon2*>}, {<*headspeed2*, *headflow22*>, <*scflow2*, *acceptcon2*>, <*headflow22*, *acceptcon2*>}…

Since the fault origins were located in the short circulation of layer 2, only the sub matrix $\mathbf{M}_{sc2}$ of the whole digraph matrix **M** was tseted to test with the 45 sets of suspected arcs according to Equation 3.13. The set of suspected arcs {<*headspeed2*,

headflow22>, <*scflow2*, *acceptcon2*>} is considered as an example. The **sv** for this set is

$$\mathbf{sv} = \begin{bmatrix} 1 & 0 & 0 & 0 & 1 & 0 & 0 & 0 & 0 & 0 & 0 & 0 & 0 & 0 \end{bmatrix} \tag{5.31}$$

and the test with Equation 3.13 is performed as follows:

$$\begin{aligned} &NUM(\mathbf{sv}) = 2 \neq NUM(\mathbf{sv} \cdot \mathbf{M}_{sc2}) = \\ &NUM(\begin{bmatrix} 1 & 1 & 0 & 1 & 1 & 0 & 0 & 1 & 0 & 0 & 0 & 0 & 1 & 0 \end{bmatrix}) = 6 \end{aligned} \tag{5.32}$$

Thus, the set {<*headspeed2*, *headflow22*>, <*scflow2*, *acceptcon2*>} cannot be a possible result. The set {<*headspeed2*, *headflow22*>, <*sliceopen2*, *headflow22*>, <*headflow22*, *acceptcon2*>} is considered as another example. The **sv** for the set is

$$\mathbf{sv} = \begin{bmatrix} 1 & 1 & 0 & 0 & 0 & 0 & 0 & 1 & 0 & 0 & 0 & 0 & 0 & 0 \end{bmatrix} \tag{5.33}$$

and the test with Equation 3.13 is performed as follows:

$$\begin{aligned} &NUM(\mathbf{sv}) = 3 = NUM(\mathbf{sv} \cdot \mathbf{M}_{sc2}) = \\ &NUM(\begin{bmatrix} 3 & 3 & 0 & 0 & 0 & 0 & 0 & 1 & 0 & 0 & 0 & 0 & 0 & 0 \end{bmatrix}) = 3 \end{aligned} \tag{5.34}$$

Thus this set is accepted as a possible result. After testing all the sets of suspected arcs, only two were left as a possible result, {<*headspeed2*, *headflow22*>, <*sliceopen2*, *headflow22*>, <*headflow22*, *acceptcon2*>}, and {<*headspeed2*, *headflow22*>, <*sliceopen2*, *headflow22*>, <*sccon2*, *acceptcon2*>, <*scflow2*, *acceptcon2*>,

<*headflow22*, *acceptcon2*>, <*wpcon2*, *acceptcon2*>}. Using the inference mechanism between the arcs reduced the number of possible results from 45 to 2.

The fault diagnosis results, i.e. the set of suspected arcs, provide valuable information needed in identifying the faulty process component in the case of a process fault. The arcs in the first set imply a pipe fault, which could probably occur after the reject outlet of the hydrocyclone, after the accept outlet of the hydrocyclone and between the wire pit and the headbox feed pump. The arcs in the second set imply a hydrocyclone plug fault, which occurs in the reject outlet of the hydrocyclone. The faulty arcs also provide information about the fault phenomenon. The fault on the arcs <*headspeed2*, *headflow22*> and <*sliceopen2*, *headflow22*> indicates that the pipe network from the headbox feed pump to the headbox has changed from the fault-free situation. The fault on the arcs <*headflow22*, *acceptcon2*> indicates that the mixing ratio of thick stock to white water has changed during the fault period. Lastly, the fault on the arcs <*sccon2*, *acceptcon2*>, <*scflow2*, *acceptcon2*>, and <*wpcon2*, *acceptcon2*> implies that the fibre accept ratio of the hydrocyclone has also changed from the fault-free state. The result is illustrated in Figure 78. Furthermore, the direction of the $TLR_{acceptcon2}$, as shown in Figure 74, implies that the fibre accept ratio has decreased instead of increasing.

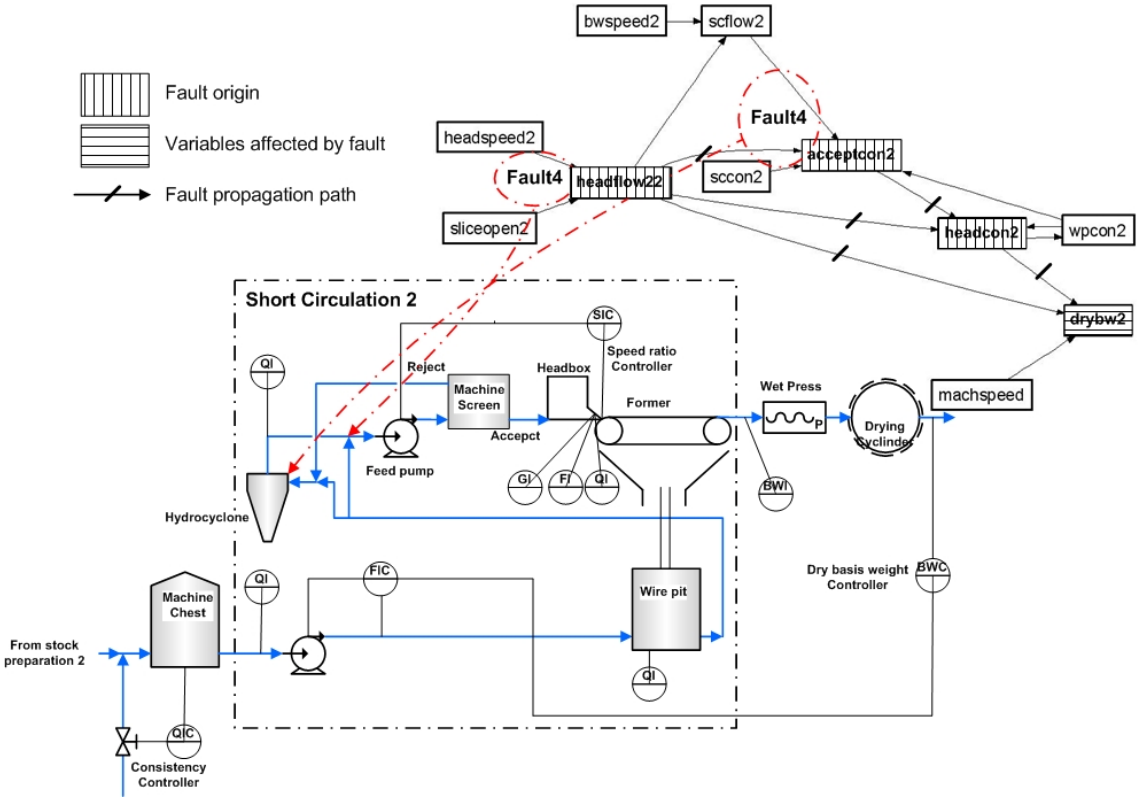

Figure 78. Fault diagnosis results for fault scenario 4.

In this fault scenario, the fault effects separation approach was applied to locate the correct origins of the fault; using the inference mechanism between the arcs decreased the number of possible fault results, and the process fault was located on the arcs. This subsequently helps to identify the faulty process components, e.g. a hydrocyclone plug, and a pipe network plug between the hydrocyclone and the headbox feed pump.

6 Summary of the results

The improvements in the proposed enhanced causal digraph method over the traditional dynamic causal digraph method are illustrated in two comparative studies. First, three different fault scenarios were tested with the proposed method in a paper machine short circulation process: an actuator fault (treated as a process fault), a sensor fault, and a process fault. The results for the second fault scenario, i.e. a sensor fault, showed that the conventional dynamic method was able to handle this case well. In the third scenario, which was a retention drop fault, the traditional method could not, however, detect the variables correctly. The correct nodes were detected for the third fault using the fault effects separation approach. In addition, the fault diagnosis results for the process fault, i.e. the first and third scenario, were also further improved by locating the process fault on the arcs using the proposed inference mechanism. The final results also showed that much more information is provided by the enhanced method as it can be used to identify the faulty process components. The improvements offered by the new method are highlighted as a summary of a comparison of the results in Table 14.

The proposed method was also tested on the simulator of the board machine of Stora Enso. Four selected fault scenarios were tested in the three-layered board machine: a sensor fault, and three process component faults. The results for the first fault scenario, i.e. a sensor fault, showed that the conventional dynamic causal digraph method and the proposed method give the same results. In the second and third scenarios, however, the traditional method could not form the correct detection set. The correct nodes were detected for the second and the third fault scenarios with the help of the fault effects separation approach. Moreover, in the fault diagnosis, the results for the last three scenarios, which were process type faults, were further improved by locating the process fault on the arcs using the proposed inference mechanism between the arcs. The possible fault process component can be identified by carrying out further analyses. The improvements offered by the enhanced method are highlighted as a summary of a comparison of the results in Table 15.

Table 14. Comparison of the results between the proposed method and the conventional method in test 1.

Faults	Fault Type	Dynamic causal digraph		Enhanced dynamic causal digraph	
		Fault detection	Fault isolation	Fault detection	Fault isolation
Fault 1	Actuator fault (treated as process fault)	**Nodes**: *defic*, *hbfic*, *wpfic*, *bw*, *ash*	**Fault origin**: *defic*	**Nodes**: *defic*, *hbfic*, *wpfic*, *bw*, *ash*	**Faulty arcs sets**: {<*baval*, *defic*>}, {<*baval*, *defic*>, <*wpfic*, *defic*>} and {<*wpfic*, *defic*>} **Possible faulty components**: basis weight valve hydrocyclone
Fault 2	Sensor fault	**Nodes**: *defic*	**Fault origin**: *defic*	**Nodes**: *defic*	Fault origin: *defic*
Fault 3	Process fault	**Nodes**: *defc*, *hbfc*, *wpfc*, *ash*	**Fault origins**: *wpfic*, *ash*	**Nodes**: *defc*, *hbfc*, *wpfc*, *ash*, *bw*	**Faulty arcs sets**: {<*hbfc*, *wpfc*>, <*hbfc*, *ash*>, <*hbfc*, *bw*>} and <*hbfc*, *wpfc*>, <*hbfc*, *ash*>, <*hbfc*, *bw*>, <*totalflow*, *bw*>} **Possible faulty component**: Former section

Table 15. Comparison of the results between the proposed method and the conventional method in test 2.

Faults	Fault Type	Dynamic causal digraph		Enhanced dynamic causal digraph	
		Fault detection	Fault isolation	Fault detection	Fault isolation
Fault 1	Sensor fault	**Nodes**: *pcon2*	**Fault origin**: *pcon2*	**Nodes**: *pcon2*	Fault origin: *pcon2*
Fault 2	Process fault	**Nodes**: *acceptcon2*, *headcon2*, *wpcon2*	**Fault origin**: *wpcon2*	**Nodes**: *acceptcon2*, *headcon2*, *wpcon2*, *drybw2*	**Faulty arc sets (4)**: {<*headcon2*, *wpcon2*>, <*headcon2*, *drybw2*>}, etc. **Possible faulty component**: Former section
Fault 3	Process fault	**Nodes**: *headflow2*, *headcon2*	**Fault origins**: *headflow2*	**Nodes**: *headflow2*, *headcon2*, *drybw2*	**Faulty arc sets (3)**: {<*headspeed2*, *headflow22*>, <*sliceopen2*, *headflow22*>} **Possible faulty component**: Pipe component between the headbox feed pump and the headbox
Fault 4	Process fault	**Nodes**: *headflow2*, *acceptcon2*, *headcon2*, *drybw2*	**Fault origins**: *headflow2*, *acceptcon2*	**Nodes**: *headflow2*, *acceptcon2*, *headcon2*, *drybw2*	**Faulty arc sets (2)**: {<*headspeed2*, *headflow22*>, <*sliceopen2*, *headflow22*>, <*headflow22*, *acceptcon2*>} **Possible faulty component**: Hydrocyclone or the pipe network between hydrocyclone and the headbox feed pump

7 Conclusions

In this work, an enhanced dynamic causal digraph method for fault diagnosis has been proposed for improving the conventional method in terms of fault detection and diagnosis. On the basis of the conventional method, the enhanced method introduces a fault effects separation approach and an inference mechanism between the arcs. In the fault effects separation approach, the contributions of the fault effects from the parent nodes and the contribution of the local fault effects are calculated and separated according to their directions. As a result, the cancellation of fault effects is taken into consideration in the fault detection and isolation, thus giving better detection results and a more complete fault propagation path. Furthermore, the inference mechanism between the arcs allows the process fault to be located on the arcs, which helps in identifying the possible faulty process components. The process knowledge concerning the relationship between different cause effect models are first introduced into the digraph model in the form of an inter-arc knowledge matrix. The sets of suspected arcs formed from the diagnosis results of the conventional method are then tested with the inter-arc knowledge matrix. This results in the removal of spurious results, thereby allowing further identification of the possible faulty process components.

The procedure used in applying the proposed method was presented next. The procedure includes four steps: a process study, causal digraph modelling, a fault study and the fault diagnosis. In the process study, the necessary process knowledge is obtained either from the simulator or from the process flowsheet. The knowledge and fault-free data are used in the second step to construct the dynamic causal digraph model and the inter-arc knowledge matrix. In the third step, the selected fault scenarios are studied and simulated in the simulator. In the last step fault diagnosis is performed on the collected faulty data using the enhanced causal digraph method.

The hypotheses presented in Chapter 1 are: (1) The developed fault effects separation approach is able to enhance the traditional dynamic causal digraph method by giving better fault detection results for a process fault compared with the traditional method, (2) The dynamic causal digraph method enhanced by the developed inference mechanism is able to provide better diagnosis results for the process fault compared with the traditional method. The hypotheses have been verified using the results of two experimental tests of the proposed method.

During the tests, the following aspects concerning the application and the method itself are noticed:

1. Causal digraph methods are group of methods that try to not only detect fault but also diagnose fault with models constructed from the fault free data. In this sense, causal digraph methods show advantages over either quantitative model based method or history data based method. Compared with the quantitative model based method, causal digraph methods require less modelling effort, since data-based model can be used for modelling. On the other hand, the process structure information in the digraph model can be used for fault isolation, which is lacked from the history data based methods. The classification type of history data based methods is able to provide good diagnosis results at cost of faulty data for model training. However, even though the regression kind of history data based methods does not require faulty data, they cannot provide reliable diagnosis results.
2. The amount of measurements available significantly affects the structure of the causal digraph model and the fault diagnosis results resolution. The major challenge of the causal digraph modelling is to form the structure that connected available variables properly. It requires the combination of the analysis of the experiment data and the process knowledge. A model represents process well can only be obtained after several refining iterations by checking the modelling error with the given model structure. Usually, the simplest structure that can produce small enough modelling error is the best choice.

3. Simulating a fault in the simulator is not a trivial thing as it is considered. Since the data for a specific fault is usually not available, it is quite nature to obtain it by simulation way. However, the simulators are usually built for the normal situation. Therefore, how to obtain the faulty data that is representative for the fault scenario requires some process knowledge or communication with plant operator.

In the future, the enhanced method will be off-line tested first on the board machine of Stora Enso before the on-line implementation. The research topics related to the causal digraph method include: the introduction of more quantitative knowledge into the inter-arc knowledge matrix, the introduction of the parameter online estimation methods to locate the fault on the arcs and to provide more information about the process faults.

8 Appendices

Appendix A: Parameters of the cause-effect models in the board machine causal digraph

Table 16. Cause-effect models for the stock preparation of the layer 1&3 in the board machine.

Nodes	Input weights	Layer weights	Bias
birflow13	$[0.248 \quad -0.339 \quad 1.2478 \quad -1.01 \quad -74.4]$[1)]	115	$[4.26 \quad -26.2]$
birdflow13	$\begin{bmatrix} 16.2 & -50.3 & 50.2 & 0.0459 \\ -590 & 2.19*10^4 & -2.06*10^4 & -1.31 \end{bmatrix}$	$[4.97 \quad 0.568]$	$[-3.74 \quad 89.0 \quad 9.37]$
pflow13	$[-0.369 \quad 1.00 \quad -2.93 \quad 2.39 \quad 110]$	-47.3	$[-5.85 \quad -1.47]$
pdflow13	$\begin{bmatrix} -1.52*10^3 & 3.91*10^3 & -3.05*10^3 & -2.68 \\ -220 & 549 & -475 & 0.0570 \end{bmatrix}$	$[-0.111 \quad -1.65]$	$[242 \quad 29.2 \quad 5.04]$
dflow13	$\begin{bmatrix} -975 \\ 3.36 \end{bmatrix}$	$[-0.240 \quad 431]$	$[72.9 \quad 0.934 \quad -317]$
belflow13	$[-0.601 \quad 0.167]$	710	$[-0.688 \quad 285]$

[1)] In Table 16-Table 20, only 3 digits are reported.

Table 17. Cause effect models for the stock preparation of the layer 2 in the board machine.

Nodes	Input weights	Layer weights	Bias
pflow2	$[-1.18 \quad -18.1 \quad 180 \quad -606 \quad 349]$	-5.74	$[-15.1 \quad 16.1]$
pdflow2	$\begin{bmatrix} 20.0 & -233 & 1.25*10^{3} & -8.51*10^{-3} \\ -999 & -56.7 & 897 & 6.22 \end{bmatrix}$	$[38.9 \quad 0.0312]$	$[1.58 \quad 6.94 \quad -36.9]$
cflow2	$[0.0525 \quad -0.486 \quad 12.0 \quad -86.4 \quad -19.3]$	76.7	$[1.75 \quad -3.10]$
cdflow2	$\begin{bmatrix} -67.1 & -53.1 & 6.66*10^{3} & -9.11*10^{-3} \\ -146 & 312 & -5.40*10^{3} & 0.0286 \end{bmatrix}$	$[-10.3 \quad -0.325]$	$[4.62 \quad 9.27 \quad 11.2]$
broflow2	$\begin{bmatrix} 105 \\ 3.03 \end{bmatrix}$		
brodflow2	-24.0	-0.985	$[1.46 \quad 1.31]$
dflow2	$\begin{bmatrix} -2.31 \\ 6.24 \end{bmatrix}$	$[-20.6 \quad 18.9]$	$[-0.459 \quad 0.0945 \quad 0.0945]$
bleflow2	3.55	-91.3	$[0.868 \quad 258]$

Table 18. Cause-effect models for the short circulation of the layer 1 in the board machine.

Nodes	Coefficients for linear regression	Other parameter
headflow12	$[3.21 \quad 10.4 \quad -88.7]^{T}$	
scflow1	$[81.5 \quad -0.843 \quad -1885.7479]^{T}$	
acceptcon1	$[0.124 \quad 1.92*10^{-3} \quad -1.74*10^{-3} \quad -1.90*10^{-6} \quad 1.65*10^{-5} \quad 7.21*10^{-4}]^{T}$	
headcon1	$[-0.0205 \quad 537 \quad 1.27*10^{-4}]^{T}$	
wpcon1	0.0814 (gain of the first order model)	0.922 (pole)
drybw1	0.954 (retention rate of the solid content)	

Table 19. Cause-effect models for the short circulation of the layer 2 in the board machine.

Nodes	Coefficients for linear regression	Other parameter
headflow22	$[3.80 \quad 12.3 \quad 194]^T$	
scflow2	$[15.3 \quad -0.0754 \quad 1.08 \quad -641]^T$	
acceptcon2	$[0.812 \quad 1.54*10^{-3} \quad -1.29*10^{-2} \quad -5.62*10^{-6} \quad -3.74*10^{-5} \quad 2.41*10^{-3}]^T$	
headcon2	$[11.1 \quad 1.12*10^{5} \quad 749 \quad -699]^T$	
wpcon2	0.102 (gain of the first order model)	0.582 (pole)
drybw2	0.933 (retention rate of the solid content)	

Table 20. Cause-effect models for the short circulation of the layer 3 in the board machine.

Nodes	Coefficients for linear regression	Other
headflow32	$[3.00 \quad 9.19 \quad -76.2]^T$	
scflow3	$[150 \quad -1.33 \quad -4131.3774]^T$	
acceptcon3	$10^{-2} * [6.57*10^{-2} \quad 1.86*10^{-3} \quad -3.46*10^{-3} \quad -2.19*10^{-6} \quad -2.61*10^{-5} \quad 9.62*10^{-4}]^T$	
headcon3	$[-0.0269 \quad 528 \quad 7.94*10^{-5}]^T$	
wpcon3	0.0552 (gain of the first order model)	0.910 (pole)
drybw3	0.933 (retention rate of the solid content)	

References

Ahn, S.J., Lee, C.J., Jung, Y., Han, C., Yoon, E.S. & Lee, G., 2008. Fault diagnosis of the multi-stage flash desalination process based on signed digraph and dynamic partial least square, *Desalination*, 228(1-3), pp.68-83.

Cheng, H., Nikus, M. & Jämsä-Jounela, S-L., 2006. Application of a causal digraph based fault diagnosis method with state space models on a paper making process simulator. In: NECST (Networked Control Tolerant to Faults), *2nd workshop on networked control system and fault tolerant control*, Rendo, Italy 23-24 November. 2006.

Cheng, H., Nikus, M. & Jämsä-Jounela, S-L., 2008a. Fault diagnosis of the paper machine short circulation process using novel dynamic causal digraph reasoning, *Journal of Process Control* 18 (7-8), pp.676-691.

Cheng, H., Nikus, M. & Jämsä-Jounela, S-L., 2008b. Evaluation of PCA methods with improved fault isolation capabilities on a paper machine simulator, *Chemometrics and Intelligent Laboratory Systems*, 92 (2) pp.186-199.

Chung, H., Bien, Z., Park, J. & Seong, P., 1994. Incipient multiple fault diagnosis in real time with application to large-scale systems, *IEEE transcation on nuclear science*, 41(4), pp.1692-1703.

Fagarasan, I., Ploix, S. & Gentil, S., 2004. Causal fault detection and isolation based on a set-membership approach, A*utomatica*, 40 (12), pp.2099-2110.

Han, C., Shih, R. & Lee, L., 1994. Quantifying Signed Directed Graphs with the Fuzzy Set for Fault Diagnosis Resolution Improvement, *Industrial & Engineering Chemistry Research*, 33 (8), pp.1943-1954.

Hinckley, D.V., 1971. Inference about the change-point from cumulative sum tests, *Biometrika*, 58, pp.509-523.

Huang, Y.C. & Wang, X.Z., 1999. Application of fuzzy causal networks to waste water treatment plants, *Chemical Engineering Science*, 54(13-14), pp.2731-2738.

Iri, M., Aoki, K., O'Shima E. & Matsuyama, H., 1979. An algorithm for diagnosis of system failures in the chemical process, *Computer & Chemical Engineering*, 3 (1-4), pp. 489-493.

Isermann, R. & Balle, P., 1997. Trends in the application of Model-based fault detection and diagnosis of technical processes, *Control Engineering Practice*, 5 (5), pp.709-719.

Isermann, R., 2006. *Fault-diagnosis systems*. Heidelberg: Springer.

Juslin, K., 2005. A Companion Model Approach to Modelling and Simulation of Industrial Processes. Number 574 in VTT Publications. Espoo: VTT.

Jämsä-Jounela, S-L., Vermasvuori, M., Enden, P., Haavisto, S., 2003. A process monitoring system based on the Kohonen self-organizing maps. *Control Engineering Practice*, 11(1), pp. 83-92.

Kämpjärvi, P., Sourander, M., Komulainen, T., Vatanski, N., Nikus, M. & Jämsä-Jounela, S-L., 2008. Fault detection and isolation of an on-line analyzer for an ethylene cracking process, *Control Engineering Practice*, 16(1), pp. 1-13.

Karray, F.O. & Silva C., 2004. *Soft Computing and Intelligent System Design*, Essex: Pearson Education Limited.

Komulainen, T., Sourander, M. & Jämsä-Jounela, S-L., 2004. An online application of dynamic PLS to a dearomatization process, *Computer & Chemical Engineering*, 28(12), pp.2611-2619.

Lai, J. & Yu, C., 1995. Qualitative-model Simplification with an Application to Multistage Separation Processes, *Engineering Applications of Artificial Intelligence*, 8 (5)5, pp.549-559.

Laukkanen, I., 2001. *Studies in using hybrid dynamic simulation through the lifecycle of paper mill*, Licentiate, Helsinki: Helsinki University of Technology.

Lapizco-Encinas, G. & Reqqia, J., 2005. Diagnostic Problem Solving Using Swarm Intelligence. In: IEEE, *Swarm Intelligence Symposium*, Pasadena, USA 8-10 June 2005

Lappalainen, J., Myller, T., Vehviläinen, O., Tuuri, S. & Juslin, K., 2003. Enhancing grade changes using dynamic simulation, *TAPPI Journal*, 2 (12)

Lappalainen, J., 2004. Paperin- ja kartonginvalmistus-prosessien mallinnus ja dynaaminen reaaliaikainen simulointi. Number 574 in VTT Publications. Espoo: VTT.

Larsson J.E., 1996. Diagnosis based on explicit means-end models, *Artificial Intelligence*, 80(1), pp.29-93.

Lee, G., Tosukhowong, T., Lee, J.H. & Han, C., 2006. Fault diagnosis using the hybrid method of signed digraph and partial least squares with time delay: the pulp mill process, *Industrial & Engineering Chemistry Research*, 45(26), pp.9061-9074.

Leyval, L., Gentil, S. & Feray-beaumont, S., 1994. Model-based Causal Reasoning for Process Supervision, *Automatica*, 30 (8), pp.1295-1306.

Lo, C.H., Wong, Y.K. & Bad, A.B., 2004. Model-based fault diagnosis in continuous dynamic systems. *ISA Transactions*, 43(3), pp.459-475.

Lumiainen, J., 2000. Refining of chemical pulp. In: Paulapuro, H., ed. 2000. *Papermaking Part 1, Stock Preparation and wet end*, Jyväskylä: FAPET Oy. Ch.4.

Maurya, M.R., Rengaswamy, R. & Venkatasubramanian, V., 2003a. A systematic framework for the development and analysis of signed digraphs for chemical process. 1.

algorithm and analysis, *Industrial & Engineering Chemistry Research*, 42(20), pp.4789-4810.

Maurya, M.R., Rengaswamy, R. & Venkatasubramanian, V., 2003b. A systematic framework for the development and analysis of signed digraphs for chemical process. 1. control loops and flowsheet analysis, *Industrial & Engineering Chemistry Research*, 42(20), pp.4811-4827.

Maurya, M.R., Rengaswamy, R. & Venkatasubramanian, V., 2004. Application of signed digraphs-based analysis for fault diagnosis of chemical process flowsheets, *Engineering Application of Artificial Intelligence*, 17(5), pp.501-518.

Maurya, M.R., Rengaswamy, R. & Venkatasubramanian, V., 2006. A signed directed graph-based systematic framework for steady-state malfunction diagnosis inside control loops, *Chemical Engineering Science*, 61(6), pp.1790-1810.

Metso Automation, 2007. 50-year-old machine still at the top of its class, *Automation*, 14(2), pp.4-7.

Montmain, J. & Gentil, S., 2000. Dynamic causal model diagnostic reasoning for online technical process supervision, *Automatica*, 36 (8), pp.1137-1152.

Mourot, G., Bousghiri, S. & Ragot, J., 1993. Pattern recognition for diagnosis of technological systems: a review. In: System, Man and Cybernetics, *IEEE International conference on System Engineering in the Service of Humans*, Le Touquet, France 17-20 October 1993.

Oyeleye, O. & Kramer, A., 1988. Qualitative simulation of chemical process systems: steady-state analysis, *American Institute of Chemical Engineers (AICHE) Journal*, 34(9), pp. 1441-1454.

Paulapuro. H., 2000. Wet pressing. In: Paulapuro, H., ed. 2000. *Papermaking Part1, Stock Preparation and Wet End*, Jyväskylä: FAPET Oy, Ch.8.

Riera, B., Lambert, M. & Amat, A., 1999. Specification for an Advanced Human Centered Supervisory System. In: Systems, Man and Cybernetics, *IEEE International conference on Systems, Man, and Cybernetics Conference*, Tokyo, Japan 12-15 October 1999.

Saxén, B. & Saxén, H., 1994. NNDT - A neural network development tool - User's guide. Number 94-8 in Heat Engineering Lab technical report. Åbo: Åbo Akademi University.

Shih, R. & Lee, L., 1995a. Use of Fuzzy Cause-Effect Digraph for Resolution Fault Diagnosis for Process Plants. 1. Fuzzy Cause-Effect Digraph, *Industrial & Engineering Chemistry Research*, 34 (5), pp.1688-1702.

Shih, R. & Lee, L., 1995b. Use of Fuzzy Cause-Effect Digraph for Resolution Fault Diagnosis for Process Plants. 2. Diagnostic Algorithm and Applications, *Industrial & Engineering Chemistry Research*, 34 (5), pp.1703-1711.

Shiozaki, J., Shibata, B., Matsuyama, H. & O'shima, E., 1989. Fault Diagnosis of Chemical Processes Utilizing Signed Directed Graphs-Improvement by Using Temporal Information, *IEEE Transactions on Industrial Electronics*, 36 (4), pp.469-474.

Silvennoinen, E., Juslin, K., Hänninen, M., Tiihonen, O., Kurki, J., & Porkholm, K., 1989. The APROS software for process simulation and model development. Number 618 in Valtion teknillisen tutkimuskeskuksen tutkimuksia.

Stora Enso Oyj, 2003. A three-layered board machine simulator in APROS environment, Imatra.

Tarifa, E.E. & Scenna, N.J., 1997. Fault diagnosis, direct graphs, and fuzzy logic, *Computer & Chemical Engineering*, 21(Supplement1), pp.S649-S654.

Tarifa, E.E. & Scenna, N.J., 2004. Fault diagnosis for MSF dynamic states using a SDG and fuzzy logic, *Desalination*, 166, pp.93-101.

Tuuri, S., Niemenmaa, A., Laukkanen, I., Lappalainen, J. & Juslin, K., 1995. A multi-purpose tool for dynamic simulation of paper and board mills. In: EUROSIM (Federation of European Simulation Societies), *2nd EUROSIM Congress*. Vienna, Austria 11-15 September 1995.

Vedam H. & Venkatasubramanian V., 1999. PCA-SDG based process monitoring and fault diagnosis, *Control Engineering Practice*, 7 (7), pp.903-917.

Venkatasubramanian, V., Rengaswamy, R., Yin, K. & Kavuri, S., 2003a. A review of process fault detection and diagnosis Part I: Quantitative model-based methods, *Computer & Chemical Engineering*, 27 (3), pp.293-311.

Venkatasubramanian, V., Rengaswamy, R., Yin, K. & Kavuri, S., 2003b. A review of process fault detection and diagnosis Part II: Qualitative models and search strategies, *Computer & Chemical Engineering*, 27 (3), pp.313-326.

Venkatasubramanian, V., Rengaswamy, R., Yin, K. & Kavuri, S., 2003c. A review of process fault detection and diagnosis Part III: Process history based methods, *Computer & Chemical Engineering*, 27 (3), pp.327-346.

VTT (Technical Research Centre of Finland), 2005. APROS 5.0.4 help document, Espoo: VTT.

Wang, X., Yang, S., Veloso, E., Lu, M. & Mcgreavy, C., 1995. Qualitative Process Modelling- A Fuzzy Signed Directed Graph Method, *Computers & chemical Engineering*, 19 (S1), pp.735-740.

Weise, U., Terho, J. & Paulapuro, H., 2000. Stock and water system of the paper machine. In: Paulapuro, H., ed. 2000. *Papermaking Part 1, Stock Preparation and wet end*, Jyväskylä: FAPET Oy. Ch.5.

Yu, C.C & Lee, C., 1991. Fault diagnosis based on qualitative/quantitative process knowledge, *American Institute of Chemical Engineers (AICHE) Journal*, 37(4), pp.617-628

Zhang, Z., Wu, C., Zhang, B. & Li, A., 2005. SDG multiple fault diagnosis by real-time inverse inference, *Reliability Engineering & System Safety*, 87 (2), pp.173-189.

ISBN 978-951-22-9878-5
ISBN 978-951-22-9879-2 (PDF)
ISSN 1795-2239
ISSN 1795-4584 (PDF)